Sensor Fusion of Charge Monitoring and Strain Gages for Piezoelectric Actuators

DIPLOMARBEIT

Ausgeführt zum Zwecke der Erlangung des akademischen Grades eines
Diplom-Ingenieurs (Dipl.-Ing.)

unter der Leitung von
Univ.Ass. Dipl.-Ing. Dominik Kohl, BSc
Univ.Ass. Dr. Rudolf Saathof, MSc
Univ.Prof. Dipl.-Ing. Dr.sc.techn. Georg Schitter, Dipl.NDS ETHZ

eingereicht an der
Technischen Universität Wien
Fakultät für Elektrotechnik und Informationstechnik
Institut für Automatisierungs- und Regelungstechnik

von
Severin Hoser, BSc
Matrikelnummer: 0826551
Gutauer Str. 24
4283 Bad Zell, Österreich

Wien, im März 2016

Gruppe für Industrielle Automationstechnik
Gusshausstrasse 27-29, A-1040 Wien, Internet: http://www.acin.tuwien.ac.at

Acknowledgment

I am using this opportunity to express my gratitude to Prof. Schitter for enabling me to compile my master project at the Automation and Control Institute of TU Vienna.

I express my thanks to Rudolf Saathof and Dominik Kohl for their support and guidance through this thesis. Both always found time to help and supported me in acquiring the proficiencies needed to finish my master thesis.

To my friends, thank you for listening, offering advice and support during the process of compiling this master thesis.

Finally, I express my very profound thanks to my family for giving me continuous encouragement and unfailing support.

Abstract

Piezoelectric actuators have established as standard actuators in nanopositioning applications due to their sub-nanometer positioning resolution and high resonance frequency. However, the main disadvantage of piezoelectric actuators are the inherent nonlinearity between applied voltage and elongation. Effects, like hysteresis, saturation and creep reduce the actuator positioning accuracy. It is well known for several decades, that these nonlinear effects are reduced in the relation between elongation and charge.

Two different approaches are applied to acquire the charge of a piezoelectric actuator while actuation, integration of the current through a shunt resistor and insertion of a sensing capacitor in this master thesis. Both approaches of measuring charge are analyzed and compared with respect to noise and accuracy.

Charge monitoring is prone to show less noise at increased frequencies while suffering from low frequency noise. In order to take benefit of the low broadband noise of charge monitoring and the DC stability of strain gages, both sensors are combined by sensor fusion. By the means of this method the standard deviation of charge monitoring is reduced from 2.2 nm to 0.56 nm at the combined sensor in the frequency range from 1 mHz to 2 kHz. Although in literature often ignored, charge monitoring suffers from residual nonlinearities. Typical spectra encountered in scanning systems are used to assess the systematic error with a novel method. This method takes both random and systematic error into account. The aim of this approach is to minimize the overall uncertainty, consisting of random and systematic error. The benefit of using charge instead of voltage to acquire the height signal is demonstrated at the vertical piezoelectric actuator of an Atomic Force Microscope. By the means of this method the difference between trace and retrace is reduced from 2.5 nm to 1.3 nm.

Zusammenfassung

Piezoelektrische Aktoren haben sich aufgrund ihrer subnanometer Auflösung und hohen Resonanzfrequenz als Standardaktuatoren für Nano-Positionieraufgaben etabliert. Der größte Nachteil von piezoelektrischen Aktuatoren ist der nichtlineare Zusammenhang zwischen angelegter Spannung und Längenänderung. Bestimmte Effekte wie Hysterese, Sättigung und Creep reduzieren die Genauigkeit in Positionieraufgaben. Seit mehreren Jahrzehnten ist bereits bekannt, dass die nichtlinearen Effekte im Vergleich Ausdehnung und elektrischer Ladung geringer ausfallen, als im Vergleich Ausdehnung und Spannung.

In dieser Diplomarbeit werden zwei unterschiedliche Ansätze verwendet um die Ladung in piezoelektrischen Aktuatoren zu messen. Diese sind zum einen die Integration über den Strom durch einen Messwiderstand und zum anderen die Einführung eines Messkondensators. Beide Ansätze werden im Hinblick auf Rauschen und Genauigkeit der Messung analysiert und verglichen.

Ladungsmessung zeigt geringes Breitbandrauschen, während hingegen im niederfrequenten Bereich die Rauschdichte zunimmt. Um sowohl den Vorteil des niedrigen Breitbandrauschens der Ladungsmessung als auch die Stabilität von Dehnungsmessstreifen bei niedrigen Frequenzen zu nutzen, werden beide Sensoren mittels Sensordatenfusion kombiniert. Anhand dieses Ansatzes konnte die ursprüngliche Standardabweichung der Ladungsmessung von 2.2 nm auf 0.56 nm im Frequenzbereich von 1 mHz bis 2 kHz reduziert werden. Die Ladungsmessung zeigt eine verbleibende Nichtlinearität zur Längenänderung - ein Aspekt, der in der Literatur oft wenig Beachtung findet. Anhand einer neuen Methode werden systematische Fehler im Bezug auf typische Spektren für Messsysteme im Vorhinein abgeschätzt. Auf diese Weise gelingt es, sowohl zufällige als auch systematische Fehler in Betracht zu ziehen. Das Ziel dieses Ansatzes ist es, die Gesamtunsicherheit, bestehend aus systematischen und zufälligen Fehlern, zu minimieren. Anhand des vertikalen piezoelektrischen Aktuators eines Rasterkraftmikroskop wird der Vorteil der Verwendung von Ladung gegenüber Spannung zur Aufnahme des Höhenprofils verdeutlicht. Mit dieser Methode wird eine Reduktion der Unterschiede zwischen den Höhenprofilen, gemessen während dem Vor- und Rücklauf, von 2.5 nm auf 1.3 nm erreicht.

Contents

List of Figures

List of Tables

Acronyms

4QPD	4-Quadrant Photo Diode
AFM	Atomic Force Microscope
FFT	fast-fourier-transform
in-amp	instrumentation amplifier
LVDT	Linear Variable Displacement Transformers
NSD	Noise Spectral Density
op-amp	operational amplifier
piezo	piezoelectric actuator
PSD	Power Spectral Density
RMS	root mean square
SNR	Signal-to-Noise Ratio

CHAPTER 1

Introduction

1.1 Atomic Force Microscopy

Atomic Force Microscope (AFM) is a powerful tool for imaging and nanofabrication that enables observation and manipulation of samples at the atomic level [1]. AFM differs from other microscopes, as the image is not captured by focusing light or electrons on the surface, like optical or electron microscopes. In AFM the topography is gathered with a mechanical probe [2]. AFM is an astonishing method to acquire surface structures with unprecedented resolution, accuracy and a high flexibility in the samples that can be investigated [3]. Very hard samples such as the surface of a ceramic material [4] as well as very soft samples like human cells [5] or individual molecules of a DNA [6] can be measured. AFM is also in respect to sample size very versatile: very small images (5 nm) showing the crystallographic structure of materials can be acquired as well as large images (100 μm) which show the shape of living cells [7–11].

The schematic of a standard feedback controlled AFM is depicted in Figure 1.1. The sample to image is brought into close proximity to a sharp tip mounted on the end of a cantilever [13]. Depending on the tip-sample separation attractive and repulsive forces are encountered between tip and sample [14]. This interaction force consists of a variety of short and long range forces such as electrostatic, van der Waals, capillary, specific chemical, Pauli repulsion, nanoscale contact and elastic forces [15]. The interacting force between tip and sample results in a deflection of the cantilever. A laser spot is aligned on the back of the reflecting cantilever. Depending on the cantilever deflection the position of the laser spot on the 4QPD changes. The deflection signal from the optical detector and thereby also the interaction force is kept constant by controlling the elongation of the Z-piezoelectric actuator (piezo). Thereby, the elongation of the Z-piezo represents the sample topography. The output signal of the controller is typically used as estimate of the surface topography. In order to acquire the topography of the required sample the tip has to be scanned over the sample. This movement

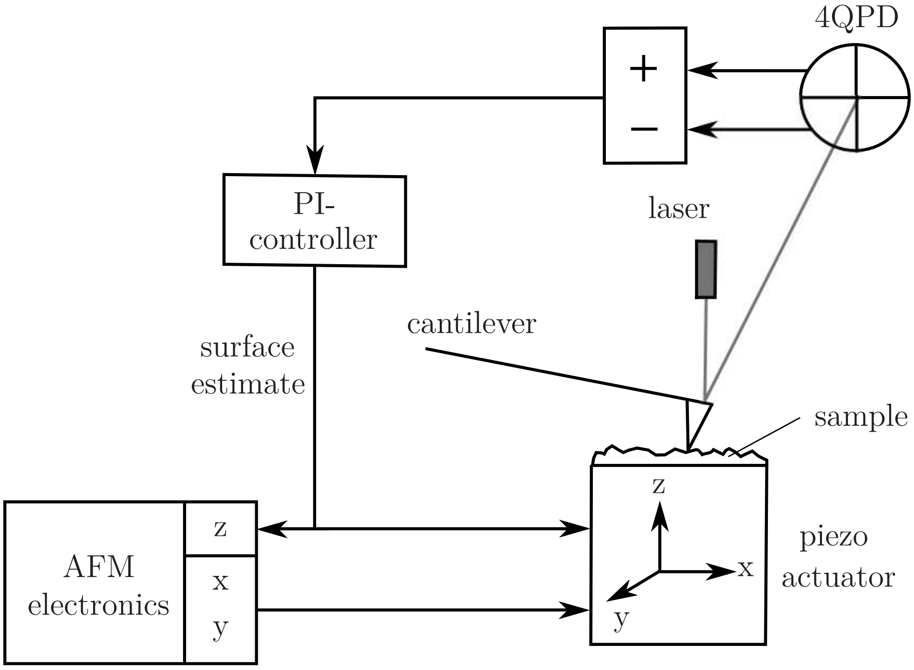

Figure 1.1: The schematic shows the working principle of an AFM. A sharp tip mounted on a cantilever is brought into close proximity to the sample. The interaction force between tip and sample results in a deflection of the cantilever. The deflection is measured by a laser spot reflected from the cantilever towards a 4QPD. The deflection and thereby the interaction force is kept constant by controlling the elongation of the Z-piezo by a PI feedback controller. The controller output represents the surface of the sample. In order to acquire the topography of the whole sample, relative motion between tip and sample in the horizontal X-Y plane is performed by the piezo. The figure is redrawn from [12].

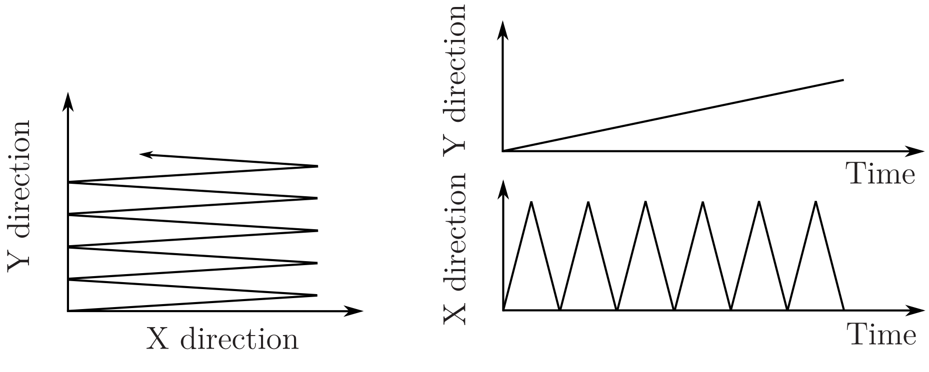

Figure 1.2: The relative motion between tip and sample in the horizontal X-Y plane is depicted in the left figure. To acquire one line a forward and backward motion is needed in the X direction. A slow movement in the Y-direction ensures the acquisition of the adjacent line in the following cycle. A triangular movement is required to generate this pattern along the fast scan axis (X direction in the right figure). While the slow scan axis (Y direction) follows a ramp. This figure is based on [3].

is typically done in a raster scan motion depicted in Figure 1.2.

In AFM the tip is scanned over the surface line by line (left). A triangular signal is needed in the fast scan axis (X). Simultaneously the slow scan axis (Y) tracks a slowly increasing ramp. The actuation can be fulfilled by individual actuators for each axis [16], by a three degree of freedom tube piezo [17] or even by taking advantage of dual-actuation using both of them [18]. The excellent properties, which establish piezos as standard actuators for AFM, in order to reach high resolution and fast motions are discussed in the following chapter.

1.2 Piezoelectricity

The physicist Pierre and Paul-Jacques Curie discovered the generation of an electric potential in a quartz crystal under compression [19]. This interaction between mechanical and electrical domain is called direct piezoelectric effect. In addition to the direct piezoelectric effect, also its reverse relation exists, called inverse piezoelectric effect [20]. The inverse piezoelectric effect describes the expansion or contraction of a piezoelectric material due to an electric field applied to its electrodes. This enables piezos to work as an actuator and sensor simultaneously [21]. Beside quartz, piezoelectricity is also found in several other materials in particular piezo ceramics [22]. The origin of the piezoelectric effect is asymmetry in the materials molecular structure [23]. This comes along with an asymmetric charge distribution. Piezoelectric actuators offer subnanometer resolution. Another advantage of piezo is their high stiffness and compact size. Hence, they provide the possibility to build fast positioning systems due to their very high resonance frequency [16]. Piezos can expand by about 0.2 % of their total length [24]. A drawback of high stiffness is its high transmission of vibration from the surrounding. Although, piezos offer extremely high resolution, the overall accuracy is often limited by nonlinearities. A nonlinear effect encountered between voltage applied to the piezo and its elongation is hysteresis [25]. Due to the polarization of microscopic ferroelectric particles, the elongation of the piezo depends on the currently applied voltage as well as on the past values of applied voltage. Hysteresis manifests as difference in motion path for increasing and decreasing voltage as shown in Figure 1.3. Especially when piezos are used over long ranges, hysteresis introduces significant positioning error. Piezoelectric actuators show slow drift in elongation, after the applied voltage is changed, known as creep [26]. Creep shows a long settling time [19]. The elongation originating from creep can be as large as 10 % of the total displacement [27]. In particular when applying a piezo in open-loop the aforementioned nonlinearities are crucial. Due to creep and hysteresis the elongation of the piezo can not be obtained from the applied voltage without further information [28]. When the topography is reconstructed from the controller output voltage, the nonlinearities of the piezo results in systematic errors in the topography. The influence of the Z-piezo nonlinearity on the measured topography is shown in [29]. Commonly the AFM image is acquired only during forward or backward movement of the fast scanning piezo. When nonlinearities are not treated properly X-, Y- and Z-scanning motion are distorted. Thereby, the data acquired in the profile line shows systematic errors. Artefacts originating from

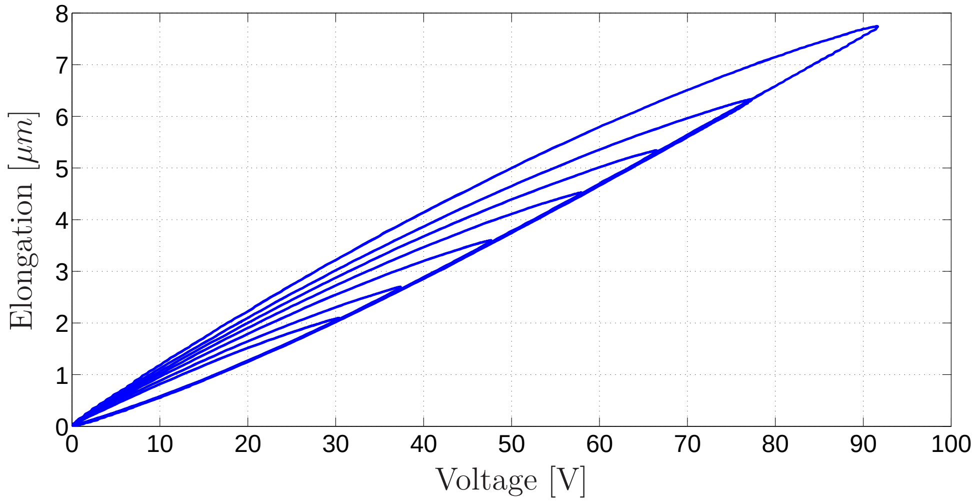

Figure 1.3: The measured hysteresis between applied voltage and elongation results in different motion path, depending on whether the applied voltage is increasing or decreasing. The elongation is measured with a capacitive sensor.

the nonlinearities of the X- and Y-piezo are shown in [3], [26] and [30].

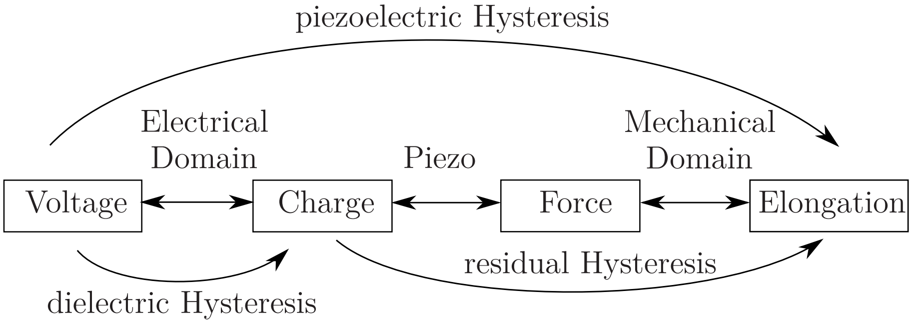

Figure 1.4: The schematic shows the origin of the dominant nonlinear behavior in piezos. As between charge and elongation a reduced hysteresis is encountered, the nonlinearity is mainly found in the capacitor which determines the relation between charge and voltage. This figure is based on [31].

It's known for several decades that nonlinearities are smaller between charge and elongation than between voltage and elongation [32], [33]. The schematic of the interaction between mechanical domain and electrical domain of a piezo is shown in Figure 1.4. The majority of the nonlinearity is encountered in the electrical domain between voltage and charge. Therefore, the charge of a piezo can be used to reduce the influence of the nonlinearities [34].

Inside the piezoelectric ceramic the voltage is represented by the electric field. As the relative permittivity of piezoelectric ceramics is $\varepsilon_{33} \gg 1$, the polarization of free space is negligible. Therefore, charge at the electrodes appears as polarization in the material. The hysteresis in the piezoelectric strain-electric field originates from processes that contributes to both - strain and polarization. An example for such processes are non-180°domain wall movements at weak fields [35]. In contrast, the movement of 180°walls contribute just to the polarization, but not to the piezoelectric strain. Therefore, the 180°walls movement results in a deviation between charge and elongation.

At weak fields 180°wall movements show less influence [35]. The response of strain and polarization to weak fields are governed mainly by movements of ferroelectric domain walls. The dielectric (polarization-field) and the piezoelectric (strain-field) hysteresis are determined mostly by the same process. Therefore, at weak fields the deviation between charge (polarization) and elongation (strain) is small, which results in small residual hysteresis of charge monitoring [36].

1.3 Problem formulation

Although piezos show significant nonlinearities they are often used without compensation. The complexity of nanopositioning systems rises with continuously increasing requirements. Thereby the incorporation of sensor systems during system implementation is complicated. Especially when sensors need to be retrofitted into existing systems, bulky nanometer resolution sensors are often not an option. Therefore, the goal of this thesis is to implement an easy-to-integrate sensor principle which offers significant reduction of the nonlinearities encountered between voltage and elongation. The introduced sensor principle needs to cover the full bandwidth of typical scanning applications. The reduced nonlinearities results in an improved measurement of the absolute dimension of a feature. The quality of a measurement is next to accuracy also determined by the resolution. The resolution is defined as the smallest detail which can be resolved by the measurement principle. The improved accuracy must not be achieved at the expense of excessive random error. Therefore accuracy as well as resolution of the implemented sensor principle needs to be investigated in respect to typical applications in scanning systems.

CHAPTER 2

State of the art

Recently, a lot of effort is made for operating piezos in a linear fashion [37]. Generally, the approaches can be classified in three main concepts: feedforward control by using an inverse hysteresis model [38], sensor-based closed loop control [39], [40] and charge control [41]. When discussing the different approaches, focus is given on nanometer resolution positioning sensors as they are key components in many precision imaging and fabrication applications. The given review of position sensor technologies and their performance motivates to discuss sensor fusion as a method to take benefit of the advantages of several sensor principles.

2.1 Inverse hysteresis model

A common method to quantify hysteresis in piezos is to model their nonlinearity. Often used hysteresis models are the Coleman-Hodgdon [42] and the Preisach model [43]. The Preisach model assembles the hysteresis by a collection of switches. Thereby, the applied voltage can be used to determine the elongation of the piezo in an AFM [25]. An inverse hysteresis model can be used to compensate hysteresis [28]. This method is often used for the X- and Y-motion in commercial AFM systems [26]. The compensation of hysteresis is schematically depicted in Figure 2.1. The inverse model of the piezo's nonlinearities is used to shape the voltage applied to the actuator in order to reach a linear movement of the piezo. The shape of the hysteresis depends on the scan speed, scan size and offset applied to the piezo. This results in a high number of needed coefficients and a time consuming identification approach [44]. Furthermore, modeling of hysteresis is sensitive to changes in the operation conditions such as temperature and aging effects [45].

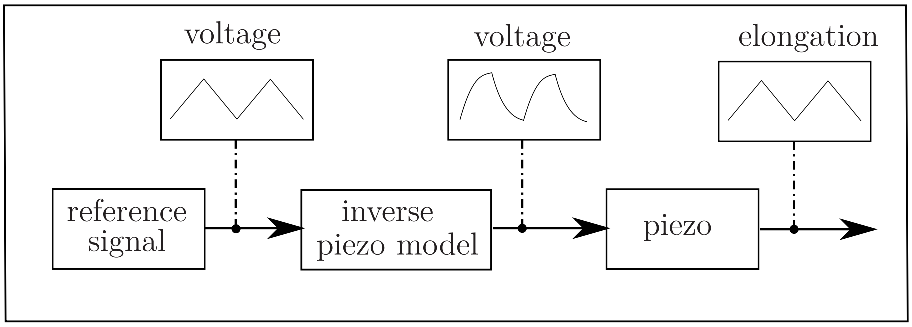

Figure 2.1: The schematic shows the working principle of an inverse piezo model. The inverse model of the piezo shapes the reference voltage. Due to the compensation of the hysteresis the actuator tracks the required triangular motion. The figure is based on [3]

2.1.1 Offline compensation

Another open-loop technique often found in AFM is to calibrate the piezos [3]. During calibration a very well-known sample with repetitive pattern is measured. From this measurement, information about the nonlinearities of the piezo is gained and stored in the calibration file. This information can be used to compensate for nonlinearities by software after acquiring the image and is associated with high computational effort. To ensure a high level of accuracy, the specimen measured during calibration should be similar in size with the feature, which is going to be measured. Calibration has similar disadvantages as the aforementioned hysteresis models, particularly sensitivity to changing operation conditions and creep.

2.2 Feedback control

Sensor-based feedback control is the most common approach for controlling piezos. The schematic of feedback control is depicted in Figure 2.2. A sensor measures the elongation of the piezo. This measurement is compared with the reference signal. The error between reference signal and measured elongation is compensated by the controller.

A drawback of feedback control is the sensor induced noise, which has direct influence on the resolution [46]. Another concern when doing feedback control is the limited closed-loop bandwidth caused by the presence of the piezo's high resonance peak. An improvement of the closed-loop bandwidth can be achieved by model based control [47–49]. Sensor-induced noise is a main disadvantage of closed-loop control. Moreover, nanometer resolution position sensors are key components in precision engineering applications. To fulfill the system requirements, a proper choice of the applied sensor principle is fundamental.

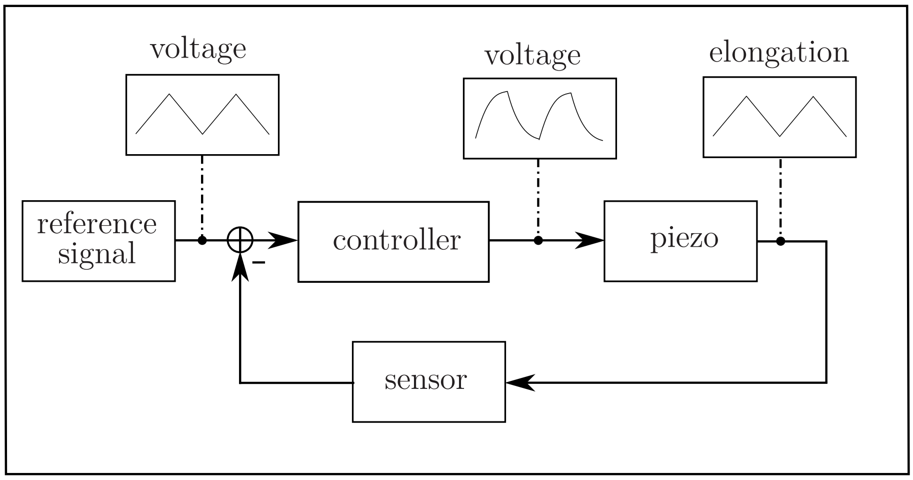

Figure 2.2: The schematic indicates the working principle of a feedback controled piezo. A sensor is used to acquire the elongation of the piezo. The deviation between the reference signal and the measured elongation is fed as error to the controller.

2.2.1 Nanometer resolution position sensors

An overview of commonly used sensor principles in nanopositioning with regard to range, noise, accuracy and the size of the sensor is given in the following based on [19] and [50].

Capacitive sensors

Capacitive sensors are based on a change in capacitance between two conducting surfaces. This change in capacitance is proportional to the displacement. They offer a high level of linearity, resolution and bandwidth. Therefore, they are the commonly used sensors in nanopositioning applications. The excellent linearity under ideal conditions is often degraded in practical applications, due to misalignment. Alignment of the sensor to the target is of high importance as tilting and bowing are crucial sources of nonlinearity. Tilt refers to the angle between the two capacitor plates and bowing describes the concavity or convexity of the target. Capacitive sensors require a relatively large, grounded targets [50]. The combination of the considerable size of capacitive sensors and the high demand in terms of sensor alignment result in difficulties in terms of integrating capacitive sensors into systems.

Eddy-current sensors

Eddy-current sensors rely on the principle of electromagnetic induction [51]. They consist of a coil excited by an AC current. When the coil is brought in proximity to an electrical conductive target, the magnetic field from the coil passes through the target. According to Lenz's law a current is induced in the target. The AC resistance of the coil is used to acquire the distance between probe and sample. They are often used in industrial applications, as they are tolerant against pollutants and dust on the sensor as well as in the air-gap between sensor and target [50]. The main drawback of Eddy-current sensors is their temperature sensitivity. The temperature sensitivity arises from the coil and the change of the target resistance with changing temperature. The minimum size of the coil imposes a minimum of the practical range (100 μm to 500 μm).

Linear variable displacement transformer

The major parts of a Linear Variable Displacement Transformers (LVDT) are one driving coil and two sensing coils. All three coils are wounded over a thermally stabled bobbin. The driving coil is arranged in the middle and the sensing coils are placed on each side of the driving coil. Any change in position of the core results in a linear differential change in the voltage, induced in the sensing coils. LVDT offer high resolution over a large range and are simple and robust. The electrical noise is very low due to low impedance of the sensing coils. The greatest disadvantage of LVDTs is their sensitivity to lateral movements and the limited bandwidth (100 Hz to 1 kHz). Especially in nanopositioning applications the added mass of the sensor might be a serious drawback as well. A LVDT is used to control the position of a nanopositioning device, actuated by a stacked piezo [39]. The electronics needed for the capacitive sensor, LVDT and eddy-current sensor consist mainly of an oscillator and demodulator.

Monochromatic confocal sensor

A monochromatic confocal sensor focuses light from a laser diode onto the target, which displacement is of interest. The reflected light passes the focusing lens. From a beam splitter the light is deflected onto a pinhole. If the focal point coincides with the surface of the target, the transmitted flux shows a maximum. With increasing distance of the surface from the focal point the transmitted flux decreases [52].

Laser triangulation

The working principle of laser triangulation is based on a laser aligned on the object to which the distance is of interest [53]. The optical path of the reflected laser beam is changed depending on the angle and distance to the measured surface. This change in light path is detected by a position sensitive detector. Triangulation sensors offer a long range (typically 0.5 mm to 1 m). Especially for large range measurements the resolution is correspondingly reduced.

Laser interferometer

A laser interferometer is based on interference of coherent laser beams that passes through optical paths with different length [19]. One beam is directed to the object of which the distance is to be measured. A second beam is reflected by a reference reflector. After returning to the interferometer both beams are recombined and interference occurs. The resulting interference pattern is a function of the phase difference between the interfering beams and hence its position. The homodyne interferometer uses light with only one frequency.

Heterodyne interferometer

In comparison, the heterodyne interferometer uses two different beams in the reference and measurement path. Although the heterodyne interferometer is more complex, it provides the benefit of measuring movements with only the AC part of the signal. Thereby, induced error by low frequency noise can be avoided [54]. The laser heterodyne interferometer has become accepted as standard, whenever high absolute accuracy is needed over long range. Compared to the other sensor technologies introduced in this chapter, the heterodyne interferometer provides the highest level of accuracy. Nevertheless, it is expensive and bulky and therefore often difficult to incorporate into nanopositioning systems.

Resistive strain gages

Resistive strain gages consist of a thin layer of conduction foil deposited on a carrier material. Any change in elongation results in an proportional change in resistance, mainly introduced by changes in geometry of the resistor. The difference in resistance is used to acquire the displacement of the target. They can be easily integrated into an existing system by bonding them on the surface of the actuator. They are often used for position control [55] as they are simple and of low cost [56]. Nevertheless, a serious handicap of strain gages is their high measurement noise, originating from thermal noise and low sensitivity.

Piezoresistive sensors

Piezoresistive sensors are made of semiconductors and show a change in conductivity, when strain is applied to them. They offer an up to two order-of-magnitude higher sensitivity in comparison to the aforementioned resistive strain gages. Their main disadvantages are low strain range (0.1 %), nonlinearity (1 %) and poor thermal stability [57].

Giant magnetoresistance sensors

Giant magnetoresistance sensors (GMR-sensors) are based on the change in resistance of a material in response to a magnetic field. For some multilayer systems the change in resistance can reach an extent of 80 % of the initial resistance [58]. The drawback of GMR-sensors is their hysteresis of up to 4 %. The electronics required to read out the change in resistance of the resistive strain gages, piezoresistive sensors and the GMR are similar and quite simple. A bridge configuration can be used to acquire the elongation [59].

Piezoelectric strain sensors

In addition to application as actuator, piezos are also used as piezoelectric strain sensors. Due to the direct piezoelectric effect, strain can be measured in terms of charge [60]. Resulting from the capacitive source impedance of piezos, piezoelectric strain sensors are susceptible to low frequency current noise of the instrumentation. Dielectric leakage and finite buffer impedance introduces a low frequency boundary of piezoelectric strain sensors. However, at high frequencies the noise spectral density of the piezoelectric force sensor is lower than the noise spectral density of the resistive strain gages. Piezoelectric strain sensors suffer from nonlinearities in the range of 0.4 % [61].

Table 2.1: The most relevant properties of the discussed sensors in comparison.

sensor principle	range	noise	size	cost	accuracy
res. strain gage	medium	high	small	low	good
piezores. sensor	low	low	small	medium	medium
GMR sensor	medium	low	small	low	poor
piezoelectr. strain sensor	low	low	small	medium	poor
capacitive sensor	far	low	medium	high	good
eddy current sensor	far	medium	medium	high	medium
LVDT	far	low	medium	high	medium
confocal sensor	far	low	big	high	good
interferometer	far	low	big	very high	very good
heterodyne interferometer	far	very low	big	very high	very good

Table 2.2.1 gives a comparison of the most relevant properties of the discussed sensors. Piezos offer fast and high resolution positioning when used as actuators. Moreover, when applied as piezoelectric strain sensors, strain can be measured in terms of charge with low broadband noise. In the following methods are discussed, which takes benefit of both applications simultaneously.

2.3 Charge monitoring

An alternative method to reduce the influence of creep and hysteresis is measuring the charge of the piezo. Below the resonance frequency the piezo behaves in the electrical domain like a nonlinear capacitor. The major part of the nonlinearity is the hysteresis in the voltage-charge relation. The electrical nonlinearity (voltage-charge relation) and the mechanical nonlinearity (voltage-displacement relation) originate mainly from the same dielectric hysteresis [36]. Therefore, the relation between charge and displacement is roughly linear as shown in [30] and [62]. Where the hysteresis between charge and elongation is reduced by 90 % compared to the hysteresis between voltage and elongation. A common approach to measure the charge of a piezo is to insert a sensing capacitor in series. The working principle of charge monitoring is shown in Figure 2.3. Voltage applied to the piezo results in elongation, which is roughly proportional to the charge of the piezo. The sensing capacitor in series to the piezo is equally charged. Therefore, the voltage drop over the sensing capacitor can be used to estimate the elongation.

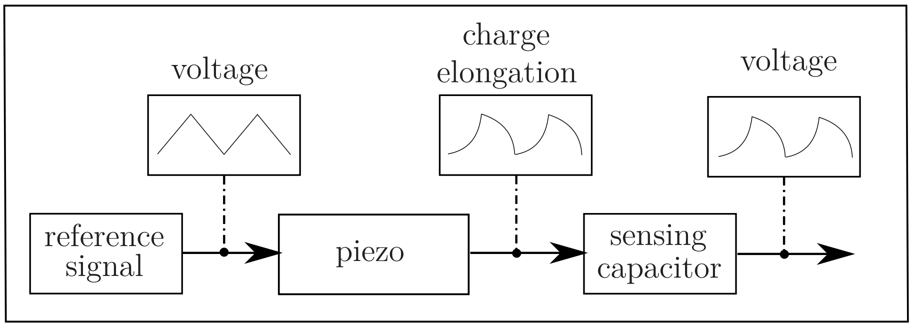

Figure 2.3: The working principle of charge monitoring is depicted. The reference voltage is applied to the piezo. The piezo responds with a nonlinear elongation. The charge of the piezo is roughly proportional to its elongation. The charge of the capacitor in series is equal to the charge of the piezo. Compared to the voltage applied to the piezo, the voltage drop over the sensing capacitor shows by 90 % reduced hysteresis to the elongation of the piezo.

When feeding back the voltage drop over the sensing capacitor a charge amplifier is built as shown in Figure 2.4. The sensing capacitor is proportionally charged to the applied voltage at the input of the charge amplifier v_{in}. The piezo C_{PZ} in series is equally charged and thereby any voltage at the input results in proportional charge at the piezo. The structure of charge or current amplifier is similar to a voltage amplifier. In case of charge or current amplification the uncontrolled nature of the output voltage is problematic. Inevitably, the circuitry contains any current offset. This DC current is integrated by the sensing capacitor. The uncontrolled sensing voltage will ramp upward and might result in saturation [63].

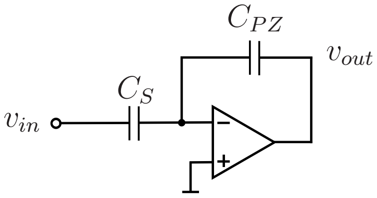

Figure 2.4: The working principle of a charge amplifier is depicted. The piezo is represented by the capacitor C_{PZ} in the electrical domain. Any voltage v_{in} applied to the input of the amplifier results in proportional charge at the sensing capacitor C_S. The piezo in series is equally charged. Thereby, the input voltage is proportional to the charge of the piezo. The figure is redrawn from [62].

Preventing charge bias between sensing element and piezo is a main challenge, when measuring the charge of piezos. Therefore, an overview is given of suggested solutions to this problem.

To avoid charge bias between the piezo and sensing capacitor additional circuitry is included to a noninverting charge amplifier [32]. With this circuitry the sensing capacitor is periodically discharged. Thereby, the hysteresis can be successfully reduced.

Nevertheless, the continuously discharging results in high frequency disturbances.

The uncontrolled output voltage of the charge amplifier is avoided by using a current source instead of a charge amplifier [33]. The charge of the piezo is controlled by switching on and off the bipolar current source for controlled intervals of time. The performance of this approach suffers from leakage current, due to dissipation of charge.

The charge amplifier is extended by an additional voltage feedback loop [63]. Thereby, charge as well as voltage is controlled, but in different frequency ranges. The amplifier controls charge above 2 Hz. This approach avoids low frequency drift sufficiently. Nevertheless, below 2 Hz the benefit of charge steering is reduced. As in this frequency range the voltage is fed back and the full hysteresis between voltage and elongation influences the performance of the approach.

A simplified approach taking advantage of the intrinsic voltage feedback of a charge amplifier is given in [62] and [29]. An inverting charge amplifier (depicted in Figure 2.5) is used to reduce the nonlinearity in the motion of a piezo. In order to have a frequency independent gain of the amplifier, resistors (R_F, R_{SC}) are inserted in parallel to the piezo C_{PZ} and the sensing capacitor C_S. By choosing resistors according to $R_F C_{PZ} = R_{SC} C_S$ the time constants are matched and a constant gain of the amplifier is ensured. Further, with this resistors the voltage is controlled at frequencies where the introduced resistors dominate the amplifier behaviour $f \ll f_{c1} = \frac{1}{2\pi R_{SC} C_S}$ with a crossover frequency in the range of 0.1 Hz. In this frequency range the amplifier works as simple voltage amplifier with the gain $\frac{v_{out}}{v_{in}} = -\frac{R_F}{R_{SC}}$. The voltage feedback at low frequencies ensures the DC stability of the circuit. On the other hand, with increasing influence of the resistors the charge amplification passes over in a voltage amplification, which results in a decreasing sensitivity of the circuit to charge below the lower boundary frequency f_{c1}. Thus, the actuator still exhibits the full hysteresis encountered between voltage and elongation in the low frequency range $f \ll f_{c1}$.

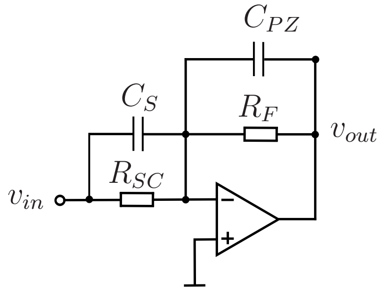

Figure 2.5: The working principle of a charge amplifier with included voltage feedback is depicted. The piezo is modeled by the capacitor C_{PZ} in the electrical domain. At high frequencies above $f_{c1} > \frac{1}{2\pi R_{SC} C_S}$ both capacitors are equally charged. Thereby, the input voltage v_{in} results in a proportional charge at the actuator. By introducing the resistors R_{SC} and R_{PC} a quasistatic feedback path is introduced, which ensures DC stability. The figure is redrawn from [62].

In an alternative approach a shunt resistor is placed in series to the piezo. To acquire charge an analog integrator can be used [64]. The current can also be integrated digitally [65], [66]. The voltage drop over the sensing resistor decreases significantly at low frequencies, as the voltage drop of the sensing resistor in series to the piezo shows high-pass characteristics. Therefore, this approaches suffer from a low signal-to-noise ratio at low frequencies. The hysteresis could be reduced by 80 % in [65], while the required SNR of 30 dB limits the minimum operational frequency to 3 Hz.

Next to the already discussed lower boundary of charge monitoring, also an upper boundary exists. In reference to [67] and [68] the behavior of charge monitoring near resonance is discussed. In Figure 2.6 the charge source q_F is introduced as it plays a major role at high frequency. The force depending charge q_F represents the influence of the mechanical domain on the electrical domain (piezoelectric effect).

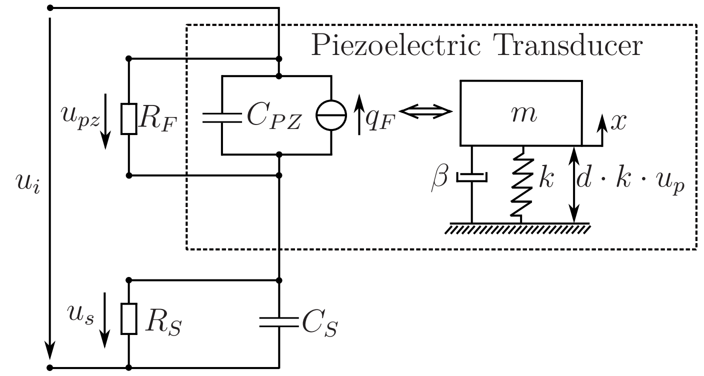

Figure 2.6: The equivalent circuit of piezos for high frequencies consists of the capacitance C_{Pz} and the force depending charge q_F. The external resistances R_F and R_S are included to match the time constant of the sensing capacitor to the time constant of piezo. The voltage u_i is applied to the piezo and the sensing capacitor C_S. The piezo is modeled as a capacitor C_{PZ} and a force depending charge q_F in the electrical domain. The charge source q_F interacts with the mechanical domain of the transducer, which is modeled as a damped mass-spring system. The sensing voltage is proportional to the charge of the piezo. Figure is based on [69].

The interplay between electrical - and mechanical domain of a piezo is described by the following relation [70]:

$$\begin{bmatrix} x(t) \\ q_{PZ}(t) \end{bmatrix} = \begin{bmatrix} K^{-1} & d \\ d & C_{PZ} \end{bmatrix} \cdot \begin{bmatrix} f_P(t) \\ u_{PZ}(t) \end{bmatrix}, \tag{2.1}$$

with displacement $x(t)$ $[m]$, mechanical stiffness K $[\frac{N}{m}]$, the charge of the piezo $q_{PZ}(t)$ $[A \cdot s]$, piezoelectric constant d $[\frac{m}{V}]$, external force $f_P(t)$ $[N]$, capacitance of the piezo C_{PZ} $[\frac{A \cdot s}{V}]$ and the voltage applied to the piezo $u_{PZ}(t)$ $[V]$. The linear, mathematical model from Equation (2.1) does not cover the non-linear properties of piezoelectric materials like creep and hysteresis. The piezo, depicted in Figure 2.6, is modeled as a second-order mass-spring-damper system in the mechanical domain [69]. The force acting on the piezo $f_p(t)$ is derived as the sum of acceleration and damping force:

$$f_p(t) = -m \cdot \frac{\partial^2 x(t)}{\partial t^2} - c \cdot \frac{\partial x(t)}{\partial t} = -m \cdot \ddot{x}(t) - c \cdot \dot{x}(t), \tag{2.2}$$

with the damping coefficient c and the mass m.

As shown in Figure 2.7 charge monitoring shows a resonance and antiresonance around the mechanical resonance of the piezo, coming from the oscillating mechanical subsystem. Above the antiresonance the charge resulting from the excitation exceeds the charge due to strain. Therefore, in this frequency range charge monitoring does not follow the elongation any longer [71], [72]. By aligning the piezo in a bridge circuit the charge resulting from strain can be extracted from the excitation charge, as shown in [67]. The mechanical eigenfrequency of the piezo with a sensing capacitor in series depends on the piezoelectric coupling and the capacitance ratio [67].

Almost all contributions in the area of charge monitoring discuss the same types of problems:

- Limitation in bandwidth due to the low frequency boundary of charge monitoring.
- Susceptibility to low frequency noise and drift due to current offset.

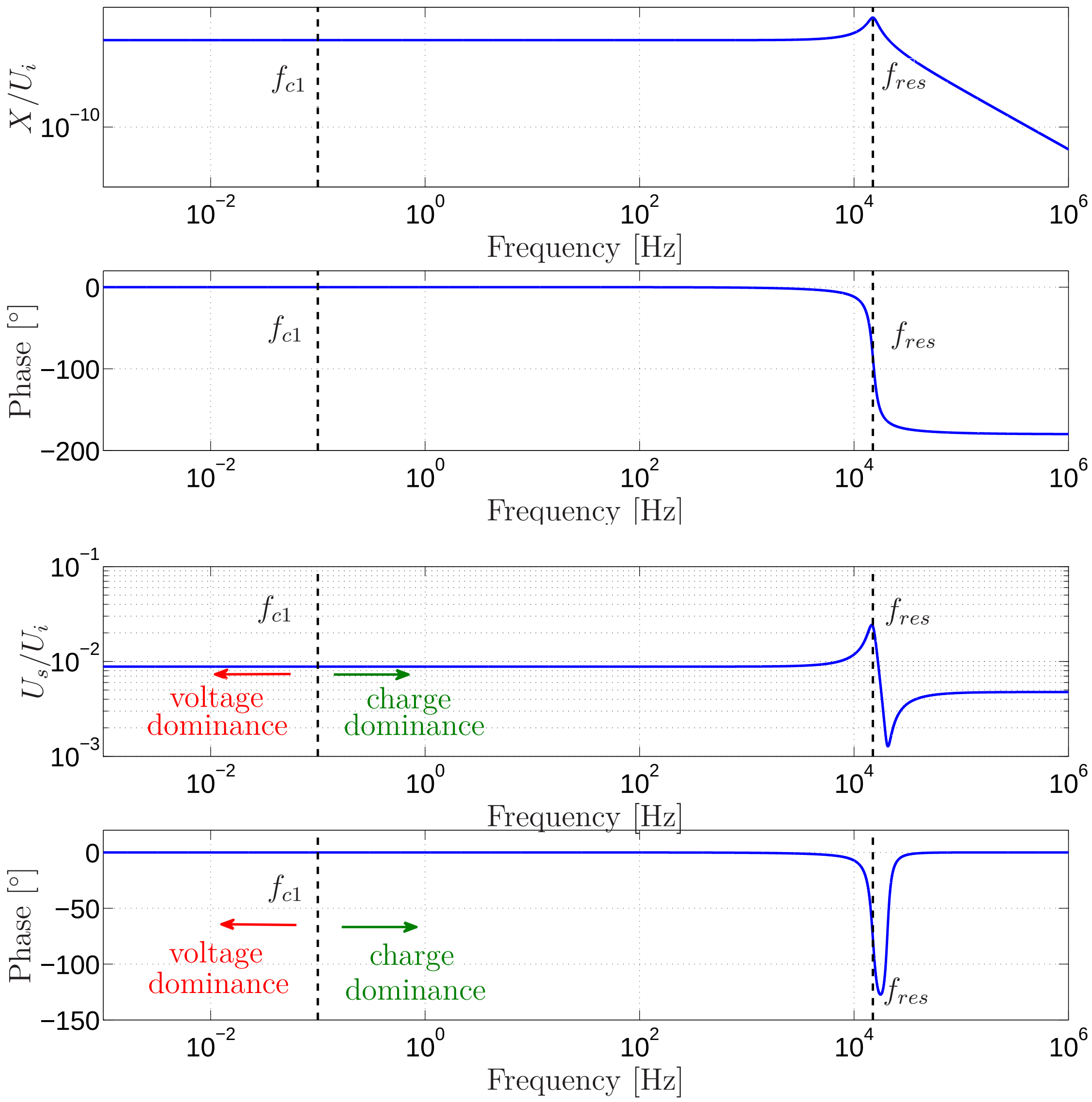

Figure 2.7: Modeled transfer function of the piezo dynamics and charge monitoring. The piezo transfer function modeled as second-order mass-spring-damper system is shown in the upper figure. The operating frequency of charge monitoring is shown in the lower figure by the modeled transfer function of u_i to u_s. Below $f_{c1} = \frac{1}{2\pi R_F C_{PZ}} = \frac{1}{2\pi R_S C_S}$ the resistors R_{SC} and R_{PZ} depicted in Figure 2.5 dominates the transfer function. The circuit behaves like a voltage resistive voltage divider below f_{c1}. Therefore, the sensitivity to charge decreases below f_{c1} [63]. At the resonance frequency of the piezo, charge monitoring shows a resonance followed by an antiresonance, coming from the oscillating mechanical subsystem. Above the antiresonance the charge resulting from excitation voltage dominates the charge due to strain, which implies a limit of charge monitoring. The output resistance of the piezo amplifier is not taken into account in this model.

2.4 Sensor fusion

A possible solution of this problem is to use a dedicated position sensor for frequencies below f_{c1}. The idea is to combine the benefits of two sensors with a complimentary filter [73], [74] shown in Figure 2.8.

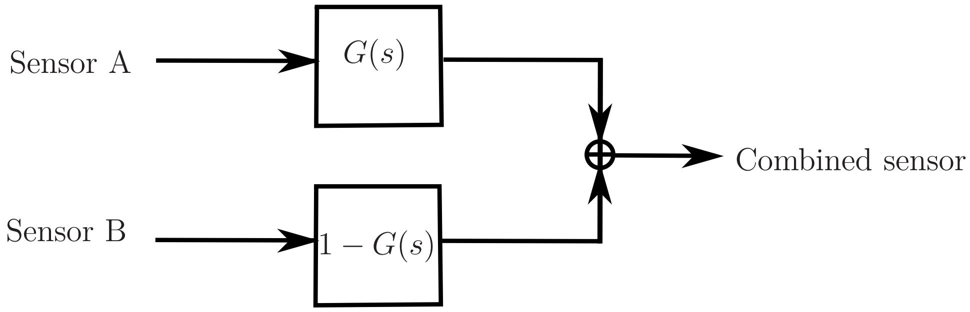

Figure 2.8: The schematic of a complementary filter is shown. Sensor A and Sensor B measure both the same physical quantity. Both sensors are based on different sensor principles and have therefore differing noise characteristics. With the filter $G(s)$ a sensor is built, which combines the benefits of both sensors. The Figure is based on [74].

Sensor fusion is a method to combine two sensor signals with different noise characteristics and thereby providing a signal with less noise than each initial sensor signal on its own. When measuring angles the benefit of sensor fusion is often used and offers a very demonstrative example. The balancing angle of an inverted pendulum can be measured for instance with a tilt sensor or a gyro sensor. The gyro sensor provides a fast response but suffers from drift due to the required integration to derive angle information from acceleration. On the other hand the tilt sensor shows a good steady state response, while it shows increased noise in the high frequency domain. Each of them alone does not fulfill the requirements. By summing the low-pass filtered gyro sensor and high pass-filtered tilt sensor the resulting signal shows moderate noise over the whole frequency range [75], [76].

Similar applications are also found in nanopositioning. A standard capacitive position sensor is combined with a strain measurement to derive a position estimate with high bandwidth and low noise [77]. Strain is obtained from an open-circuited electrode of a tube piezo. The strain voltage with a total harmonic distortion of approximately 3 % is combined with a standard capacitive sensor. Two different approaches for combining both sensor signals are presented. Linear sensor fusion is done by first-order complementary filtering. The strain voltage is high-pass filtered in order to suppress the low frequency noise of the measured strain voltage. The capacitive sensor is low-pass filtered to reduce high frequency noise at the output of the complementary filter. The crossing frequency of the noise spectral densities of both sensors are used as crossover frequency of the high and low-pass filter. The second approach of merging uses a Kalman filter and a receding horizon control.

A piezoelectric force sensor in combination with strain gages by sensor fusion creates a sensor with low noise and high stability [78]. The obtained sensor signal is used for closed-loop control of a piezo.

To increase the bandwidth, charge measurement is merged by a complementary filter with an artificial neural network in [66].

CHAPTER 3

System description

With continuously increasing requirements on nanopositioning systems also their complexity rises, which complicates the insertion of sensors during implementation and in particular, when sensors needs to be retrofitted into an existing system. Compared to the nanoresolution sensors introduced in Chapter 2, a unique characteristic of charge monitoring is that the measurement of the elongation takes place only in the electrical domain. The immediate benefit of this is, that the sensor does not need to be located directly at the actuator. Another benefit of charge monitoring are the simple read-out electronics, resulting in low-costs as well. In literature two different approaches for charge monitoring are mainly applied: insertion of a capacitor in series and integrating over the voltage drop of a resistor in series to the piezo. Both approaches are known to show less noise at increased frequency, however with the drawback of increased noise in the low frequency range. To circumvent the increased noise in the low-frequency range, charge monitoring is combined with a dedicated position sensor. Strain gages offer high DC stability and represent thereby a counterpart to charge monitoring in order to build a low noise sensor system. First typical spectra encountered in scanning systems are discussed. The properties of the stacked piezo and the tube piezo, to which charge monitoring is applied, are shown. Finally, the working principle of the sensor principle is discussed.

3.1 Motivation of the expected spectra

Before designing the experimental setup the expected signal applied to the piezo needs to be defined. Two operating situations are analysed, scanning motion and vertical actuation in closed loop.

3.1.1 Vertical actuation in the closed loop

The signal applied to the Z-piezo is a priori unknown and determined by the spatial frequency of the sample topography which is tracked due to the closed loop alignment of the Z-piezo. This signal can be separated into low frequency components with a high amplitude and high-frequency components with low magnitude as discussed in [79]. The low frequency component originates mainly from a possible tilt and large features at the sample. While the high frequency component arises mostly from the actual nanoscale topography. The sample structure consists of few big features and many small features. Therefore, large features appear with low spatial frequency, compared to small features [80]. The spatial constitution of the sample topography is transformed with the scan speed to a signal applied to the piezo. Resulting in a 1/f-behavior as shown in Figure 3.1.

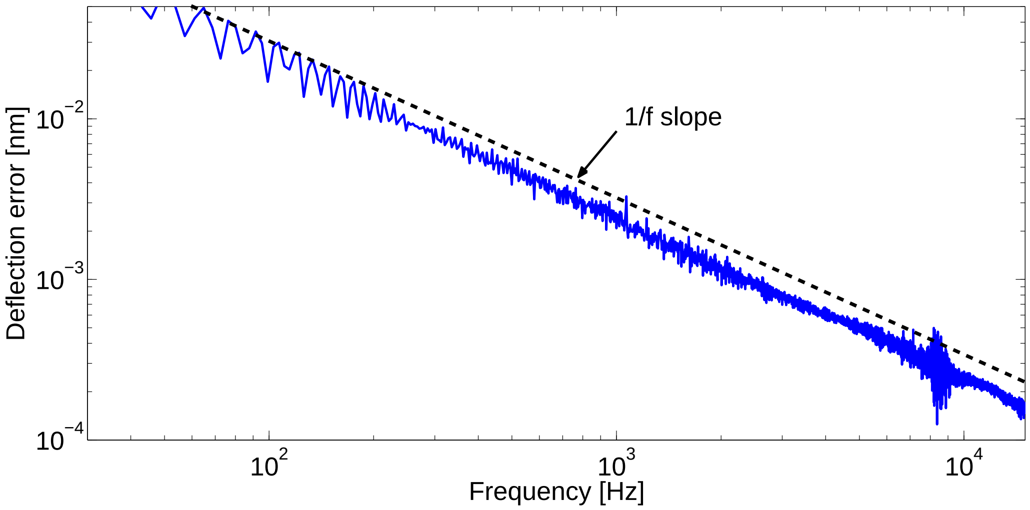

Figure 3.1: The FFT of a typical deflection error signal is shown. The error signal is recorded with a ScanAsyst-Air cantilever on a silica test grating. The spectrum follows the 1/f-slope and shows small peaks arround the resonance frequency of the used tube piezo. Figure reprinted with the permission of the author [80].

The expected amplitude spectrum of the sample topography image decreasing inversely proportional to the frequency above the line scan rate as depicted in Figure 3.2 by the red line. In addition, the spectrum of the triangular signal induced by a sample tilt is shown by the blue line.

In [29] the needed position sensor bandwidth is discussed for vertical actuators in AFM. With the aforementioned triangular scanning motion and ten features per line the position sensor bandwidth needs to be typically 20 times the line-scan rate for smooth samples and 200 times the line-scan rate for sharp samples.

3.1.2 Scanning motion

For example in AFM the tip has to be moved relative to the sample in the horizontal X-/Y-plane in order to acquire the topography. This movement is typically done in raster scan pattern as shown in Figure 1.2. In AFM the X-motion (fast scan axis) needs to track a triangular signal x_{tria} with the fundamental frequency at the line scan rate and odd higher harmonics derived as

$$x_{tria} = \hat{x}\frac{8}{\pi^2}\sum_{k=0}^{\infty}(-1)^k\frac{sin(2\pi(2k+1)\cdot f_l \cdot t)}{(2k+1)^2} \tag{3.1}$$

with f_l being the line scan rate, $\hat{x}$ the peak value of the triangular signal and k the number of the higher harmonics. The components of the fourier series of the triangular scanning signal are depicted in Figure 3.2 in black. While the Y-motion (slow scan axis) needs to track a ramp.

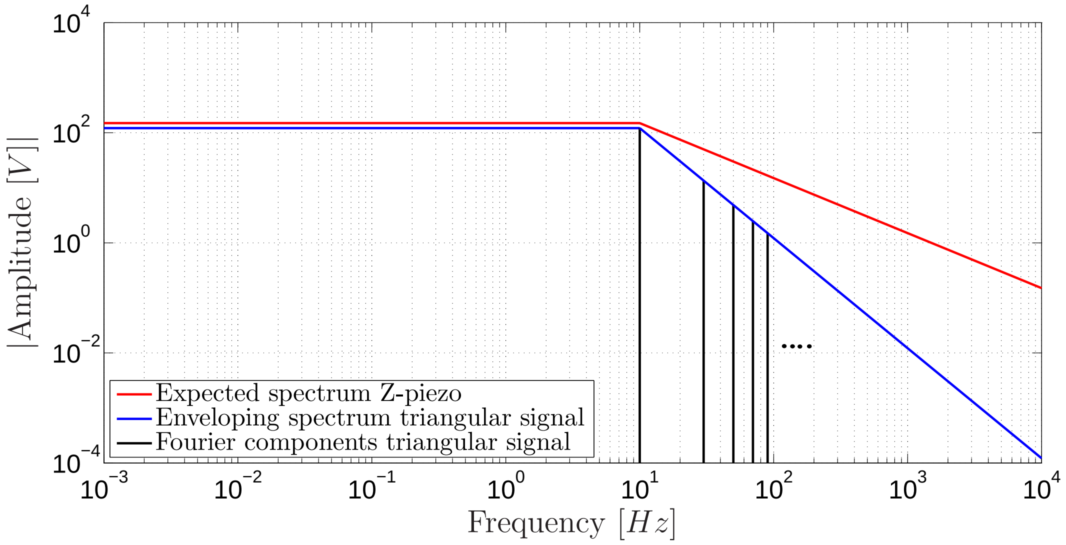

Figure 3.2: The expected spectrum applied to the Z-piezo is shown. Triangular movements of piezos are of interest in atomic force microscopy as they are used as scan signals. The fourier components of the triangular signal with a maximum voltage of 150 V is depicted by the black line. The enveloping spectrum of the fourier components is determined by the first component ($150\ V \cdot \frac{8}{\pi^2}$) below the line scan rate of 10 Hz. Above the line scan rate the amplitude spectrum of the triangular signal (blue line) decreases with a slope of -2. The spectrum shown by the red line is expected for the Z-piezo in an AFM. Up to the line scan rate of 10 Hz full range actuation is required. Above the line scan rate the spectrum is assumed to decrease with a slope of -1.

3.2 Used piezoelectric actuators

Charge monitoring is applied to the stacked piezo HPS050015 from nanoFAKTUR (Villingen-Schwenningen, Germany). The piezo, with a length of 26 mm, is prestressed and encapsulated in a stainless steel housing. The electrical capacitance of the actuator is 0.89 μF and parasitic resistance of the piezo is $R_{PZ} = 3.0\ G\Omega$, resulting in a time constant of $\tau_{PZ} = R_{PZ}C_{PZ} = 0.89\mu F \cdot 3.0G\Omega = 2670s$. The resonance frequency of the piezo is 16 kHz. The voltage range is from 0 V to 150 V and the piezo has a nominal piezoelectric constant $d = 8.2 \cdot 10^{-8} m/V$. Four strain gages with a nominal resistance of 1 $k\Omega$ are integrated and aligned in a full bridge. A 4 poles plug-and-socket connection EGG.0B.304.CLL from Lemo (Munich, Germany) provides access to the nodes of the bridge. The stacked piezo is driven by a Tech-Project piezo amplifier (Tech-Project, Vienna, Austria) with a driving voltage from 0 V to 150 V.

Next, to already introduced stacked piezo, charge monitoring is also applied to a tube piezo. For this purpose the E-scanner with a vertical range of 2.5 μm is used. The Z-piezo of the E-scanner has a capacitance of $C_{PZ} = 28\ nF$ and a time constant of $\tau = 470\ s$. The E-scanner is driven by the piezo amplifier Falco Systems WMA-02 (Falco Systems, Amsterdam, The Netherlands).

3.3 Charge monitoring

The basic concept of charge monitoring is depicted in Figure 1.4. The relation between voltage applied to the piezo and its elongation shows a nonlinear behavior. Charge measurement can be used as an estimate of elongation, with far less hysteresis than in the voltage-elongation relation. As discussed in Chapter 2 charge monitoring is limited by the first mechanical resonance towards higher frequencies and the time constant of the piezo implies a low frequency boundary.

3.3.1 Charge monitoring based on capacitor insertion

As presented in Chapter 2 the charge of a piezo can be measured by a sensing capacitor C_s inserted in series to the piezo as shown in Figure 3.3. The serial capacitor contains the same charge (Q_S) as the piezo (Q_{PZ}). With the capacitance C_S of the sensing capacitor the relation between the charge of the piezo and the voltage drop over the sensing capacitor U_S is derived as

$$Q_{PZ} = U_{PZ}C_{PZ} = Q_S = U_S C_S. \tag{3.2}$$

The piezo and the sensing capacitor form a capacitive voltage divider. The voltage drop across the sensing capacitor C_S reduces the voltage applied to the piezo. Thereby, the stroke of the piezo is reduced. This can be compensated by a higher amplification factor of the piezo amplifier. The tolerable loss of voltage range and maximum input voltage of the sensor electronics determine the lower limit of the capacitance C_S. On the other hand, a high sensing capacitor results in a low voltage drop over the sensing capacitor. Thus, the sensing voltage needs to be amplified to meet the required sensor signal magnitude. However, this leads to additional noise. With a ratio of 100 between sensing capacitor and piezo capacitance both requirements can be fulfilled, as 1 % loss in voltage is acceptable and only small amplification is needed to reach the required sensor signal magnitude.

Below the frequency f_{c1} the desired ratio between the voltage drop over the sensing capacitor and the piezo is not fulfilled any longer as the parasitic resistances (R_S

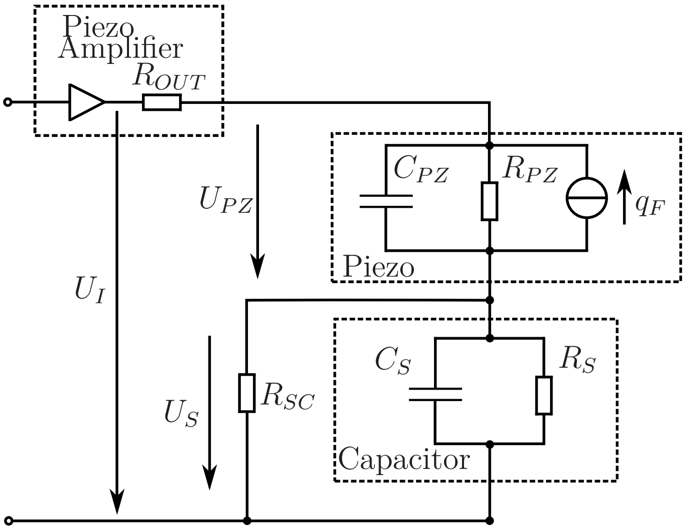

Figure 3.3: The circuit of charge monitoring with capacitor insertion is shown. The piezo amplifier has an output resistance R_{OUT}. The equivalent circuit of the piezo consists of the capacitance C_{PZ}, the parasitic resistance R_{PZ}, and the force depending charge q_F. The sensing capacitance C_S is applied in series to the piezo to measure the charge of the piezo. In order to match the time constants of the sensing path to the piezo the resistance R_{SC} is included.

and R_{PZ}) dominates the behavior of the circuit. The parasitic resistance of piezos and its dependency on humidity, temperature and electrical field is discussed in [81]. The time constants of the piezo and the sensing capacitor are generally not equal $R_{PZ}C_{PZ} \neq R_S C_S$. Thereby, the voltage drop over the sensing capacitor would be frequency-dependent. To maintain a constant voltage drop over frequency, the time constants are matched $R_{PZ}C_{PZ} = C_S(R_S \parallel R_{SC})$ by introducing an external resistor R_{SC} in parallel to the sensing capacitor. The voltage applied to the piezo related to the voltage drop over the sensing path with R_{SC} in parallel is derived as

$$\frac{U_{PZ}}{U_S} = \frac{R_{PZ}}{R_S \parallel R_{SC}} \frac{1 + sC_S(R_S \parallel R_{SC})}{1 + sC_{PZ}R_{PZ}} = \frac{100}{1}. \tag{3.3}$$

After matching the time constants of the piezo and the sensing path, the transfer function of Equation (3.3) becomes independent of frequency. Above the lower boundary $f \gg f_{c1} = \frac{1}{2\pi C_S(R_S \| R_{SC})} = \frac{1}{2\pi C_{PZ}R_{PZ}}$ the transfer function from Equation 3.3 results in

$$\frac{U_{PZ}}{U_S} = \frac{C_S}{C_{PZ}}. \tag{3.4}$$

With Equation (3.2) and (3.4) the voltage drop over the sensing capacitor is derived as $U_S = \frac{Q_{PZ}}{C_S}$. The sensing voltage, which is proportional to the charge of the piezo, can be used as estimate of the elongation.

For frequencies $f \ll f_{c1}$ the transfer function from Equation (3.3) results in

$$\frac{U_{PZ}}{U_S} = \frac{R_{PZ}}{R_S \parallel R_{SC}}. \tag{3.5}$$

In this frequency range the resistors dominate the circuit, which works as a resistive voltage divider. Below f_{c1} the sensing voltage U_S is proportional to the voltage applied to the piezo and shows the full nonlinearities.

3.3.2 Charge monitoring based on current integration

As alternative to the previous mentioned technique a shunt resistor R_{SH} can be applied in series to the piezo as shown in Figure 3.4. The voltage drop over the sensing resistor

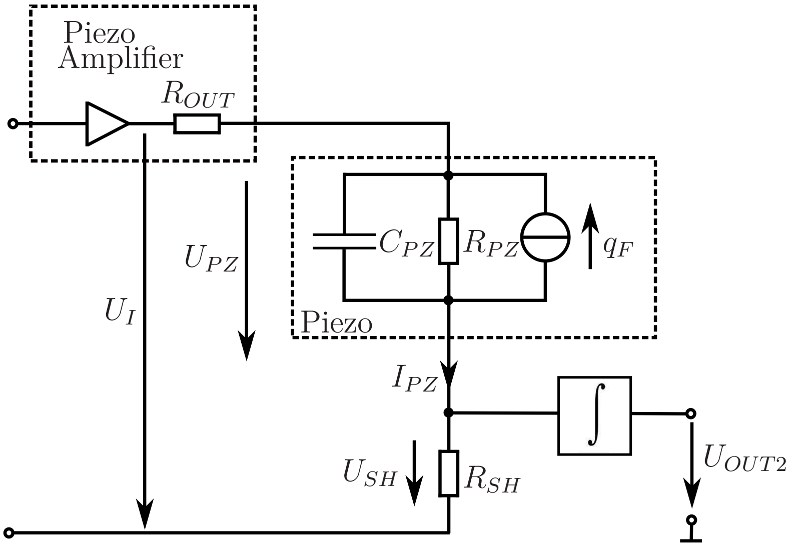

Figure 3.4: The circuit of charge monitoring via current integration is shown. The piezo amplifier has an output resistance R_{OUT}. The equivalent circuit of the piezo consists of the capacitance C_{PZ}, the parasitic resistance R_{PZ} and the force depending charge q_F. The shunt resistor R_{SH} is used to measure the current through the piezo. The current is integrated to acquire the charge as estimation of the elongation.

U_{SH} is proportional to the current through the piezo

$$U_{SH} = R_{SH} I_{PZ} \tag{3.6}$$

The voltage drop is integrated with an analog integrator.

$$U_{OUT2} = \int I_{PZ} R_{SH} \, \mathrm{d}t \tag{3.7}$$

The output voltage U_{OUT2} is proportional to the charge of the piezo. Below the resonance the current I_{PZ} is composed by the derivative of the charge Q_{PZ} and the leakage current over the parasitic resistance R_{PZ}. For frequencies $\omega < \frac{1}{R_{PZ}C_{PZ}}$ the leakage current over the parasitic resistance R_{PZ} of the piezo contributes significantly to the current I_{PZ}. Therefore, charge monitoring via current integration shows the same lower boundary $f_{c1} = \frac{1}{2\pi R_{PZ}C_{PZ}}$ as charge monitoring via capacitor insertion.

In the operating frequency of charge monitoring the voltage drop over the shunt resistor U_{SH} is derived as:

$$U_{SH}(s) = U_I(s)\frac{R_{SH}C_{PZ}s}{R_{SH}C_{PZ}s + 1} \tag{3.8}$$

In order to obtain a high signal-to-noise ratio at the shunt resistor U_{SH} a high resistance R_{SH} is beneficial. Nevertheless, the voltage drop over the shunt resistor must not exceed the maximum input voltage of the analog integrator and thus introduces a constraint on the maximum value of the shunt resistor.

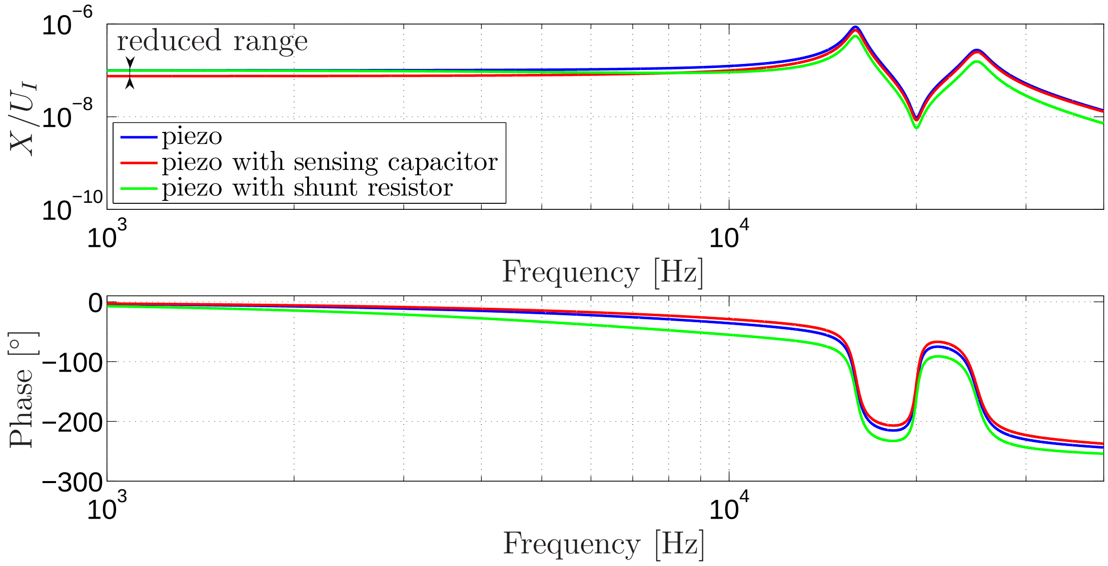

Figure 3.5: The influence of a pole introduced by the serial resistance and the capacitive load is shown by the modeled transfer function. When the piezo amplifier is applied to the piezo without charge monitoring the pole's crossover frequency is determined by the output resistance of the piezo amplifier and the capacitance of the piezo. The elongation resulting from the low-pass filtered input voltage is shown by the blue, continuous line. With the shunt resistor (exemplary chosen equal the output resistance of the amplifier) in series the resulting resistance is doubled resulting in a decreased crossover frequency and more phase lag in the elongation (green continuous). Compared with this the sensing capacitor in series reduces the load capacitance and thereby increases the crossover frequency of the low-pass filter (red). Further, the sensing capacitance results in a reduced voltage at the piezo, evidenced by a lower elongation at low frequencies.

The output resistance of the piezo amplifier R_{OUT} and the capacitance build a low-pass filter from U_I towards U_{PZ}. Without any charge monitoring applied to the piezo the crossover frequency of the low-pass filter is derived as

$$f_{LP} = \frac{1}{2\pi R_{OUT} C_{PZ}}. \tag{3.9}$$

The modeled transfer function from U_I towards the piezo elongation X is depicted by the blue, continuous line.

When doing charge monitoring via current integration, the introduced shunt resistor reduces the crossover frequency of the low-pass filter to

$$f_{LP} = \frac{1}{2\pi (R_{OUT} + R_{SH}) C_{PZ}}. \tag{3.10}$$

The reduced pole results in an increased phase lag between piezo amplifier output voltage and elongation, depicted by the green, continuous line. When using charge monitoring in a closed loop the phase-lag results in an reduced phase margin. The acceptable reduction of phase margin implies a second restriction to the maximum value of the shunt resistor, next to the maximum voltage drop.

For charge monitoring via capacitor insertion the voltage applied to the piezo is reduced by the factor $\frac{C_S}{C_S+C_{PZ}}$, due to the capacitive voltage divider, which is visible in the transfer function as reduced value at low frequencies (red line). Insertion of the sensing capacitor results in an increased crossover-frequency

$$f_{LP} = \frac{1}{2\pi R_{OUT} \frac{C_{PZ} C_S}{C_{PZ}+C_S}}, \tag{3.11}$$

by the costs of an reduced voltage shown in red dashed.

A shunt resistor in series shows fundamental influence on the system, due to reduced phase margin. Compared to that, the voltage drop over a sensing capacitor can be easily compensated by an increased gain of the piezo amplifier.

3.4 Resistive strain gage measurement

Strain gages are simple, of low cost and easy to integrate into an existing system. Therefore, they are used to overcome the low frequency concerns of charge monitoring.

3.4.1 Construction and working principle

The considerations in this section are based on [82] and [56]. Strain gages consist of thin flexible carrier materials with deposited wire or film resistors. In order to increase its sensitivity they are manufactured in meanderlike structures as shown in Figure 3.6. Thereby, a high sensitivity in one direction is achieved, while the overall dimension is kept within practical limits. The resistance R of an electrical conductor depends on

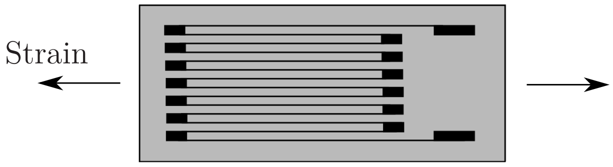

Figure 3.6: A typical arrangement of the conducting material on a thin film strain gage. High sensitivity in one direction is reached by the meanderlike structure. The figure is redrawn from [56].

its length l, its cross section A and the electrical resistivity ρ of the material:

$$R = \frac{\rho l}{A} \tag{3.12}$$

Any stretching or compression changes the resistance. By substituting the cross section A in Equation (3.12) with the diameter D the linearized relative change in resistance is derived as:

$$\begin{aligned} \frac{\Delta R}{R} &= \frac{1}{R}\frac{\partial R}{\partial l}\Delta l + \frac{1}{R}\frac{\partial R}{\partial D}\Delta D + \frac{1}{R}\frac{\partial R}{\partial \rho}\Delta \rho \\ &= \frac{\Delta l}{l} - 2\frac{\Delta D}{D} + \frac{\Delta \rho}{\rho} \end{aligned} \tag{3.13}$$

The ratio between relative change in resistance and strain is designated as gage factor:

$$K = \frac{\frac{\Delta R}{R}}{\frac{\Delta l}{l}} = 1 - 2\frac{\frac{\Delta D}{D}}{\frac{\Delta l}{l}} + \frac{\frac{\Delta \rho}{\rho}}{\frac{\Delta l}{l}} \tag{3.14}$$

The second term in Equation (3.14) describes the ratio between transverse and longitudinal strains. This term is named poisson ratio. The first two terms provide a gauge factor in the range of 1.4 to 2 based on the change in geometry. Strain gages can consist of metallic or semiconductor materials. The change in resistance (third therm) results in a gage factor in the order of 0.3 for metals [57].

3.4.2 Wheatstone bridge

Accurately measurement of small changes in resistance is a significant challenge when applying resistive sensors. One approach is to use a wheatstone bridge as shown in Figure 3.7. A full-bridge design is beneficial as it shows the highest sensitivity and introduces no further nonlinearities as shown in Equation (3.16). The bridge output voltage U_d from Figure 3.7 is derived as:

$$U_d = I_0 \frac{R_3 R_2 - R_1 R_4}{R_1 + R_2 + R_3 + R_4} \tag{3.15}$$

with $R_1 = R_4 = R_0 - \Delta R$ and $R_2 = R_3 = R_0 + \Delta R$ the bridge output voltage is:

$$U_d = I_0 \Delta R. \tag{3.16}$$

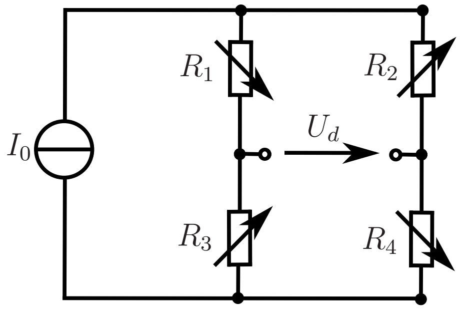

Figure 3.7: In order to measure small changes in resistance the strain gages are arranged in a Wheatstone Bridge. The upward and downward arrows in the resistors indicate an increase and decrease in resistance with increasing strain respectively.

The bridge output voltage is proportional to the change in resistance (ΔR) and to the current source (I_0). As long as all four strain gages are suspended to the same temperature, any change in resistance originating from temperature fluctuations influences all four strain gages at the same extent. Therefore, the bridge circuit is insensitive to temperature changes.

The full scale bridge output is expected to be in the range of 10 mV. Larger excitation current would result in proportionally higher bridge output voltage. Nevertheless the excitation is limited by the power dissipation of the strain gages. Excessively high excitation results in unwanted self heating error. Therefore high amplification in the conditioning circuitry is unavoidable. Even though sensitivity to thermal noise of the strain gages and noise of the conditioning circuitry is increased. In addition to noise also the input resistance of the conditioning circuitry is of interest. Any influence of the input resistance would be interpreted as apparent strain. The bridge output voltage U_d contains a high DC voltage. Therefore, also the common mode rejection ratio of the differential amplifier, which acquires the voltage U_d, is of interest.

3.5 Summary of system description

Although the signal applied to the vertical piezoelectric actuator is a priori unknown an expectation of the applied spectra is deduced. The expected spectra at the Z-piezo has full range amplitude up to the line scan rate and decreases with a slope of -1 above the line scan rate, while the spectrum of the scanning motion decreases with a slope of -2. The required sensor bandwidth for a typical line scan rate of 10 lines per second is 2 kHz.

To measure the elongation of the discussed piezos charge monitoring and strain gage measurement is considered.

Charge monitoring via current integration introduces phase lag in the actuator motion due to shifting the pole originating from the amplifier resistance, shunt resistance and piezo capacitance to a lower frequency. Any voltage drop over the shunt resistor or inserted capacitor reduces the voltage applied to the piezo. For low frequencies the voltage applied to the piezo is not reduced remarkably by the shunt resistor in series. On the other hand, the inserted capacitor shows a constant voltage drop of approximately 1 %. By applying a higher supply voltage the original elongation still can be reached. The obtained sensor bandwidth is determined by the time constant of the piezo and its resonance frequency and therefore equal for either of the introduced approaches.

Strain measurement via strain gages is not limited in bandwidth in the considered frequency range. Both before introduced charge monitoring approaches are based on a configuration, where neither of the electrodes of the piezo is grounded. Such configuration is applicable only if it is possible to use a floating load.

CHAPTER 4

Experimental setups and noise analysis

This Chapter starts with a general discussion of random signals. Followed by the discussion of the implemented setups of both charge monitoring approaches and the strain measurement with resistive strain gages. Based on the deduced circuit a noise model is derived. The noise model is used to determine qualitatively the noise contribution over frequency and the main contributors to the noise at the output in the different frequency ranges. Thereby, the required quality and magnitude of the used components can be assessed upfront. The derived noise model is compared with the measured Noise Spectral Density (NSD).

4.1 Noise analysis

The mathematical description of random signals is discussed in this section, further noise sources faced in charge monitoring are introduced and their transmission through linear systems of the sensor electronics is discussed. The considerations in this section are based on [83], [84] and [19].

4.1.1 Mathematical description of random signals

The definition for noise given in [85] is:

> "Unwanted disturbances superimposed upon a useful signal, which tend to obscure its information context. Random noise is the part of the noise that is unpredictable, expect in a statistic way."

In general a random variable $A(t)$ is not reproducible, nevertheless it can be described by statistical methods.

Mean, power and variance

A statistical variable can be described by the following parameters. $\overline{A}$ is the average, mean or expected value of the random signal $A(t)$.

$$\overline{A} = \lim_{T\to\infty} \frac{1}{2T} \int_{-T}^{T} A(t)\,\mathrm{d}t. \tag{4.1}$$

The fluctuation $a(t)$ of $A(t)$ around the mean value is

$$a(t) = A(t) - \overline{A}. \tag{4.2}$$

As the mean of $a(t)$ is zero by definition, the extent of the fluctuation around the mean value is described by its mean square value:

$$\sigma^2 = \overline{a(t)^2} = \lim_{T\to\infty} \frac{1}{2T} \int_{-T}^{T} [a(t)]^2\,\mathrm{d}t. \tag{4.3}$$

The value σ^2 is referred to as variance and its root σ is designated as standard deviation. The variance and standard deviation represents the power and root mean square value of the fluctuation around the mean. In electrical signal the variance is the noise power in the signal. The variance σ^2 can also be expressed by the random signal $A(t)$ by substitution of Equation (4.2) in Equation (4.3)

$$\sigma^2 = \overline{a^2} = \overline{(A-\overline{A})^2} = \overline{A^2} - \overline{2A\overline{A}} + \overline{A}^2 = \overline{A^2} - 2\overline{A}^2 + \overline{A}^2 = \overline{A^2} - \overline{A}^2. \tag{4.4}$$

with $\overline{A^2}$ is the total power of the random signal and $\overline{A}^2$ is the power of the mean value.

Autocorrelation

From the preceding considerations it is concluded, that the value of a random variable is not predictable. Nevertheless, a known value at the instance of time t_1 permits certain probability statements about the value at the instant of time $t_2 = t_1 + \tau$. The autocorrelation function

$$\rho(\tau) = \overline{a(t_1)a(t_1+\tau)} = \lim_{T\to\infty} \frac{1}{2T} \int_{-T}^{T} a(t_1)a(t_1+\tau)\,\mathrm{d}t_1 \tag{4.5}$$

describes how well the process is correlated with itself at two different instants of time. For any stationary process the autocorrelation function is time invariant, and thereby depends only on the time difference $\tau = t_2 - t_1$ [83]. Dynamic error budgeting is used to identify performance limiting disturbances in the frequency domain. Therefore a representation of the autocorrelation function in the frequency domain is needed. In reference to Equation (4.5) the following qualitative statement about the autocorrelation function is made. For any autocorrelation function decreasing rapidly in time, the process changes rapidly. Vice versa slowly changing processes are characterized by autocorrelation functions, which are slowly decreasing with τ. Thus the autocorrelation function contains spectral information of the fluctuating signal.

Power spectral density

The fourier transform of the autocorrelation and its inverse are defined as:

$$s(f) = \int_{-\infty}^{\infty} \rho(\tau) e^{-2\pi j f \tau} \, \mathrm{d}\tau \tag{4.6}$$

and

$$\rho(\tau) = \int_{-\infty}^{\infty} w(f) e^{2\pi j f \tau} \, \mathrm{d}f. \tag{4.7}$$

Insertion of $\tau = 0$ in Equation (4.7) results in

$$\rho(0) = \int_{-\infty}^{\infty} s(f) \, \mathrm{d}f. \tag{4.8}$$

By comparing Equation (4.5) and (4.3), it is noticed that $\rho(0) = \overline{a^2}$. Thereby, it emerges that $s(f)$ has to be the two-sided power spectral density. The integration over the frequency range of interest is equal to the total noise power in the respective bandwidth, as shown in Equation (4.8). The two-sided power spectral density is even, because the autocorrelation of Equation (4.5) is even as well. Thereby, the single-sided power spectral density $S(f)$ can be defined [84]:

$$S(f) = \begin{cases} s(0) & \text{if } f = 0 \\ 2s(f) & \text{if } f > 0. \end{cases} \tag{4.9}$$

With the single-sided power spectral density of Equation (4.9) and Equation (4.6) the Wiener-Khinchin theorem is exposed

$$S(f) = 2 \int_{-\infty}^{\infty} \rho(\tau) e^{-2\pi j f \tau} \, \mathrm{d}\tau. \tag{4.10}$$

Correlation

Practically every electronic component introduces noise. Therefore, the noise observed at the output results from the superposition of many elementary fluctuations. These elementary fluctuations can show a dependency between each other. In the case of two fluctuating signals with zero mean the variance of their sum is derived as:

$$\overline{(a_1 + a_2)^2} = \overline{a_1^2} + \overline{a_2^2} + \overline{2a_1 a_2} = \sigma_1^2 + \sigma_2^2 + 2c_{12}\sigma_1\sigma_2 \tag{4.11}$$

with σ_1^2 and σ_2^2 the variances of those signals on their own and c_{12} the crosscorrelation coefficient. Let us consider a series connection of two resistors. When the fluctuation a_1 and a_2 originate from the thermal noise of the resistors, their crosscorrelation is zero, as they are based on different noise processes. Thereby the resulting variance σ_{12}^2 is simply the sum of the variances

$$\sigma_{12}^2 = \sigma_1^2 + \sigma_2^2. \tag{4.12}$$

On the other hand, if the fluctuations a_1 and a_2 originate from a current noise, they are correlated due to the same current noise source. Their correlation coefficient in

Equation (4.11) has to be taken into account in order to determine the resulting variance.

4.1.2 Typical noise sources

There exists many different sources of electronic noise. The two most crucial for the considered mechatronic system are thermal noise and 1/f-noise, which originates from fluctuating conductivity. Thermal noise in circuits is simply brownian motion of charge carriers. Therefore any appearance of brownian motion is taken into account in the electrical domain as thermal noise.

Thermal noise

Charge carriers in conductors and semiconductors show a thermally induced, random movement. In consequence to the charge carrier motion, the electrodes of the conductor are fluctuated charged, which leads to fluctuating potential difference across its ends. Thermal noise (also known as Johnson or Nyquist noise) is modeled as a noiseless resistor in series with a noise creating voltage source as depicted in Figure 4.1. The noise creating voltage source has a power spectral density of

$$S_V(f) = 4 \cdot k_B \cdot T \cdot R, \tag{4.13}$$

with k the Boltzmann's constant ($1.38 \cdot 10^{-23} J/K$), T $[K]$ the temperature and R $[\Omega]$ the resistance. The power spectral density from Equation (4.13) is independent from the frequency and shows a Gaussian amplitude distribution, hence designated white, gaussian noise. By multiplying the power spectral density with the noise bandwidth Δf and taking the square root of it, the RMS noise voltage is derived as

$$U_{nrms} = \sqrt{\overline{u^2}} = 2 \cdot \sqrt{k_B \cdot T \cdot R \cdot \Delta f}. \tag{4.14}$$

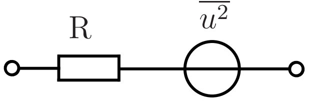

Figure 4.1: The equivalent circuit of a resistor with thermal noise consists of a noiseless resistor with a noise-creating voltage source in series. The figure is redrawn from [83].

1/f-noise

When current passes trough a resistor or semiconductor the noise level rises above thermal noise. This exceeding noise is called 1/f-noise (also known as flicker or excess noise). It is based on fluctuating conductivity originating from imperfect contact between two materials. As the name 1/f-noise already reveals its power spectral density increases with decreasing frequency:

$$S_E(f) = \frac{K_f}{f^{\alpha}} \tag{4.15}$$

with K_f depending on the material and the average voltage drop over the resistor and the exponent α typically between 0.8 and 1.4. For approximations the exponent α is often set to unity. The noise power P in the spectrum between f_1 and f_2 is given by

$$P = \int_{f_1}^{f_2} S(f) \cdot \mathrm{d}f. \tag{4.16}$$

In case of 1/f-noise with $\alpha = 1$, the noise power from Equation (4.17) is derived by inserting Equation (4.15) in Equation (4.16) as

$$P = \int_{f_1}^{f_2} \frac{K_f}{f} \cdot \mathrm{d}f = K_f \cdot \ln\left(\frac{f_2}{f_1}\right). \tag{4.17}$$

For any constant, relative frequency spectrum (f_1, $f_2 = a \cdot f_1$) the noise power is

$$P = K_f \cdot \ln(a). \tag{4.18}$$

Hence the power in a certain relative frequency spectrum (for instance one decade) of 1/f-noise is independent of the absolute frequency. The constant noise power in every decade is used by manufacturers to specify the 1/f-noise as a noise index C_R $[\frac{\mu V}{V}]$:

$$C_R = \frac{\sigma_u \cdot 10^6}{\overline{u}} \tag{4.19}$$

4.1.3 Summing up uncorrelated noise

Thermal noise and 1/f-noise noise arise from different physical processes. Hence they are uncorrelated. The resulting power spectral density $S(f)$ of thermal noise $S_V(f)$ with overlaying 1/f-noise $S_E(f)$ is derived as:

$$S(f) = S_V(f) + S_E(f). \tag{4.20}$$

The frequency f_{nc} at which the power spectral density of 1/f-noise dominates the thermal noise power spectral density is called 1/f-corner frequency and is depicted in Figure 4.2.

4.1.4 Response of linear systems to random inputs

In order to carry out dynamic error budgeting it is essential to determine the transmission of noise through linear systems. The power spectral density is proportional to the square of the amplitude of the fluctuation $a(t)$. Therefore the power spectral density at the output of a linear system is proportional to the square of the magnitude frequency response. With $S_x(f)$ the power spectral density at the input of a linear system with the transfer function $H(f)$, the power spectral density at the output $S_y(f)$ is derived

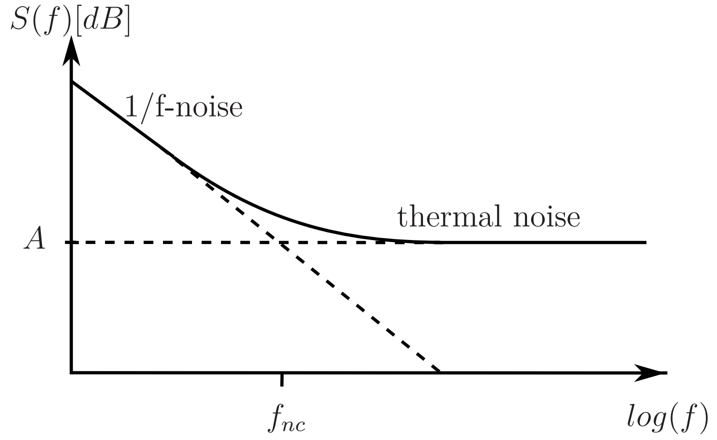

Figure 4.2: Typically, white noise and 1/f noise are detected at the output of active components. Below the corner frequency f_{nc} 1/f-noise dominates over white noise. The figure is redrawn from [50].

as

$$S_y(f) = |H(f)|^2 \, S_x(f). \tag{4.21}$$

4.2 Experimental setup

Based on the used piezos and expected spectra from Chapter 3, the setups for both charge monitoring approaches and the displacement measurement with strain gages is discussed in the following.

4.2.1 Experimental setup charge monitoring via capacitor applied to stacked piezo

The experimental setup is depicted in Figure 4.3. As the piezo has a capacitance of $C_{PZ} = 0.89\ \mu F$, a sensing capacitor with $C_S = 89\ \mu F$ is required in order to fulfill the ratio of 100 between sensing capacitor and piezo capacitance. Due to availability an actual sensing capacitance of 100 μF is used with a parasitic resistance $R_S = 8.4\ G\Omega$. According to Equation (3.2) the linear relationship between Q_P and U_S depends on the linearity of the used sensing capacitor. The most crucial nonlinearity in capacitors originates from dielectric absorption [41], [86]. To avoid this error source, metalized polypropylene film capacitors with a very low dielectric absorption (0.05 %) are used for charge monitoring. To adapt the time constants of the sensing path to the time constant of the piezo a resistance $R_{SC} = 27\ M\Omega$ is applied in parallel to the sensing capacitor C_S. The lower boundary of charge monitoring is derived by the time constant of the piezo

$$f_{c1} = \frac{1}{2\pi R_{PZ} C_{PZ}} = \frac{1}{2\pi \cdot 3\text{G}\Omega \cdot 0.89\mu\text{F}} = 6.0 \cdot 10^{-5}\ \text{Hz}. \tag{4.22}$$

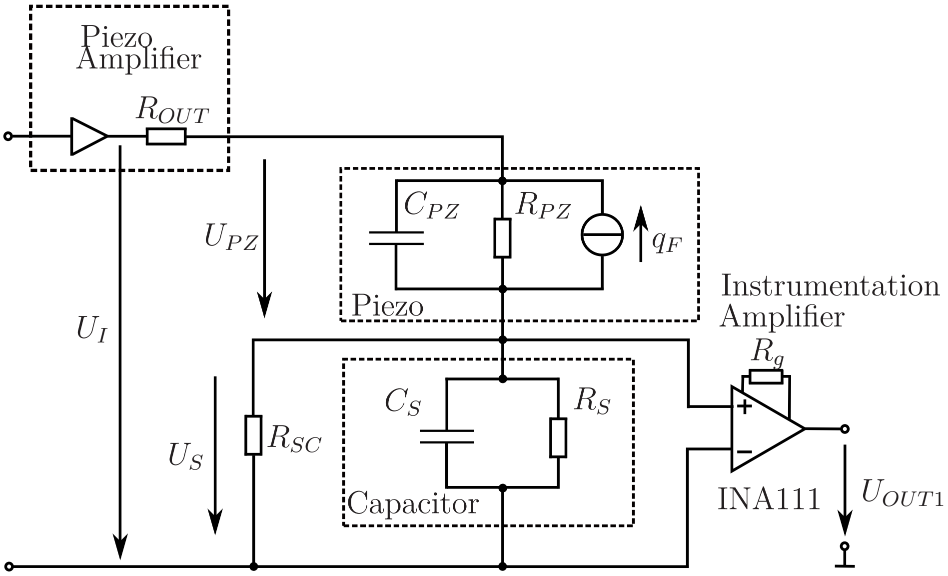

Figure 4.3: The used setup for charge monitoring via capacitor insertion is shown. The equivalent circuit of the piezo consists of the capacitance C_{PZ}, the parasitic resistance R_{PZ}, and the force depending charge q_F. The sensing capacitance C_S is applied in series to the piezo to measure the charge of the piezo. In order to match the time constants of the sensing path to the piezo the resistance R_{SC} is included. To amplify and acquire the voltage drop over the sensing capacitor an in-amp INA111 is used.

The required sensitivity of the introduced sensor is 0.52 $\frac{V}{\mu m}$, in order to obtain a measurement in the range of common electronic signals. From the first line of Equation (2.1) and Equation (3.2) the sensitivity between the sensing voltage U_S and the elongation of the piezo x is derived as:

$$\frac{U_s}{x} = \frac{C_{PZ}}{C_S d} = \frac{0.89\mu F}{100\mu F \cdot 8.2 \cdot 10^{-8} m/V} = 0.11 \frac{V}{\mu m} \tag{4.23}$$

with the piezoelectric constant $d = 8.2 \cdot 10^{-8} m/V$. Theoretically, a gain of 4.7 is computed to reach the desired sensitivity. To record the voltage drop over the sensing capacitor an instrumentation amplifier INA111 from Texas Instruments (Dallas, United States) is used, as it offers low noise and a high input resistance. For the practical implementation a gain of the instrumentation amplifier of $G_{INA1} = 3.7$ ($R_g = 18.7\ k\Omega$) is used, to reach the required sensitivity. The decreased required amplifier gain in the practical implementation arises from a deviation between nominal and real piezoelectric constant.

4.2.2 Experimental setup charge monitoring by current integration applied to stacked piezo

The resistance of the shunt resistor (R_{SH} in Figure 4.4) is of high importance. On the one hand a high shunt resistance results in a high desired Signal-to-Noise Ratio (SNR) at the output U_{OUT2}. On the other hand the shunt resistance needs to be sufficiently low to keep the maximum voltage drop within the operating range of the instrumentation amplifier. Further, the shunt resistor introduces a phase shift between applied voltage and elongation, similar to the output resistance of the piezo amplifier, which limits the phase margin when applied in closed-loop control.

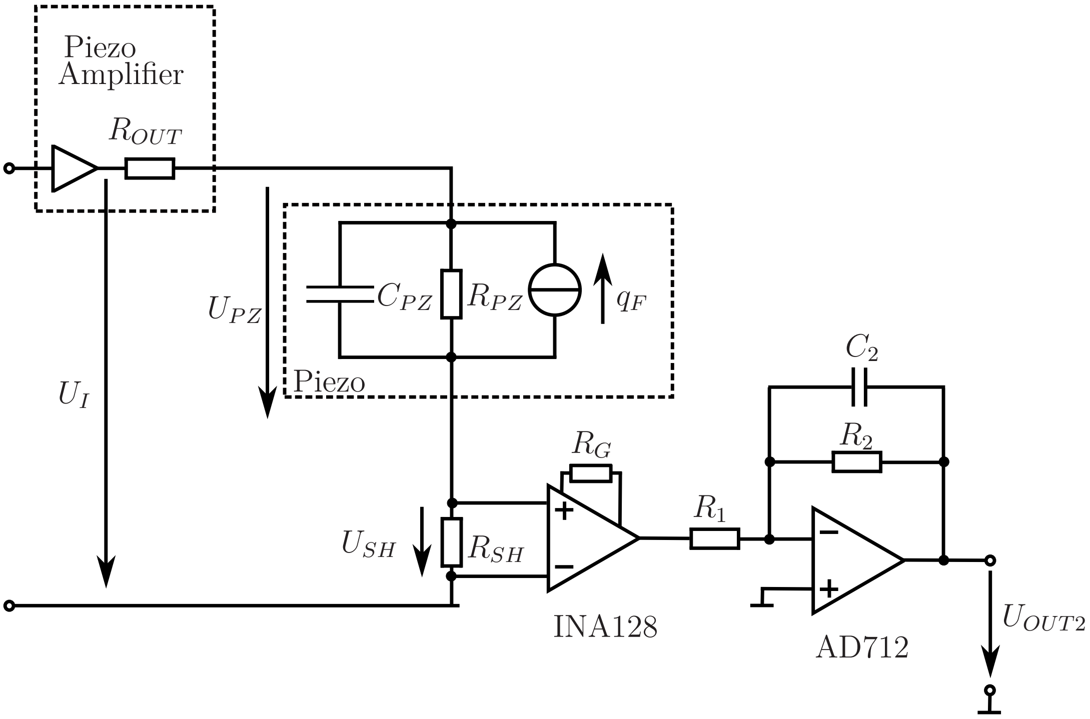

Figure 4.4: The setup for charge monitoring via current integration is shown. The equivalent circuit of the piezo consists of the capacitance C_{PZ}, the parasitic resistance R_{PZ} and the force depending charge q_F The shunt resistor R_{SH} is used to measure the current through the piezo. The voltage drop over R_{SH} is acquired with an in-amp (INA128) and integrated via the inverting integrator, built with the op-amp AD712. The resistor R_2 prevents the integrator from saturation.

With the output resistance R_{OUT} of the piezo amplifier taken into account, the voltage drop over the shunt resistor U_{SH} is derived as:

$$|U_{SH}| = U_I \frac{\omega R_{SH} C_{PZ}}{\sqrt{1 + (\omega C_{PZ}(R_{OUT} + R_{SH}))^2}}. \tag{4.24}$$

The amplitude spectrum applied to the Z-piezo is full range up to the line scan rate and decreases in most cases inversely proportional to the frequency above the line scan rate as depicted in Figure 3.2 by the red line. The maximum voltage drop over the shunt resistor arises at the line scan rate (10 Hz) and maximum voltage (150 V) applied to the piezo. This voltage drop needs to be in the operating range of the instrumentation amplifier. With the operating range of the instrumentation amplifier of ±12 V the maximum value of the shunt resistor is derived as 1435 Ω, by solving the quadratic Equation (4.24).

Next to the maximum voltage drop over the shunt a second restriction to the maximum value of the shunt arises. According to Figure 4.4 the serial combination of internal resistor, shunt resistor and piezo capacitance introduces a pole in the transfer function from the amplifier output voltage U_I towards the voltage applied to the piezo U_{PZ} and the elongation x. This pole results in a phase lag between applied voltage and elongation (shown in Figure 3.5). When the piezo is used in closed-loop this phase lag reduces the phase margin. The influence of the pole on the stability margin of the piezo embedded in the closed-loop of an AFM is discussed in [30]. To ensure high stability margins the pole must be a factor of 10 higher than the bandwidth of the actuator. In [29] the required position sensor bandwidth is discussed for vertical actuators in AFM. With a triangular scanning motion and ten features per line the position sensor bandwidth has to be typically 20 times the line-scan rate for smooth samples and 200 times the line-scan rate for sharp samples, which results in a required position sensor bandwidth of 2 kHz for charge monitoring, which is below the upper boundary of charge monitoring. Therefore, the frequency of the pole introduced by the output resistance of the amplifier and the shunt resistor in combination with the capacitance of the piezo has to be higher than $f_p = 20000\ Hz$. The output resistance of the custom made high voltage amplifier (Tech-Project, Vienna, Austria) was determined to be $R_{OUT} = 7\ \Omega$. With Equation (3.10) the maximum value of the shunt resistor is derived as:

$$\begin{aligned} R_{SHMAX} &= \frac{1}{2\pi f_p C_{PZ}} - R_{OUT} \\ &= \frac{1}{2 \cdot \pi \cdot 20000\ Hz \cdot 0.89 \cdot 10^{-6}\ F} - 7\ \Omega = 1.94\ \Omega. \end{aligned} \tag{4.25}$$

Practically a shunt resistor R_{SH} of 1.9 Ω is chosen. The voltage drop over the shunt resistor is derived as:

$$U_{SH} = Q_{PZ} s R_S. \tag{4.26}$$

The voltage drop over the shunt resistor is acquired with an instrumentation amplifier (INA128). The analog integrator is implemented by an inverting integrator with the resistors R_1, R_2 and C_2. Disregarding the resistor R_2 in a first approach, the transfer function from U_{SH} towards U_{OUT} is derived as

$$\frac{U_{OUT}}{U_{SH}} = \frac{1}{R_1 s C_2} G_{INA2}, \tag{4.27}$$

with the gain of the instrumentation amplifier G_{INA2}. From Equation (2.1) the relation between charge of the piezo and its elongation below the resonance frequency is derived as:

$$Q_{PZ} = \frac{x}{d} C_{PZ}. \tag{4.28}$$

With Equation (4.26 to 4.28) the sensitivity between the output of charge monitoring U_{OUT} and the elongation x is derived as:

$$\frac{U_{OUT}}{x} = \frac{C_{PZ} R_{SH} G_{INA2}}{R_1 C_2 d}. \tag{4.29}$$

With $R_1 = 150\Omega$, $C_2 = 9.4\mu F$ the gain of the instrumentation amplifier is used to reach the required sensitivity of $S = \frac{U_{OUT}}{x} = 0.52\frac{V}{\mu m}$. The theoretical gain is derived as

$$G_{INA2} = S\frac{R_1 C_2 d}{C_{PZ} R_{SH}} = 0.52\frac{V}{\mu m}\frac{150\Omega \cdot 9.4\mu F \cdot 8.2 \cdot 10^{-2}\frac{\mu m}{V}}{0.89\mu F \cdot 1.9\Omega} = 35.6 \tag{4.30}$$

Practically the required sensitivity was reached with a gain of 26.7 ($R_g = 1900\Omega$). The boundaries of the operating frequency range are the same as for charge monitoring via capacitor insertion.

4.2.3 Experimental setup of strain gage measurement

For the experimental setup a current driven Wheatstone bridge is used to measure the deviation of the strain gage resistance from their nominal value ($R_0 = 1k\Omega$), shown in Figure 3.7. The required sensitivity ($0.52\ \frac{V}{\mu m}$) for the strain measurement with strain gages is the same as used for charge monitoring. In Equation (3.16) the output voltage at the wheatstone bridge is given as

$$U_d = I_0 \Delta R. \tag{4.31}$$

The change in resistance with elongation is derived from Equation (3.14) as

$$\frac{\Delta R}{R_0} = K\frac{\Delta l}{l}. \tag{4.32}$$

After substitution of Equation (4.32) into Equation (4.31) the sensitivity of the bridge output voltage to elongation is derived as

$$\begin{aligned} \frac{U_d}{\Delta l} = \frac{I_0 R_0 K}{l} &= \frac{10mA \cdot 1k\Omega \cdot 2}{26 \cdot 10^{-3}m} \\ &= 7.7 \cdot 10^{-4}\frac{V}{\mu m} \end{aligned} \tag{4.33}$$

with the excitation current $I_0 = 10\ mA$, a typical gage factor of $K = 2$ and the length of the piezo $l = 26\ mm$.

To reach the required sensitivity at the output a gain of 675 is needed. Due to its high input resistance, low noise and high common mode rejection ratio an instrumentation amplifier INA111 from Texas Instruments (Dallas, United States) is used to amplify the bridge output voltage as shown in Figure 4.5. As such a high gain would reduce the low frequency performance of the instrumentation amplifier a second stage amplifier is introduced. Practically, a gain $G_{INA3} = 23.7$ ($R_g = 2.2\ k\Omega$) of the instrumentation amplifier and a gain of $G_4 = 21$ of the noninverting amplifier ($R_5 = 20k\Omega$, $R_6 = 1k\Omega$) were used to reach the sensitivity.

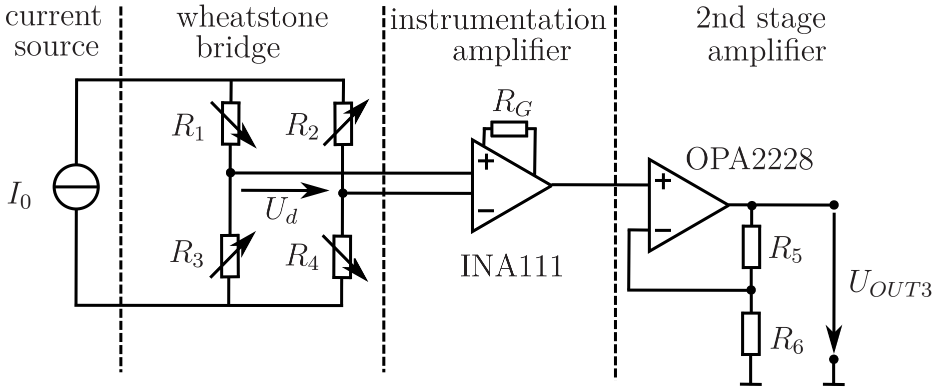

Figure 4.5: Strain gages glued onto the piezo are used to measure the elongation of the piezo. A wheatstone bridge circuit is used to read out the small variation in resistance of the four active strain gages. The bridge voltage is acquired with an instrumentation amplifier in order to measure the differential output signal, without influence of the common mode signal. A non inverting amplifier is used to increase the sensitivity of the measurement.

4.3 Random error of the sensor principles

Based on the derived setups the expected NSD of the sensor principles are calculated. The main contributors to the overall noise of the investigated sensor principle are determined to assess the required quality and magnitude of the used components upfront. Finally, the modeled noise is compared with the measured NSD. The following NSDs are acquired with a HP3563A Dynamic Network Analyzer (Agilent Technologies, Inc., Santa Clara, United States) utilizing a hanning window and three averages, to measure the relevant decades one after another. Although the individual decades are measured immediately after another, small artifacts arise between those decades. Next to the thermal noise of resistors, also the internal noise of the used electronic amplifiers is of interest. The noise specifications given in datasheets are referred to the input of the

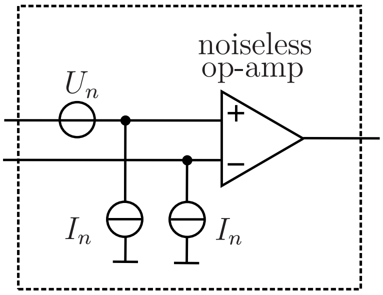

Figure 4.6: The noise model of an op-amp is shown. The equivalent noise model of an op-amp consists of a noiseless op-amp with a voltage source U_n at the non-inverting input representing the voltage noise of the op-amp. The current noise is represented by a current source between ground and each input. The figure is redrawn from [87].

amplifier [87]. The noise model of an op-amp is depicted in Figure 4.6, consisting of a noiseless op-amp with a voltage source at the non-inverting input, representing the voltage noise of the amplifier. The current noise is modeled by current sources between ground and each input of the amplifier.

A typical op-amp consists of three stages. The first stage has a differential input and a differential output with high common mode rejection. The second stage offers a high voltage gain towards its single ended output, followed by an unity gain output stage. The characteristic of the op-amp is heavily influenced by the structure of the input stage, which nearly always consists of a two amplifiers building a long-tailed-pair input stage in order to reach a high common mode rejection ratio [88]. When choosing an electronic amplifier, the used amplifier technology is of high interest as it influences the voltage noise, current noise, offset voltage and bias current. In general, bipolar transistors offer low voltage offset and voltage noise while field-effect transistors are beneficial concerning bias current and current noise. The higher the source impedance, the more important are low current noise and bias current, for example in the case of charge monitoring via capacitor insertion [89]. In general 1/f-noise of active components shows a Power Spectral Density (PSD) that follows $\frac{1}{f^{\alpha}}$, with the frequency exponent α between 0.5 and 2 [90]. Although there is no universal model for 1/f-noise, it is characterized under very specific circumstances [90]. The noise index depends on temperature [91] and gate bias [92]. For the used amplifiers in the introduced setup a noise exponent α of 1.6 proved to be a good assumption to assess the resulting noise upfront [93]. The relevant noise properties of the used electronic amplifiers are given in Table 4.1.

Table 4.1: Characteristic noise values of the used electronic amplifiers given in the respective datasheets.

INA111 (in-amp), $Gain = 23.7$

broadband voltage noise	$10 \frac{nV}{\sqrt{Hz}}$	broadband current noise	$0.8 \frac{fA}{\sqrt{Hz}}$
1/f-corner frequency	$10\ Hz$	1/f-corner frequency	$1\ kHz$

INA111 (in-amp), $Gain = 3.7$ and $Gain = 1.3$

broadband voltage noise	$50 \frac{nV}{\sqrt{Hz}}$	broadband current noise	$4 \frac{fA}{\sqrt{Hz}}$
1/f-corner frequency	$10\ Hz$	1/f-corner frequency	$1\ kHz$

INA128 (in-amp), $Gain = 27.3$

broadband voltage noise	$8 \frac{nV}{\sqrt{Hz}}$	broadband current noise	$100 \frac{fA}{\sqrt{Hz}}$
1/f-corner frequency	$1\ Hz$	1/f-corner frequency	$1\ kHz$

OPA2228 (op-amp)

broadband voltage noise	$3 \frac{nV}{\sqrt{Hz}}$	broadband current noise	$0.4 \frac{pA}{\sqrt{Hz}}$
1/f-corner frequency	$10\ Hz$	1/f-corner frequency	$1\ kHz$

AD712 (op-amp)

broadband voltage noise	$18 \frac{nV}{\sqrt{Hz}}$	broadband current noise	$10 \frac{fA}{\sqrt{Hz}}$
1/f-corner frequency	$10\ Hz$	1/f-corner frequency	$1\ kHz$

4.3.1 Random error of charge monitoring with capacitor insertion applied to stacked piezo

The equivalent circuit for the NSD of charge monitoring via capacitor insertion is derived from Figure 4.3. The piezo amplifier is replaced by a short circuit, because the output resistance is neglitible compared to the impedance of the piezo. Thus, the piezo and the sensing capacitor are in parallel. The parallel alignment of both capacitors is represented by the equivalent capacitance C_{eq1} derived as: $C_{eq1} = C_{PZ} + C_S = 0.89\ \mu F + 100\ \mu F = 100.89 \mu F$. The parasitic resistances R_S and R_{PZ} as well as the external resistance R_{SC} are also in parallel, represented by the equivalent resistance $R_{eq1} = R_{PZ} \parallel R_S \parallel R_{SC} = 3.0\ G\Omega \parallel 8.4\ G\Omega \parallel 27\ M\Omega = 26.7\ M\Omega$.

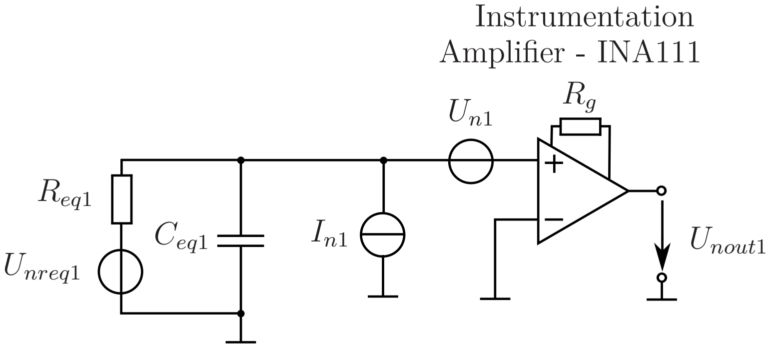

Figure 4.7: The equivalent circuit of capacitive charge monitoring is depicted. It consists of the equivalent resistance R_{eq1} representing the parallel connection of R_{PZ}, R_{SC} and R_S. The equivalent capacitance C_{eq1} is the sum of the piezo capacitance C_{pz} and the sensing capacitance C_S. U_{nreq1} represents the thermal noise of R_{eq1}. U_{n1} and I_{n1} are the input voltage and current noise of the in-amp. The contribution of each noise source to the output noise U_{nout1} is investigated.

Figure 4.7 shows the noise equivalent circuit, consisting of U_{n1} and I_{n1} the voltage and current noise of the instrumentation amplifier. U_{nreq1} is the thermal noise of the resistance R_{eq1} derived with Equation (4.14). Although, the equivalent resistor R_{eq1} has a resistance of 27 $M\Omega$ it does not contribute to the noise at the output U_{nout}. Because the resistance R_{eq1} and C_{eq1} build a low-pass filter from U_{nreq1} towards the output U_{nout}. The measurement is done on a high impedance node. Therefore, the input offset and bias current play an important role, as they result in remarkable voltages in combination with high impedances. Thus their contribution to low frequency noise was measured with a capacitive load at the input resulting in a current noise of 100 $\frac{fA}{\sqrt{Hz}}$, a corner frequency of 1 kHz and a slope of -0.8 in the 1/f-noise. The transfer function of the current noise I_{n1} towards the output U_{nout1} is derived as:

$$\begin{aligned}\left|\frac{U_{nout1}}{I_{n1}}\right| &= G_{INA1}\frac{R_{eq1}}{\sqrt{1+(2\pi f C_{eq1}R_{eq1})^2}}\\ &= 3.7\frac{26.7\ M\Omega}{\sqrt{1+(2\pi f\cdot 100.89\ \mu F\cdot 26.7\ M\Omega)^2}}\\ &= \frac{125.5\cdot 10^6}{\sqrt{1+(f\cdot 16925)^2}}\Omega\end{aligned} \tag{4.34}$$

With the transfer function of the current noise toward the output given in Equation (4.34), the contribution of the current noise to the noise at the output shows a slope of -1.8, depicted in Figure 4.8 by the green line. The voltage noise of U_{n1} is amplified by the gain G_{INA1} of the instrumentation amplifier:

$$\left|\frac{U_{nout}}{U_{n1}}\right| = G_{INA1} = 3.7. \tag{4.35}$$

The contribution of the voltage noise to the noise at the output is shown with magenta crosses in Figure 4.8. According to Equation (4.20) the contribution of the noise spectral density of the current noise and voltage noise (with the noise parameters given in Table 4.1) are summed up quadratically and are depicted by the blue line.

The resulting noise at the output consists of three parts: Above 10 Hz the white component of the voltage noise determines the NSD. Between 100 mHz and 10 Hz the 1/f-component of the voltage noise dominates, so that the NSD falls with a slope of -0.8. Below 100 mHz the integrated 1/f-current noise results in a slope of -1.8.

The modeled NSD from Figure 4.8 and the measured NSD coincides above 100 mHz. Around 10 mHz the measured NSD exceeds the modelled NSD. This difference is an measurement artifact, as the measurement takes several hours.

A reduction of the low frequency noise by including resistors in parallel to the piezo and the sensing capacitor is discussed in Section 3.3.1. Nevertheless, this approach would rise the low frequency boundary of charge monitoring and is therefore not applicable. Increasing the sensing capacitance would reduce the noise as well as the signal of interest. As the sensitivity of the sensor would be decreased proportionally there is no improvement of SNR. The circuit from Figure 3.3 was implemented on a breadboard. The circuit is influenced by the power line and environmental influence. Circuits with high impedance nodes are very sensitive to electromagnetic interference [30]. The standard deviation is derived from the square-root of the integration over the squared NSD. The standard deviation of charge monitoring via capacitor insertion between 1 mHz and 2 kHz is derived as 2.24 nm. It is remarkable that due to the strong increase of the NSD at lower frequencies nearly 90 % of the noise is located in the lowest decade. When rising the lower boundary to 10 mHz the standard deviation is reduced to 0.27 nm.

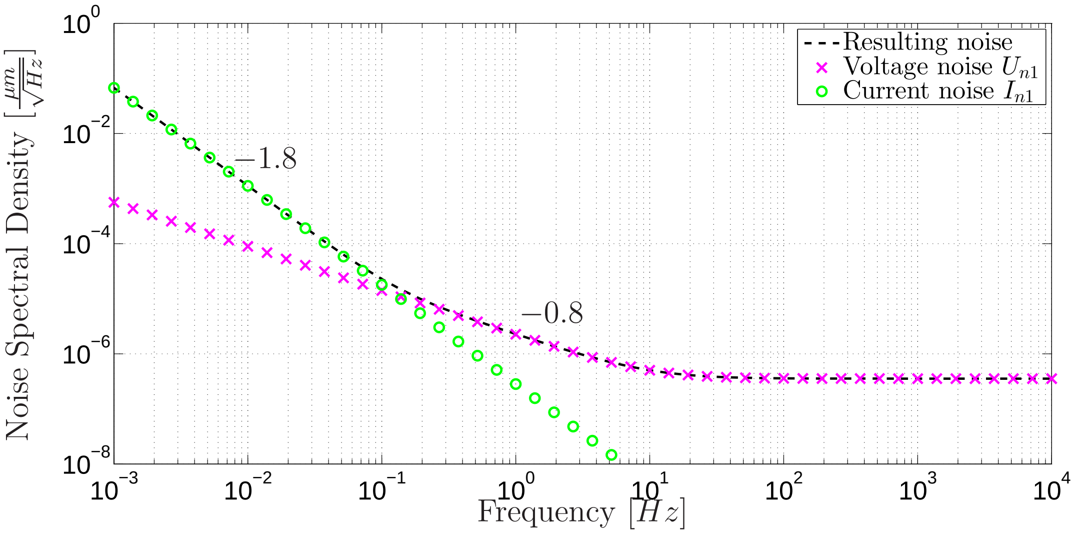

Figure 4.8: The expected noise spectral density of charge monitoring via capacitor insertion is shown. According to the derived noise model, the contribution of the current noise (green circles) and voltage noise (magenta crosses) of the instrumentation amplifier to the resulting noise (black dashed) at the output is shown. The current noise decreases with a slope of -0.8 below the 1/f-corner frequency of 1 kHz. The current noise is integrated by the capacitance C_{eq}, which results in a voltage noise at the output, that decreases with a slope of -1.8. Below 100 mHz the integrated current noise dominates the resulting noise and above the voltage noise of the instrumentation amplifier dominates. The voltage noise of the in-amp dominates the noise at the output above 100 mHz and decreases below 10 Hz with a slope of -0.8.

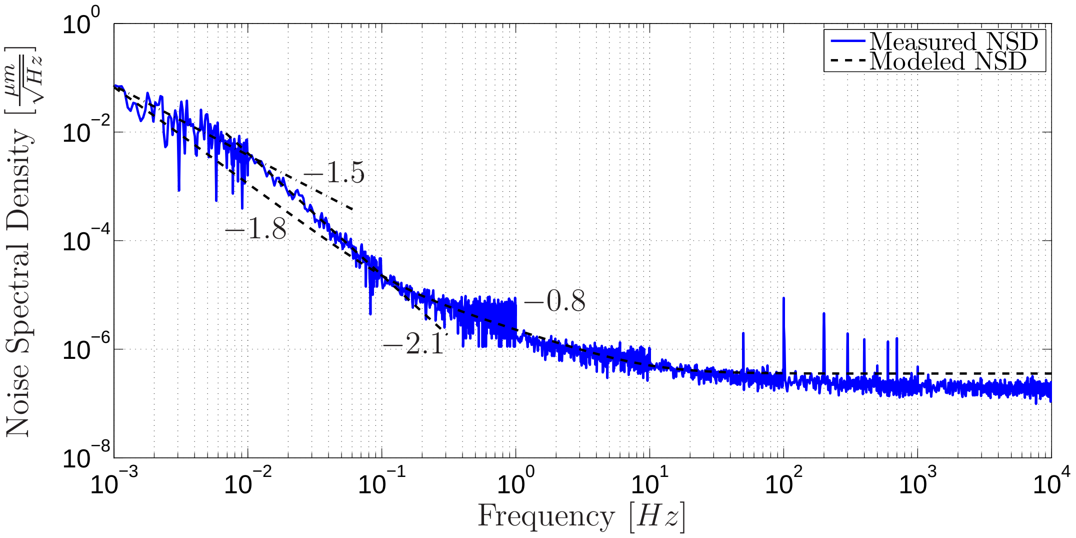

Figure 4.9: The measured NSD of charge monitoring via capacitor insertion is shown by the blue line. The measurement is compared with the expected NSD derived from the noise model and shown by the black dashed line. Around 10 mHz the measured NSD is higher than the expected NSD. The slope of the measured NSD (depicted by the dashed dot line) between 1 mHz and 10 mHz is -1.5 and between 10 mHz and 100 mHz -2.1, in comparison an expected slope of -1.8 is deduced from the noise model. Due to the interference with the power line, peaks arise in the NSD at 50 Hz and its harmonic. As the NSD is measured decade per decade a measurement artifact arises at 1 Hz. Although the measurements are done immediately after each other, this artifact could not be avoided.

4.3.2 Random error of charge monitoring via current integration applied to stacked piezo

The noise model for charge monitoring via current integration is derived from Figure 4.4. To acquire the NSD the resistance R_2 is chosen sufficiently high in order not to influence the measurement.

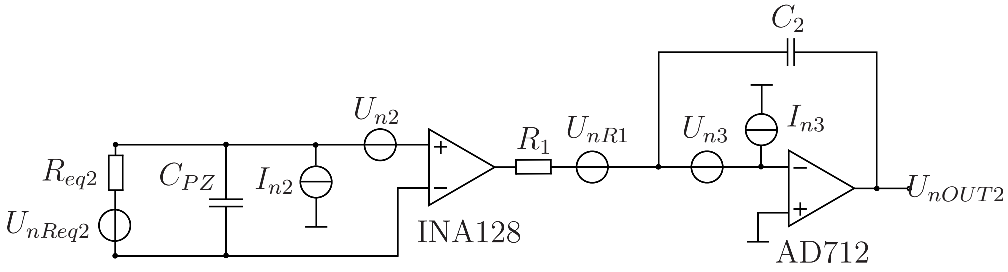

Figure 4.10: The equivalent noise circuit for charge monitoring via current integration is shown. The equivalent resistance R_{eq2} consists of the parallel alignment of the shunt resistor R_{SH} and the parasitic resistance of the piezo R_{PZ}. The current noise I_{n2} and the voltage noise U_{n2} represents the internal noise of the instrumentation amplifier INA128. The thermal noise U_{nR1} arises from the resistor R_1. The noise introduced by the op-amp AD712 is represented by U_{n3} and I_{n3}.

The piezo amplifier is replaced by a short circuit. Thereby the shunt resistor R_{SH} is in parallel to the piezo. The equivalent resistance R_{eq2} represents the shunt resistor R_{SH} in parallel to the parasitic resistance of the piezo R_{PZ}, resulting in a resistance which is equal to the shunt resistance $R_{eq2} = R_{SH} \parallel R_{PZ} = 1.9\Omega \parallel 3.0G\Omega = 1.9\Omega$. Compared to the input voltage noise of the INA128 given in Table 4.1 the noise arising from the equivalent resistor U_{nReq2} is negligible. The input current noise of the INA128 I_{n2} results in a voltage noise with the equivalent resistor in parallel to the capacitance C_{PZ}. Due to the low shunt resistor the input current noise can be neglected, compared to its voltage noise. The voltage noise U_{n2} is amplified by the instrumentation amplifier gain and integrated towards the output U_{nOUT2}. The thermal noise U_{nR1} of the resistance R_1 is also integrated towards the output, but compared to the amplified voltage noise of the instrumentation amplifier it is negligible. The current noise I_{n3} of the AD712 is integrated via the capacitor C_2 towards the output. Due to a low current noise and high capacitance the current noise is irrelevant as well. Finally, the voltage noise of the instrumentation amplifier U_{n2} and operation amplifier U_{n3} determine the random error at the output. The noise of the instrumentation amplifier is amplified by the instrumentation amplifier gain G_{INA2} and is integrated

$$\left|\frac{U_{OUT}}{U_{n2}}\right| = G_{INA2}\frac{1}{2\pi f R_1 C_2} = 27.3\frac{1}{2\pi f \cdot 150\Omega \cdot 9.4\mu F} = \frac{3082\ Hz}{f}. \tag{4.36}$$

The impact of the voltage noise U_{n3} towards the output U_{OUT} is dertemined as:

$$\begin{aligned}\left|\frac{U_{OUT}}{U_{n3}}\right| &= \left|\frac{1+sC_2R_1}{sC_2R_1}\right| \\ &= \frac{\sqrt{1+(2\pi f\cdot 9.4\mu F\cdot 150\Omega)^2}}{2\pi f\cdot 9.4\mu F\cdot 150\Omega} \\ &= \frac{\sqrt{1+(0.0089\cdot f)^2}}{0.0089\cdot f}.\end{aligned} \tag{4.37}$$

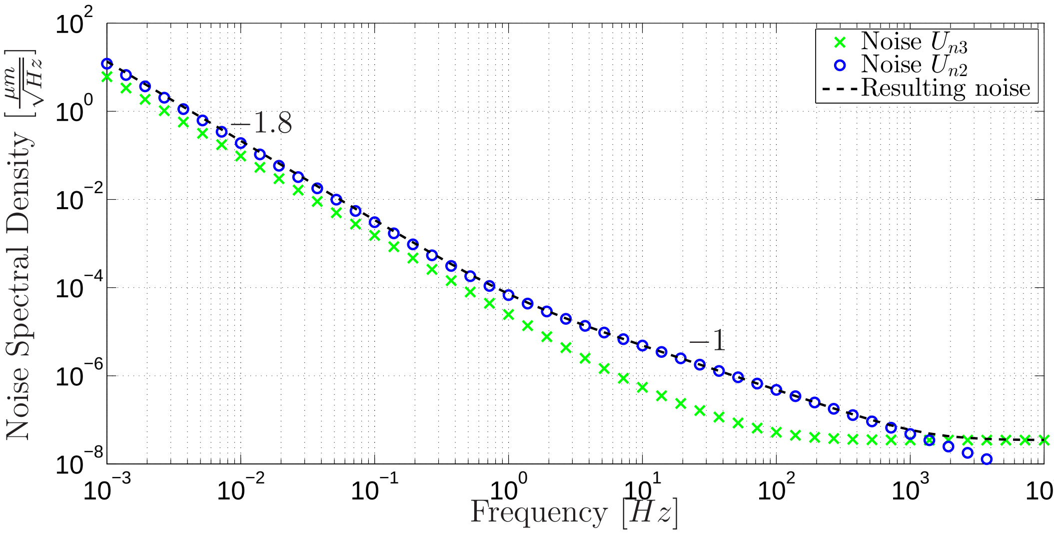

Figure 4.11: The modeled noise spectral density of charge monitoring via current integration is shown by the black dashed line. It is composed of the contribution from the voltage noise of the instrumentation amplifier depicted by blue circles and the voltage noise of the op-amp shown by green crosses. Both voltage noises show an increasing voltage noise below the 1/f-corner frequency of 1 Hz. The component arising from the instrumentation amplifier is integrated over the whole measurement range. Above 3 kHz the resulting noise is determined by the voltage noise of the op-amp (U_{n3}), below 3 kHz the voltage noise of the in-amp (U_{n2}) determines the resulting noise.

According to Equation (4.36) the modeled voltage noise of the in-amp is shaped by the integrator. Therefore the contribution of U_{n2} to the NSD at the output shows a slope of -1 above 1 Hz, as shown in Figure 4.11 (blue circles). Below the 1/f-corner frequency of 1 Hz the voltage noise of the in-amp is dominated by the 1/f-component which falls with a slope of -0.8. The resulting contribution to the noise at the output decreases with a slope of -1.8 in this frequency range. The noise of the op-amp (U_{n3}) shows a 1/f-corner frequency of 10 Hz. With the transfer function given in Equation (4.37) the contribution to the noise at the output is white above 112 Hz and decreases with a slope of -1.8 below 10 Hz. The noise arising from U_{n2} and U_{n3} are summed up quadratically to the NSD at the output. The resulting noise from the model is depicted by the black, dashed line in Figure 4.11. Above 3 kHz the noise at the output is dominated by the voltage noise of the op-amp and below by the voltage noise of the in-amp.

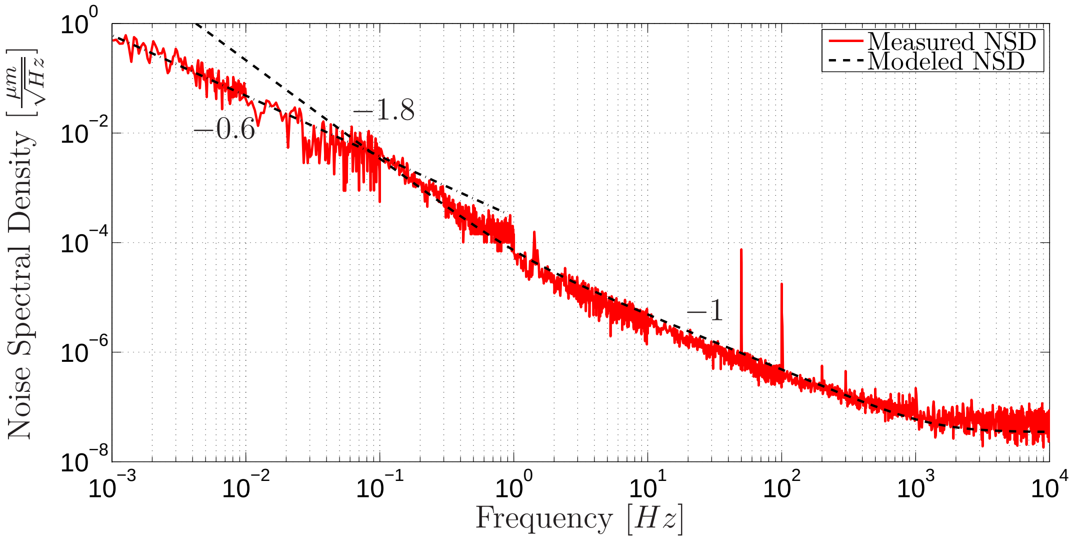

Figure 4.12: The measured noise at the output of charge monitoring is shown by the red line. In comparison the expected NSD derived from the noise model is depicted by the black dashed line. Below 50 mHz the measured NSD deviates from the modeled NSD, because of measurement artefacts. The slope of the measured NSD is -0.6 in this frequency range depicted by the dashed-dot line. Due to the interference with the power line, peaks arise in the NSD at 50 Hz and its harmonic.

The measured NSD of charge monitoring is depicted in Figure 4.12 by the red line. The expected NSD derived from the noise model is shown by the black dashed line and matches with the measurement down to a frequency of 100 mHz. Below 0.1 Hz the measured NSD shows a reduced slope, which is expected to arise from changing ambient conditions as the measurement lasts several hours. The standard deviation of the charge monitoring via current integration is 23.4 nm between 1 mHz and 2 kHz. The NSD of charge monitoring via current integration and capacitor insertion is shown in Figure 4.13. Above 200 Hz the NSD of current integration is below the NSD of capacitor insertion. Due to the significant lower noise below 200 Hz charge monitoring via capacitor insertion is preferred compared to charge monitoring via current integration.

The NSD at the output could be theoretically reduced by using amplifiers with lower noise or by reducing the noise transfer function of the dominating noise sources given in Equation (4.36) and (4.37). Practically, the gain in Equation (4.36) cannot be reduced as otherwise the required sensitivity can not be reached. Due to the structure of the transfer function given in Equation (4.37), the noise gain can not be reduced in the relevant frequency range as well. Regarding circuit design, a high capacitance

C_2 is beneficial so that the current noise of the op-amp (I_{n3}) has no influence. The main part of the noise arises from the voltage noise of the in-amp (U_{n2}). In difference to charge monitoring via capacitor insertion the in-amp INA128 is preferred, as the higher current noise has no influence, but the lower voltage noise is beneficial.

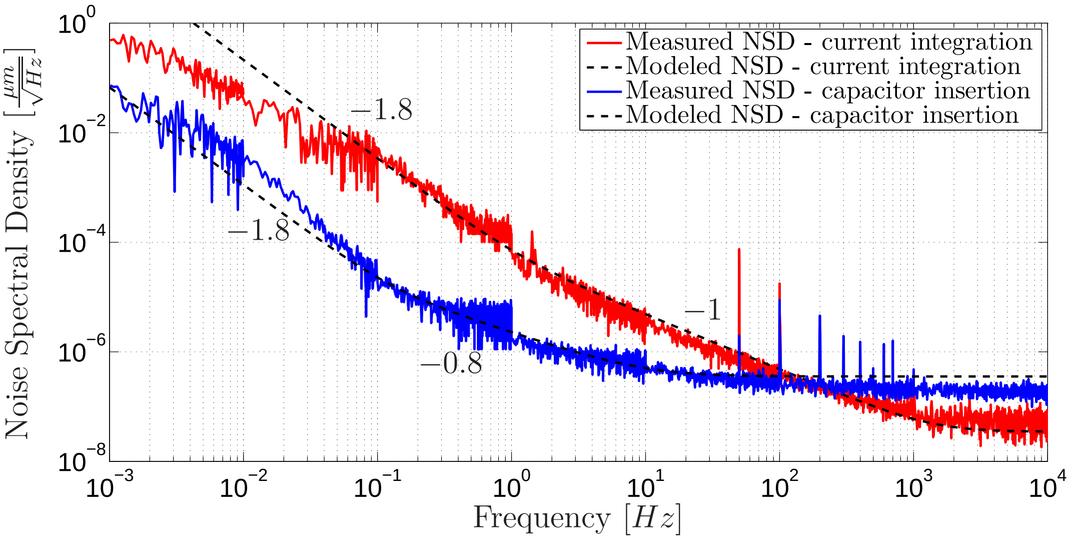

Figure 4.13: The measured NSD of charge monitoring is shown in red and the NSD of charge monitoring via capacitor insertion is depicted by the blue line. Below 200 Hz the NSD of charge monitoring via capacitor insertion is below the NSD of charge monitoring via current integration.

4.3.3 Random error of strain measurement with strain gages

The equivalent noise model of strain measurement with strain gages is derived from Figure 4.5. With the already introduced noise model of electronic amplifiers (given in Figure 4.6) the equivalent noise model for strain measurement with strain gages is derived in Figure 4.14.

The equivalent noise model of the four strain gages aligned in a wheatstone bridge, driven by a current source, is represented by a single resistance R_0 and its thermal noise U_{nR0}, derived from Equation (4.14). The voltage and current noise of the in-amp (INA111) are represented by the voltage and current source U_{n4} and I_{n4}, respectively. The current noise I_{n4} is transformed to a voltage noise by multiplication with R_0. With the given noise values from Table 4.1 and the $R_0 = 1\ k\Omega$ it is concluded, that the current noise of the instrumentation amplifier can be neglected, compared to its voltage noise. The noise arising from the wheatstone bridge U_{nR0} and the voltage noises of the instrumentation amplifier U_{n4} are amplified by the gain of the in-amp and the gain of the 2nd stage amplifier towards the output U_{nOUT3}, given as

$$\left|\frac{U_{nOUT3}}{U_{nR0}}\right| = \left|\frac{U_{nOUT3}}{U_{n4}}\right| = G_{INA3} \cdot (1 + \frac{R_5}{R_6}) = 23.7 \cdot (1 + \frac{20\ k\Omega}{1\ k\Omega}) = 498. \tag{4.38}$$

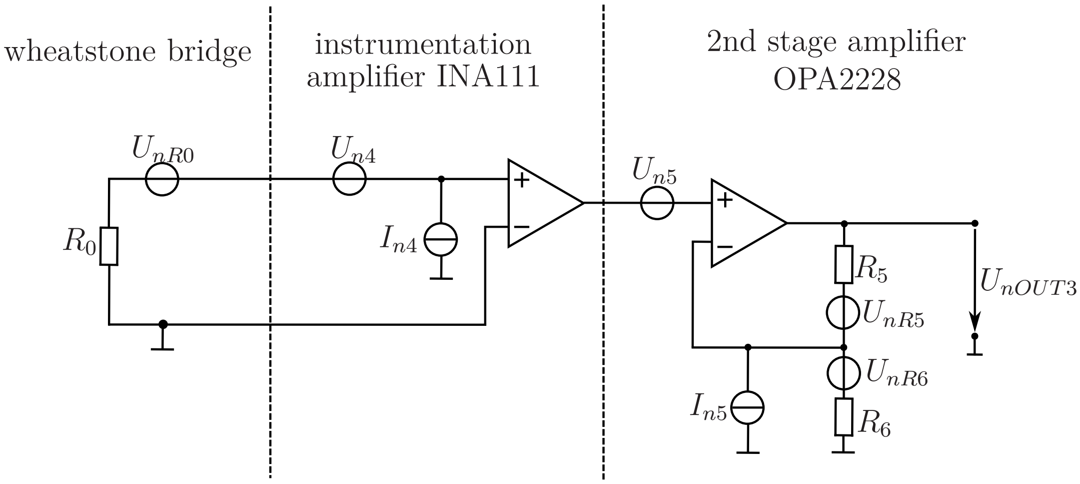

Figure 4.14: The noise model of the circuit for strain measurement with strain gages is shown. The equivalent noise model of the wheatstone bridge and the current source is indicated with R_0 and its thermal noise is U_{nR0}. The voltage noise of the instrumentation and operation amplifier is U_{n4} and U_{n5} respectively. Their current sources are named I_{n4} and I_{n5}. The resistors R_5 and R_6, needed for the noninverting amplifier, introduce the thermal noise U_{nR5} and U_{nR6}. The contribution of the introduced noise sources on the output noise U_{nOUT3} is investigated.

The input noise of the op-amp U_{n5} is amplified by the 2nd stage amplifier. The current noise of the op-amp I_{n5} results in a voltage noise of $I_{n5}R_5$ at U_{nOUT3}. The thermal noise U_{nR5} influences directly the output noise U_{nOUT3}. The thermal noise U_{nR6} is amplified with the gain $\frac{R_5}{R_6}$ towards the output U_{nOUT3}. The noise contribution of the 2nd stage amplifier (U_{n5}, I_{n5}, U_{nR5}, U_{nR6}) is negligible compared to the voltage noise of the in-amp U_{n4} and the thermal noise of the strain gages U_{nR0}, which are amplified by both amplifiers.

The contribution of the thermal noise of the strain gages and the voltage noise of the in-amp is shown in Figure 4.15. The thermal noise, amplified by the transfer function given in Equation (4.38) is shown by blue circles. The voltage noise of the in-amp (with the noise parameters from Table 4.1) is amplified by the same gain and represented with black crosses. The resulting noise (shown in green) is mainly determined by the noise of the in-amp. The expected noise at the output corresponds with the measured noise from Figure 4.16. Below the 1/f-corner frequency the 1/f-component of the voltage noise U_{n4} dominates the NSD. The standard deviation obtained from the measured NSD between 1 mHz and 2 kHz is 2.5 nm. From a circuit engineering point of view, the NSD of the strain gage measurement can not be reduced, as the relevant transfer function determines the required sensitivity as well. Figure 4.16 shows the resulting noise spectral density.

,

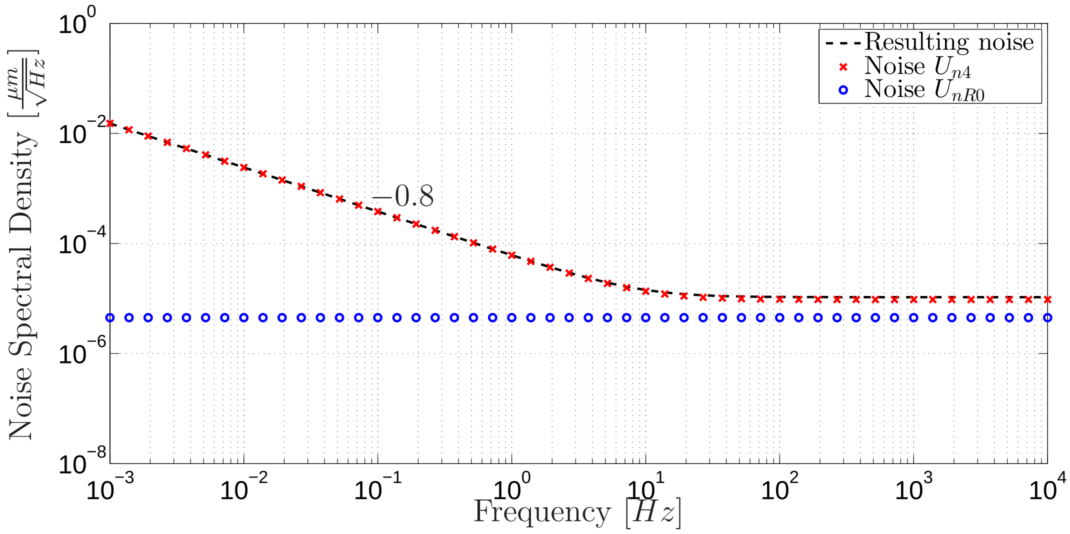

Figure 4.15: The expected noise spectral density of the strain gage measurement is depicted. The contribution of the in-amp voltage noise U_{n4} indicated by red crosses and the thermal noise of the strain gages U_{nR0} indicated by blue circles are the relevant noise sources for the resulting NSD depicted by the black dashed line. The 1/f-noise of the instrumentation decreases with a slope of -0.8 below 10 Hz.

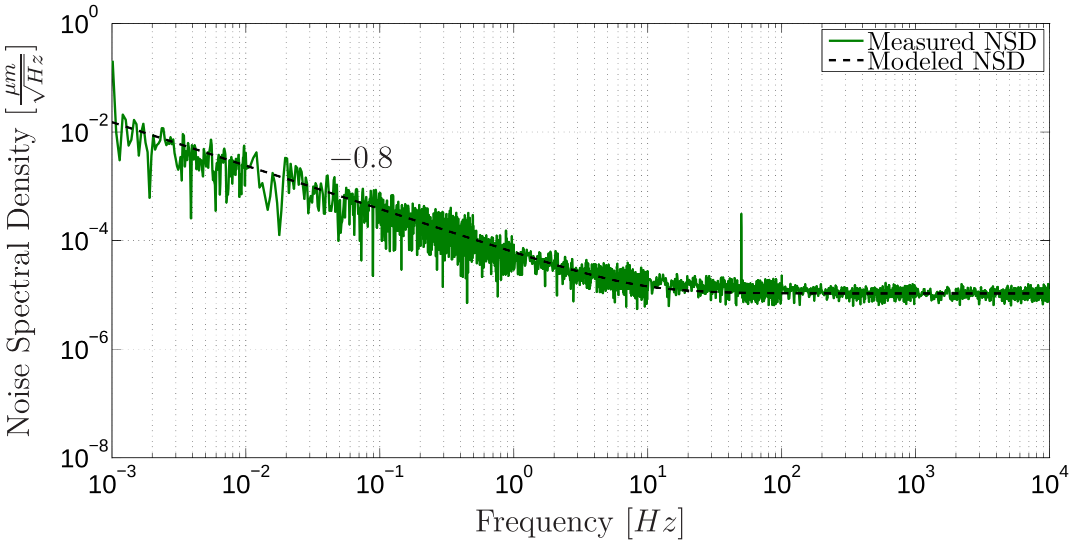

Figure 4.16: The measured noise spectral density of the strain gage measurement is shown. Due to the high amplification of the instrumentation amplifier the random error is determined by the noise of the in-amp. Below 10 Hz the 1/f-noise of the instrumentation amplifier dominates the random error, resulting in an decrease with a slope of -0.8. At 50 Hz a peak is appearant in the noise spectral density due to interference of the power line.

4.4 Random error of charge monitoring via capacitor insertion applied to the tube piezo

In comparison to the stacked piezo, the tube piezo is not equipped with strain gages. Due to the beneficial NSD of charge monitoring via capacitor insertion, for the tube piezo only this approach of doing charge monitoring is implemented. The Z-piezo of the E-scanner has a capacitance of $C_{PZ} = 28\ nF$ and a time constant of $\tau = 470\ s$. Therefore, the circuit depicted in Figure 3.3 has to be adapted. A polypropylene sensing capacitor with $C_S = 9.4\ \mu F$ is used. To match the time constants of the sensing path to the piezo a resistance $R_{SC} = 50\ M\Omega$ is introduced in parallel to the sensing capacitor as depicted in Figure 3.3. The resulting crossover frequency between voltage and charge sensing is $f_c = \frac{1}{2\pi R_{SC} C_S} = 0.34\ mHz$. The same sensitivity of $0.52\ \frac{V}{\mu m}$ as in Section 3.3.1 is achieved with a gain $G_{INA4} = 1.3$ ($R_g = 160\ k\Omega$). The expected noise is derived from the same noise model as used for charge monitoring applied to the stacked piezo derived in Chapter 4.

The transfer function of the current noise I_{n1} towards the output U_{nout1} is derived as:

$$\begin{aligned}\left|\frac{U_{nout1}}{I_{n1}}\right| &= G_{INA1}\frac{R_{eq1}}{\sqrt{1+(2\pi f C_{eq1} R_{eq1})^2}} \\ &= 1.3\frac{65\ M\Omega}{\sqrt{1+(2\pi f \cdot 9.4\ \mu F \cdot 50\ M\Omega)^2}} \\ &= \frac{125.5 \cdot 10^6}{\sqrt{1+(f \cdot 2953)^2}}\Omega\end{aligned} \tag{4.39}$$

With the transfer function of the current noise toward the output given in Equation (4.34), the contribution of the current noise to the noise at the output shows a slope of −1.8, depicted in Figure 4.17 in green. The voltage noise of U_{n1} is amplified by the gain G_{INA4} of the instrumentation amplifier:

$$\left|\frac{U_{nout}}{U_{n1}}\right| = G_{INA4} = 1.3. \tag{4.40}$$

With the characteristical noise parameters of the in-amp INA111 the expected noise is shown in Figure 4.17.

According to the equivalent circuit for noise in charge monitoring as shown in Figure 4.7, the integrated 1/f-current noise results in a strong increase in noise with decreasing frequency below 1 Hz as shown in Figure 4.18. Due to the reduced gain of the instrumentation amplifier, the measured noise is also reduced compared to Figure 4.9.

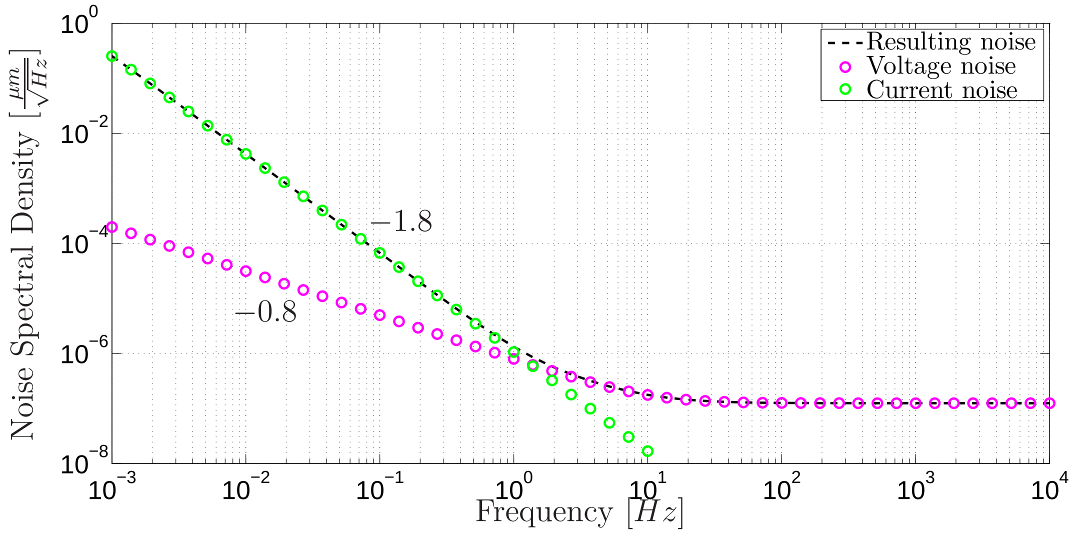

Figure 4.17: The expected noise spectral density of charge monitoring applied to the E-scanner is shown. The current noise is integrated by the capacitance C_{eq} resulting in a voltage noise at the output with a slope of -1.8. Below 1 Hz the integrated current noise dominates the resulting NSD and above the voltage noise of the instrumentation amplifier.

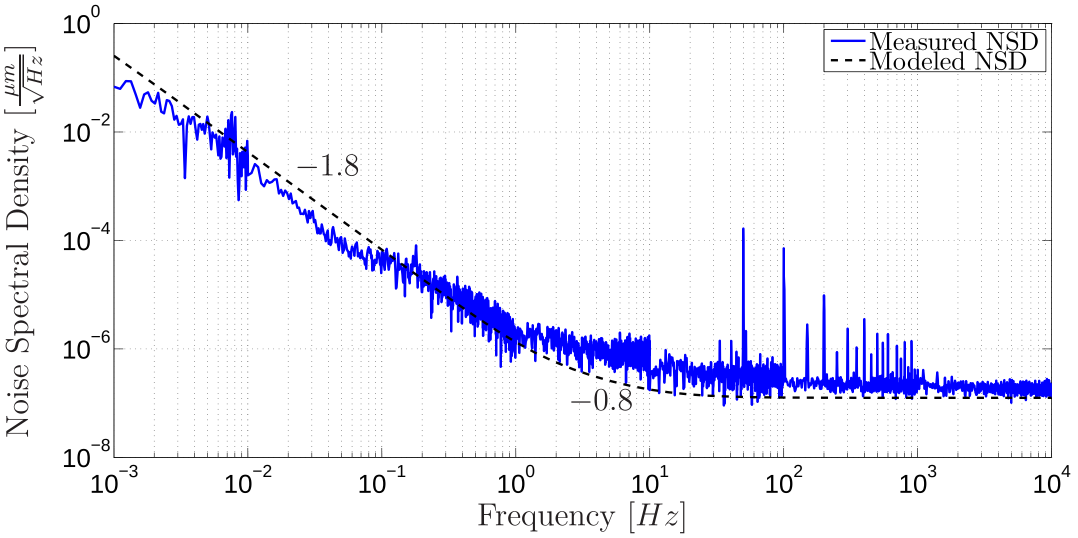

Figure 4.18: The measured NSD of charge monitoring via capacitor insertion applied to the E-scanner is shown. Above 20 Hz the white component of the voltage noise of the instrumentation amplifier determines the resulting noise spectral density. Between 1 Hz and 20 Hz the 1/f-component of the voltage noise results in a slope of -0.8. Due to the interference with the power line at 50 Hz and its harmonics peaks arise in the NSD, compared to charge monitoring applied to the stacked piezo the power line is increased due to a more spacious setup.

4.5 Summary of sensor performance

Charge monitoring via capacitor insertion as well as charge monitoring via current integration offer low noise at higher frequency, while suffering from increased frequency noise. Charge monitoring via current integration requires integrating behaviour. Thereby, as well its NSD is shaped by the integrator. In comparison the increased NSD at low frequency in charge monitoring via capacitor insertion arises from current noise at the high impedance. As the capacitance of the piezo and the sensing capacitor offers moderate impedance at higher frequencies the current noise makes an appearance in the resulting NSD only below 100 mHz. A comparison of the NSD of both charge monitoring approaches is given in Figure 4.13. Because of the beneficial noise, charge monitoring via capacitor insertion is used in the following to do sensor fusion based on random error. Due to the low sensitivity of strain gages high gain is required in the read-out system, which amplifies the noise as well. Nevertheless, strain gages offer high DC stability.

CHAPTER 5

Sensor fusion based on random errors

Charge monitoring shows low noise over a wide frequency range, however the susceptibility to current noise and bias current results in an increased noise at low frequency. In contrast strain gages offer high DC stability, while suffering from significant broadband noise. In this Chapter a method of sensor fusion of charge monitoring and strain gages based on statistical error is shown. This method can be applied when minimization of the noise is desired and results in a sensor system containing the benefits of both initial sensors.

5.1 Complementary filter

The considerations about complementary filtering are based on [73] and [74]. A comparison of complementary and Kalman filtering is given [74].

The schematic of a complementary filter is depicted in Figure 5.1, where x and y are measurements of the same signal z. Assuming that the noise n_1 in x is mainly high frequency and the noise n_2 in y is mainly low-frequency. By implementing $G(s)$ as low-pass filter and its counterpart $1 - G(s)$ as high-pass filter, the error in the estimate $\hat{z}$ is reduced. The crossover frequency needs to be optimized depending on the noise characteristics of the sensor signal. In this project the elongation of the piezo is redundant measured by means of charge monitoring and strain gage measurement. Each provides its own particular error characteristic shown in Chapter 4. After filtering the measurements x and y with $G(s)$ and $1 - G(s)$ the filter outputs are summed up to $\hat{z}$ the estimation of z. The output signal of the complementary filter in the Laplace domain is derived as

$$\hat{Z}(s) = Z(s) + N_1(s)G(s) + N_2(s)(1 - G(s)). \tag{5.1}$$

The transfer function $G(s)$ has no influence on the transmission of the deterministic part $Z(s)$ of the signal through the filter. Therefore $G(s)$ is used to minimize the

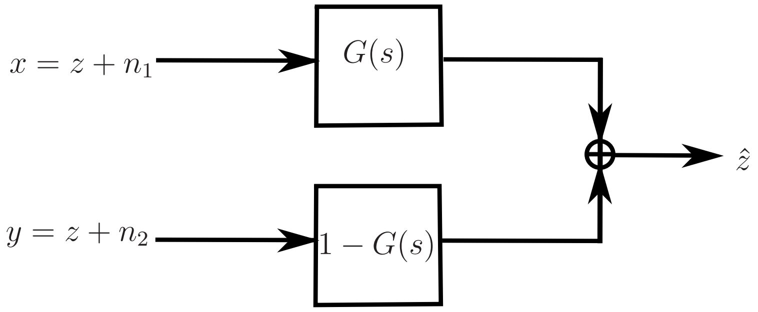

Figure 5.1: The signals x and y are measurements of the same signal z with different sensors. Each measurement has its own noise characteristics n_1 and n_2 respectively, as the measurements arise from different measurement principles. The filters $G(s)$ and $1 - G(s)$ are designed to attenuate the noise in the estimation $\hat{z}$. In order to preserve the deterministic part in the signals the sum of both filters has to be constant over frequency. If $G(s)$ is a low-pass filter, its complementary part $1 - G(s)$ is a high-pass filter [74].

mean-square error in $\hat{Z}(s)$. The simplest implementation of a complementary filter consists of a first-order low pass and a first-order high pass filter. Although higher order complementary filters exist, they are practically only realized digitally [94]. In analog implementations higher-order filters show unavoidable deviation from the nominal filter coefficient, which results in unacceptable phase error. As the use of digital filters is not in the scope of this thesis, in the following only analog first-order complementary filters are considered. To determine the crossover frequency f_{co} of $G(s)$ and $1 - G(s)$ the measured PSD for charge monitoring S_{CHM} and the strain gage measurement S_{SG} are used. With Equation (4.21) the expected power spectral density in the combined signal is derived as

$$S_{\hat{z}}(f, f_{co}) = |G(f, f_{co})|^2 \, S_{SG}(f) + |1 - G(f, f_{co})|^2 \, S_{CHM}(f), \tag{5.2}$$

with $G(f, f_{co})$ a first-order high-pass filter with crossover frequency f_{co}. The expected noise power P at the filter output is derived together with Equation (4.16) to:

$$\begin{aligned} P(f_{co}) &= \int_{f_1}^{f_2} S_{\hat{z}}(f, f_{co}) \, \cdot \mathrm{d}f \\ &= \int_{f_1}^{f_2} |G(f, f_{co})|^2 \, S_{SG}(f) + |1 - G(f, f_{co})|^2 \, S_{CHM}(f) \, \cdot \mathrm{d}f. \end{aligned} \tag{5.3}$$

The noise Power $P(f_{co})$, which is depending on the crossover frequency f_{co} of the high- and low-pass filter, is used as a cost function to minimize the squared error [95], [96].

To determine the filter crossover frequency, which minimizes the cost function, the interior-point method is used. The interior point method uses logarithmic barrier functions to prevent the crossover frequency from exceeding the boundaries [97]. To find the crossover frequency, which minimizes the cost function Matlab function fmincon is used, with parameters ’interior-point’ to choose the underlying algorithm, the cost function given in Equation (5.3), the upper and lower boundary and an initial value.

The lower and upper boundary of the crossover frequency is set to the upper- and lower limit of the noise measurement 1 mHz and 10 kHz, respectively.

5.2 Experimental results

The sensor fusion approach of charge monitoring and strain gages, based on random erros is shown for charge monitoring applied to the stacked piezo as well as the E-scanner. For the stacked piezo the result is verified by the measurement of the NSD at the output of the implemented complementary filter. As the tube piezo is not equipped with strain gages, only the expected crossover frequency of the complementary filter is calculated.

Stacked piezoelectric actuator

In Figure 5.3 the random noise of charge monitoring via capacitor insertion applied to the stacked piezo on the one hand and of the strain gage measurement on the other hand are compared. At higher frequencies the noise of the strain gage measurement is significantly higher than the noise in charge monitoring.

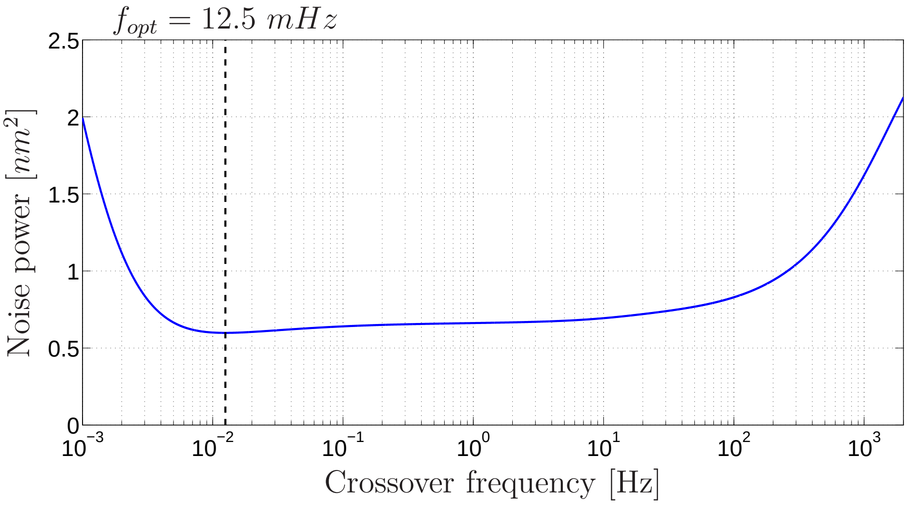

Figure 5.2: The noise power in the combined signal over the crossover frequency is depicted. At 12.5 mHz a minimum arises which determines the optimum crossover frequency of the complementary filter.

The integrated 1/f-current noise results in an increasing noise in charge monitoring at low frequencies. Thereby, the noise of charge monitoring exceeds the noise of the strain gages. With the introduced minimization approach from Section 5.1 the crossover frequency of the first-order complementary filter is determined to be 12.5 mHz. The resulting noise power in the combined signal over the crossover frequency of the complementary filter is depicted in Figure 5.2 and shows a minimum at 12.5 mHz.

The NSD of the complementary filter output is depicted in Figure 5.4. Above the crossover frequency the noise spectral density of the combined signal follows the noise

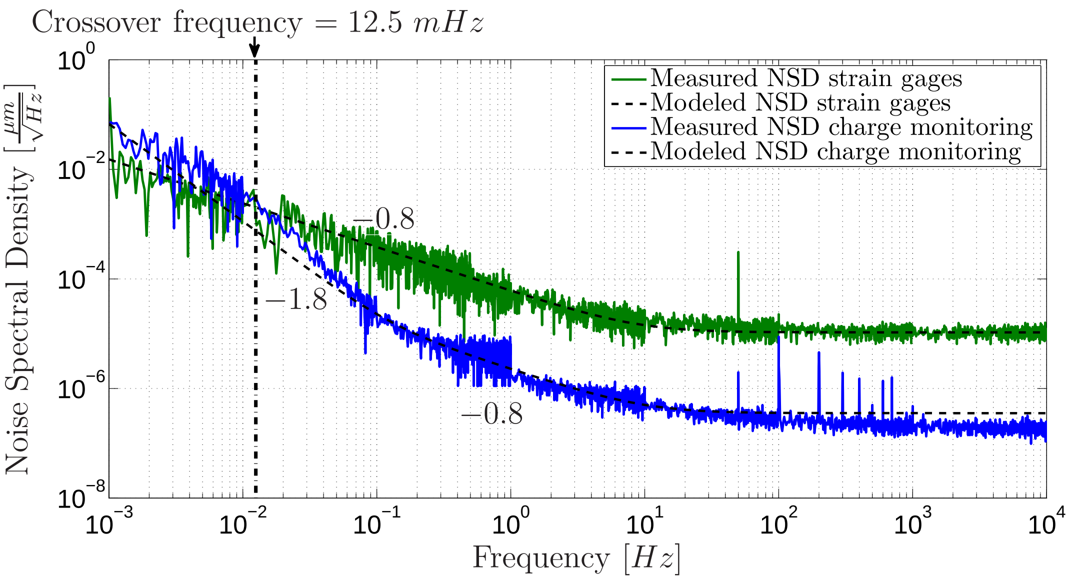

Figure 5.3: The NSD of charge monitoring (blue) and strain gages (green) is shown. A significant increase of noise is recognized at low frequencies due to the integrated 1/f-current noise. Although the strain gage measurement shows a higher noise level in the high frequency range, its low frequency noise is less pronounced. Below 12.5 mHz the noise spectral density of the strain gage measurement is lower than the noise spectral density of charge monitoring.

of charge monitoring, while below the crossover frequency the noise is determined by the strain gage measurement shown.

To get a benchmark,the resulting noise spectral density at the output of the complementary filter is compared with the capacitive sensor MicroSense 6810. The capacitive sensor is aligned on the same shortened piezo. The combination of strain gages and charge monitoring shows less random error over the whole required bandwidth, as shown in Figure 5.5. The combination of strain gages with charge monitoring provides a method which is easy to integrate and costs a fraction of a capacitive sensor.

The standard deviation at the output of the complementary filter is derived from the NSD as 0.56 nm between 1 mHz and 10 kHz. Over the same frequency range the capacitive sensor shows a standard deviation of 2.0 nm.

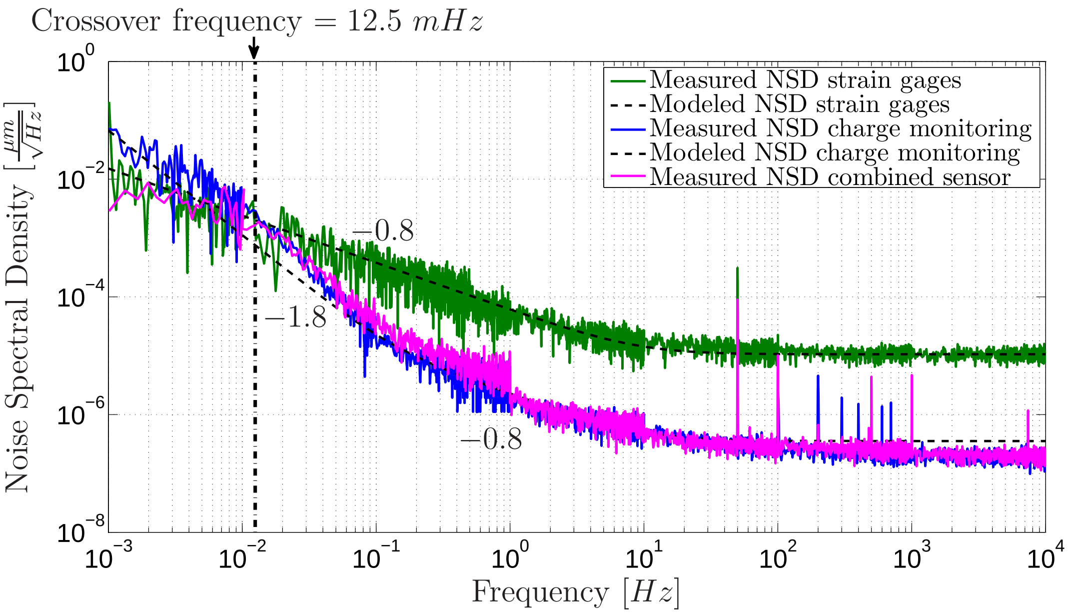

Figure 5.4: This graph shows the NSD at the output of the first-order complementary filter with the crossover frequency at 12.5 mHz (pink), the NSD of the strain gage measurement (green) and the NSD of charge monitoring (blue). Below the crossover frequency the noise of the combined signal is determined by the noise of the strain gage measurement. Above 1 Hz it follows the noise spectral density of charge monitoring. Between the crossover frequency and 1 Hz the NSD of the filter outcome is influenced by both sensors, due to the finite roll-off of the complementary filter.

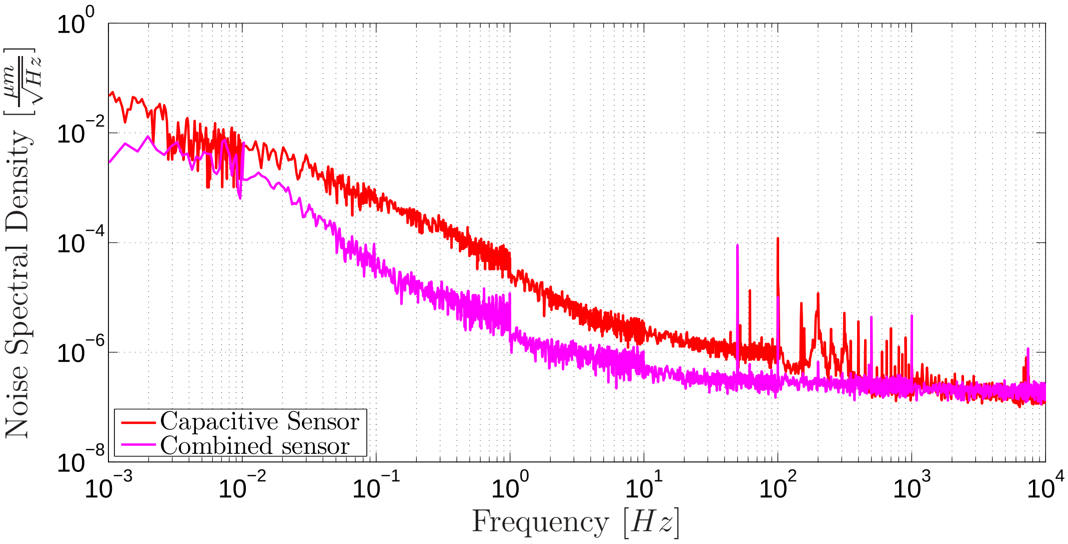

Figure 5.5: The noise spectral density of a capacitive sensor (red) is compared with the noise of the combination of strain gages and charge monitoring (pink). In the required bandwidth of 2 kHz the combined sensor shows a better behavior concerning noise than the capacitive sensor. Because of interference with the power line, peaks arise in the NSD of the capacitive sensor at 50 Hz and its harmonic.

Tube piezoelectric actuator

As the E-scanner is not equipped with strain gages the following assumptions have to be done. The same strain gages are assumed to be applied to the E-scanner as were used to measure the elongation of the stacked piezo. The strain gages are used with the same read out instrumentation, therefore it is assumed that the random noise is the same as in Figure 4.16.

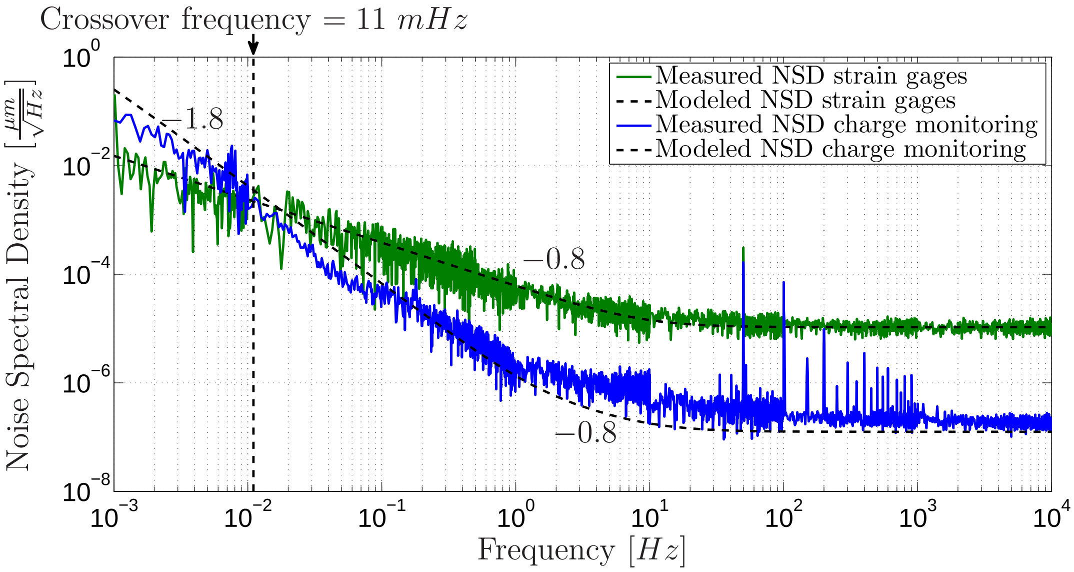

Figure 5.6: The random error of the strain gages depicted by the green line and charge monitoring applied to the E-scanner depicted by the blue line are compared. Below 10 mHz the random error of charge monitoring exceeds the random error of the strain gages.

With the introduced minimization approach from Section 5.1 a complementary filter with a crossover frequency of 11 mHz is obtained.

5.3 Summary

The standard deviations in the frequency range from 1 mHz to 2 kHz of the investigated sensors are derived from the measured NSD are given in Tabel 5.1. Allthough, charge monitoring has a lower NSD than the strain gage measurement over a wide frequency range, their standard deviations are nearly the same. This originates from the concentration of noise in the low frequency range, when doing charge monitoring. When reducing the bandwidth of charge monitoring to 10 mHz - 2 kHz, its standard deviation is already reduced to 0.27 nm. The uneven distribution of noise in charge monitoring indicates the potential of doing sensor fusion. After complementary filtering with a crossover frequency of 12.5 mHz a combined sensor principle is obtained with a standard deviation of 0.56 nm. Compared to the capacitive sensor, a sensor signal with nearly a factor 4 lower standard deviation is derived.

Table 5.1: Standard deviations of the investigated sensor principle in the bandwidth of $1\ mHz$ to $2\ kHz$.

Sensor principle	Standard deviation	Range
Charge monitoring applied to the stacked piezo	$2.2\ nm$	$12.6\ \mu m$
Charge monitoring applied to the tube piezo	$2.9\ nm$	$2.5\ \mu m$
Strain measurement with strain gages	$2.5\ nm$	$12.6\ \mu m$
Combined sensor	$0.56\ nm$	$12.6\ \mu m$
Capacitive sensor	$2.0\ nm$	$100\ \mu m$

CHAPTER 6

Sensor fusion including systematic error

The quality of a measurement acquired with an scanning system is determined by the resolution and the accuracy [67]. The resolution is defined as the smallest detail which can be resolved by the instrument. In relation to charge monitoring non-repeatable distortions such as noise and drift influence the precision of the measured elongation. In contrast to resolution the accuracy describes the extent of repeatable or systematic errors. Calibration errors and nonlinearities in the instruments can affect the accuracy of a measurement. The requirements on the accuracy of the positioning system are highly depending on the imaging application. When the exact dimension of measured sample feature is of interest, a high absolute accuracy of the instrument is requested. On the other hand there are applications, for which it is highly important to resolve different features on a sample, while the absolute dimension of the features are of lower interest. In Chapter 5 sensor fusion is done only with regard to random noise and therefore resolution. The potential of charge monitoring and strain gage measurement to minimize both, systematic and random error is investigated in this chapter.

6.1 Extraction of systematic error

The investigation of systematic errors in this Chapter is done by comparing the investigated sensor principles, with the measurement acquired by the capacitive sensor as reference sensor. Inevitable, the measured error consists next to the systematic error of the investigated sensor also of the random errors of investigated and reference sensor. To extract the systematic error, knowledge about the expected systematic error is used. The systematic error of charge monitoring is composed by three main error sources. Hysteresis is encountered as difference in increasing and decreasing branch. In addition to hysteresis an asymmetry is measured. Especially at reduced voltages applied to the piezo an error arises due to the deviation from the peak-to-peak gain from its nominal value at full range. Figure 6.1 shows a normalized symmetric hysteresis

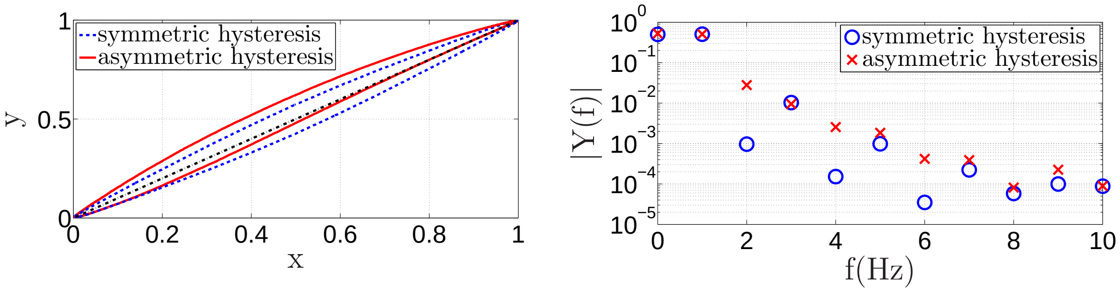

Figure 6.1: A symmetric hysteresis (blue) is compared with an asymmetric hysteresis (red). The decreasing steepness of the hysteresis with increasing range results in an asymmetry shown in the left figure. The symmetric hysteresis shows dominant odd harmonics. With asymmetry the even harmonics are increased.

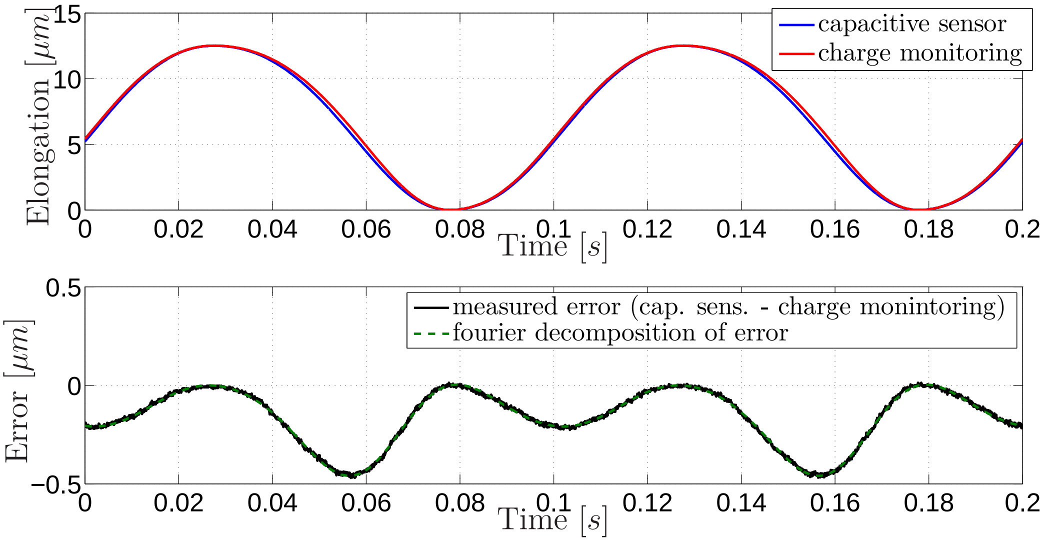

Figure 6.2: The error between charge monitoring and the elongation measured with the capacitive sensor is shown, while the piezo is driven over full range of 150 V and 10 Hz. Due to the residual nonlinearity a systematic error arises (cyan). To extract the systematic error a fourier decomposition with four harmonics of the error signal is used (green).

and its fast-fourier-transform (FFT) in red.

The odd fourier components are dominant in the FFT. Whenever asymmetry is included to the hysteresis, the even fourier components are increased. The peak-to-peak gain is a simple scaling factor and has therefore no influence on the ratio between the distinct fourier components. From the FFT of the signal distorted by an asymmetric hysteresis it can be concluded that a fourier decomposition with four harmonics can be used to extract the systematic error from the measurement noise [77] and thereby obtaining an RMS value of the systematic error consisting of hysteresis, asymmetry and error due to varying peak-to-peak gain. The decomposition is implemented with the Matlab function fit, with the fittype 'fourier5'. The approach is shown for the residual hysteresis, when a sinusoidal signal with maximum voltage of 150 V at 10 Hz is applied to the piezo in Figure 6.2. The measured systematic error (cyan) and its composition of the fourier components (green) coincide, except the random error which appears only in the measured signal.

6.2 Identification of systematic errors

Before presenting a method how to combine two measurement signals, the systematic errors of the introduced sensor principles are discussed.

6.2.1 Comparison of the residual hysteresis in charge monitoring via capacitor insertion and current integration

In Chapter 4 charge monitoring via capacitor insertion and charge monitoring via current integration are investigated in regard to the random error in the sensor signal. In this chapter the systematic error is of interest as well, therefore the potential of the introduced charge monitoring approaches to reduce nonlinearities are investigated. Further, a third approach is introduced to ensure that the sensing capacitor as well as the inverting integrator are not introducing any systematic error. The measured voltage drop over a shunt resistor in series to the piezo is measured and integrated digitally in Matlab. The elongation over the derived charge is depicted for all three approaches in Figure 6.3. Charge monitoring via capacitor insertion (blue crosses), charge monitoring by analog integration (red crosses) and digital integration (green line) show no remarkable difference. All three approaches reduce the initial hysteresis of 16.5% between voltage and elongation, to 2.0 % between charge and elongation. As in Chapter 5 charge monitoring via capacitor insertion is preferred to charge monitoring via current integration, due to less influence on the system and less noise.

6.2.2 Charge monitoring via capacitor insertion applied to the stacked piezo

The difference between dielectric and piezoelectric hysteresis is of high interest as it is the origin of residual hysteresis in charge monitoring [35], [36]. Further, their dependency on the voltage applied to the piezo is discussed. In addition to hysteresis a

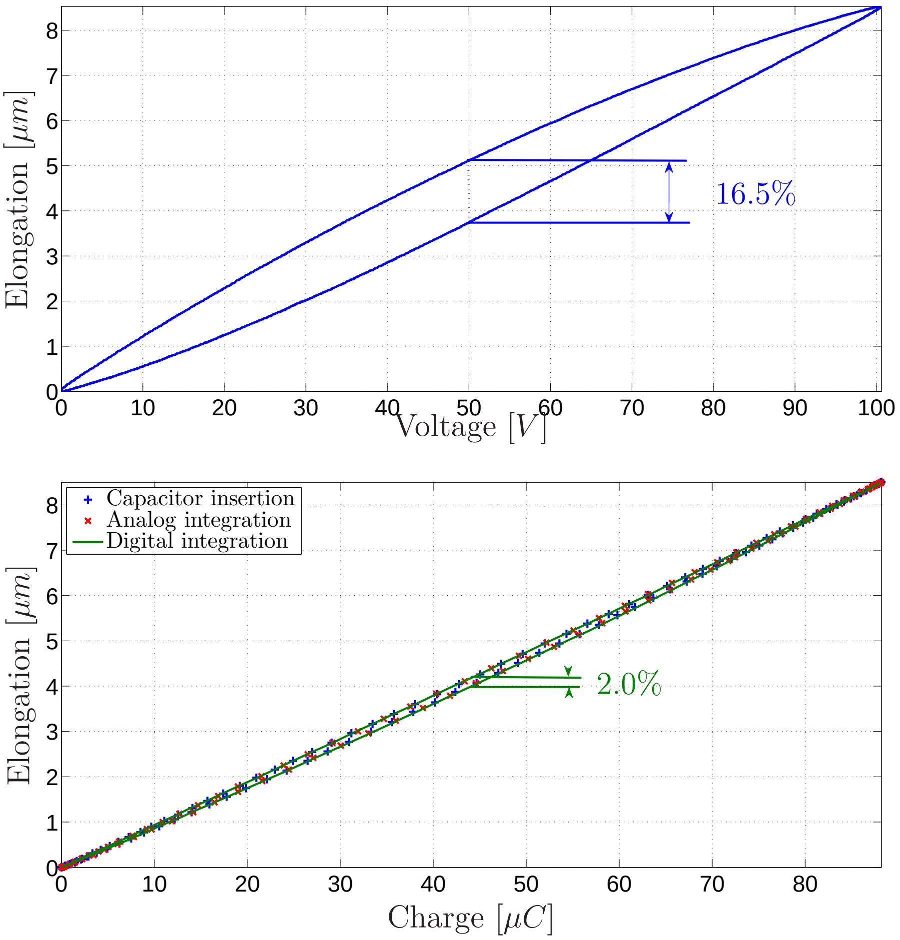

Figure 6.3: The residual hysteresis of charge monitoring implemented with capacitor insertion, analog and digital integration are compared. A signal with amplitude 100 V and frequency 10 Hz is applied to the piezo. No difference in residual hysteresis is measured between the different implementations of charge monitoring.

second nonlinear effect is encountered, which results in an asymmetry of the hysteresis. Both nonlinear effects are encountered also in the charge-elongation relationship. The maximum deviation between increasing and decreasing branches is related to the maximum value and given as relative hysteresis in percent, as shown in Figure 6.4. For the purpose of better representation and clarity at the half of the x-axis and y-axis a black dashed line is included. The distance of the average of decreasing and increasing branch in the mid-loop to the dashed line representing half magnitude is related to the maximum value and designated as asymmetry in percent. Further, a deviation from the nominal peak-to-peak gain, depending on the applied offset is observed. The residual nonlinearities in the charge-elongation relationship are investigated as they determine the systematic error in charge monitoring.

As discussed in Chapter 1, the movement of 180°walls contributes only to the dielectric hysteresis (electric field - polarization) but not to the piezoelectric field (electric field - strain) hysteresis. This effect leads to more hysteresis in the voltage-charge relation (16.7%) than in the voltage-elongation relation (15.1%) as shown in Figure 6.4. The asymmetry encountered in the voltage-charge relation is 7.5 %, while the asymmetry in the voltage-elongation relation is 5.1 %. For charge monitoring the difference between the shape of both hysteresis loops is crucial, as it impacts the residual hysteresis of charge monitoring. The residual hysteresis in the charge-elongation relation is 1.9 % and 2.6 % asymmetry is measured. Charge monitoring applied to the stacked piezo results in a reduction of hysteresis by 89 % over full range.

In comparison at weak fields 180°wall movements are less dominant. The response of strain (piezoelectric hysteresis) and polarization (dielectric hysteresis) to weak electric fields are mainly governed by movements of ferroelectric domain walls. Therefore, at weak fields the deviation between charge (polarization) and elongation (strain) is small, which results in small residual hysteresis of charge monitoring. Figure 6.5 shows the hysteresis in case that the piezo is driven over 20 % of its range. The relative hysteresis between voltage and charge (13.4 %) as well as the hysteresis between voltage and elongation (13.2 %) decreases only slightly compared to Figure 6.4. The hysteresis from Figure 6.5 contributes to the systematic error of charge monitoring and is strongly reduced from 13.2% to 0.4%. Over full range hysteresis are reduced by 89 %. In comparison the relative hysteresis is reduced by 97 %, when the piezo is driven over 20 % of its range. The higher efficiency of charge monitoring originates from the aforementioned dominance of ferroelectric domain wall movements at reduced voltage. Next to hysteresis an asymmetry of 0.5% is encountered. Beside the before treated hysteresis and asymmetry, another error source is determined. In Figure 6.6 the elongation-charge relation is depicted over 20% of its voltage range (red). In comparison the same measurement is figured with 150 V applied to the piezo (blue). A significant difference in the peak-to-peak gain over full range and 20% of the range is shown. This change in peak-to-peak gain originates from the overall asymmetry of 2.6% at 150 V applied to the piezo. Further, the measured charge over 20% of its range (red) follows the rising branch of the measurement with full range (blue). This contributes further to the change in slope over different ranges.

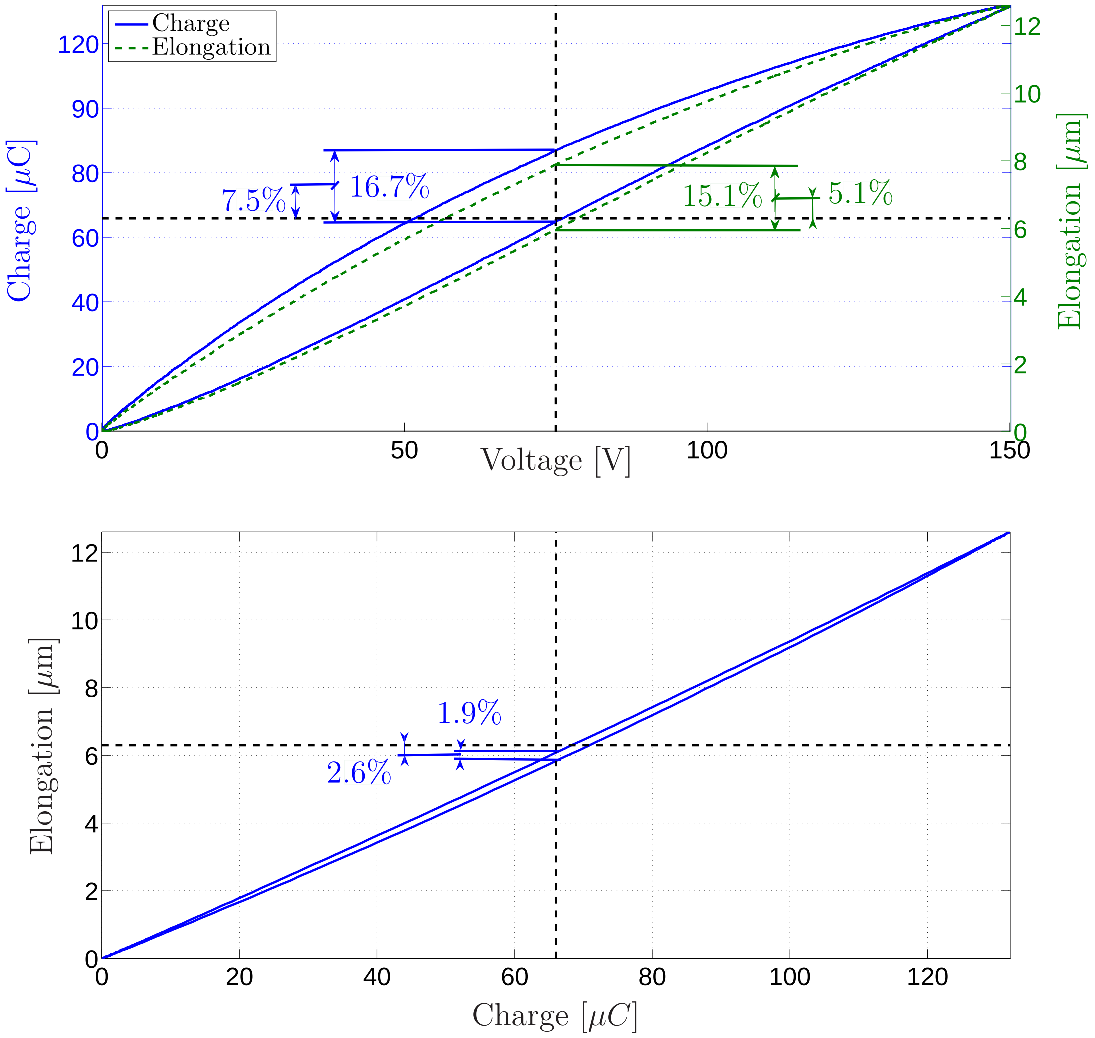

Figure 6.4: The dielectric and piezoelectric hysteresis are compared above and below the residual hysteresis in charge monitoring over full range is shown. The elongation of the stacked piezo over full range is shown in green in the above figure. The voltage-elongation relation shows a hysteresis of 15.1% and a asymmetry of 5.1%. For comparison the hysteresis between charge and applied voltage in blue is 16.7%. Further an asymmetry of 7.5% is measured. The difference in the dielectric (polarization - electric field) and piezoelectric (strain - electric field) hysteresis from the above figure results in a hysteresis in the elongation over charge shown below. The hysteresis between charge and elongation is 1.9%. Next to hysteresis an asymmetry of 2.6% is measured.

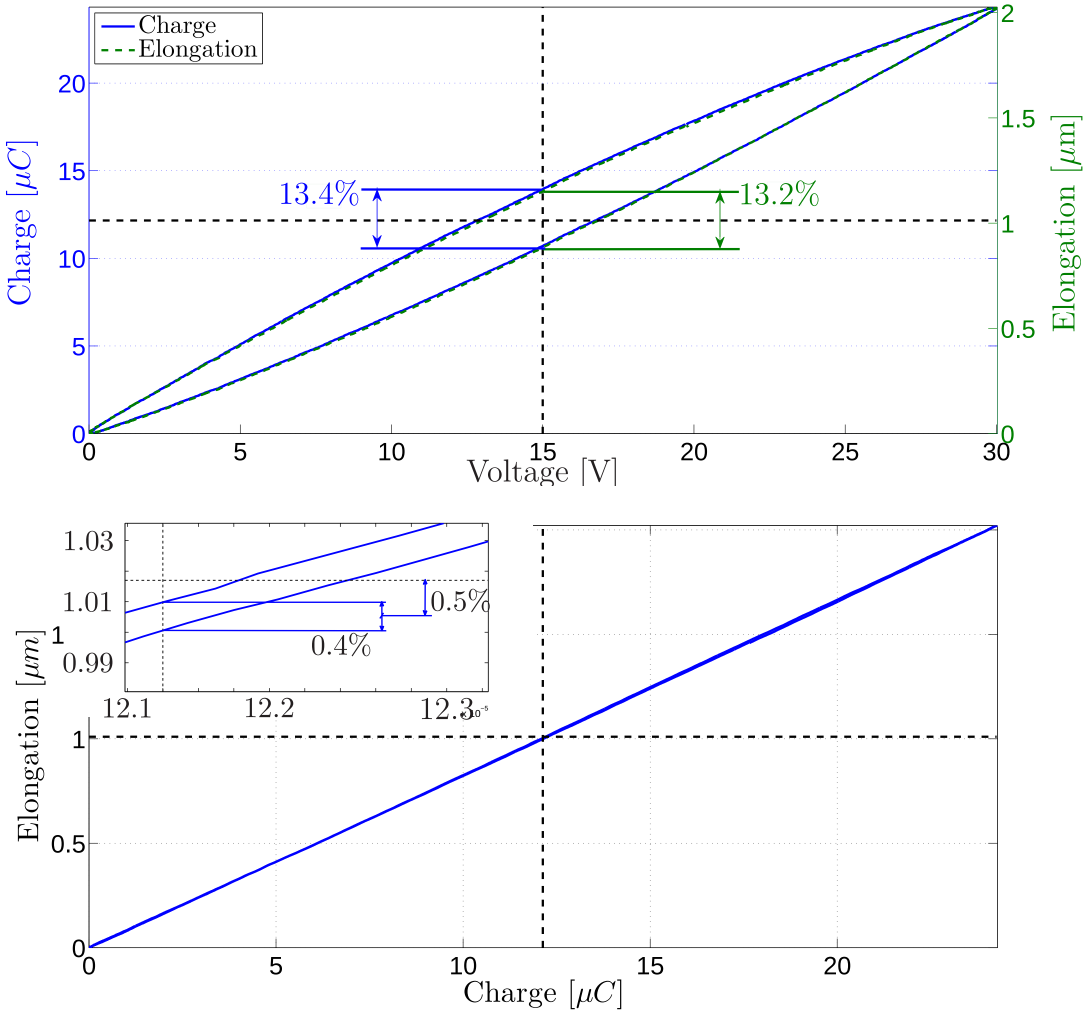

Figure 6.5: The reduced residual hysteresis at weaker fields in comparison to Figure 6.4 is shown. The dielectric and piezoelectric hysteresis are compared above and below the residual hysteresis in charge monitoring over 20% of its range is shown. Over 20% of its voltage range the hysteresis of the piezo between voltage and elongation (in green) is still 13.2%. Further an asymmetry of 0.2% is encountered. In comparison, the hysteresis between applied voltage and measured charge (blue) is 13.4% with an asymmetry of 0.7%. As both hysteresis in the upper figure are dominated mainly by movements of domain walls, their amount is nearly equal. Therefore, the hysteresis between charge and elongation is reduced to 0.4%, while still an asymmetry of 0.5% is encountered.

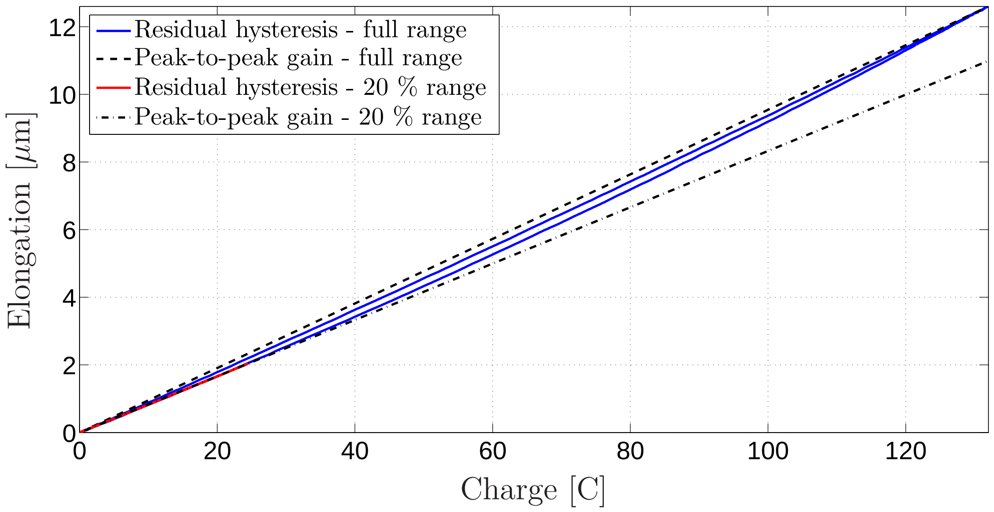

Figure 6.6: The elongation over charge is compared over full range (blue) and 20 % of its range (red). A significant deviation of the peak-to-peak gains exists between both measurements. This error originates from the change in steepness over range. Further, the measurement with reduced range (red) tracks the rising branch of the hysteresis measured when the piezo is actuated over full range.

6.2.3 Charge monitoring via capacitor insertion applied to the tube piezo

The stacked piezo has high nonlinearities and offers thereby the investigation of piezoelectric and dielectric hysteresis over range. In comparison charge monitoring is applied to the tube piezo with low inherent nonlinearities. The hysteresis between voltage and elongation is measured at 10 Hz with an amplitude of 175 V. The relative hysteresis in the mid-loop is 1.3 %. Similar to the observations at the stacked piezo an asymmetry of 1.2 % is measured.

The hysteresis encountered between charge and elongation is less than 0.3 %. An asymmetry of approximately 0.2 % is measured.

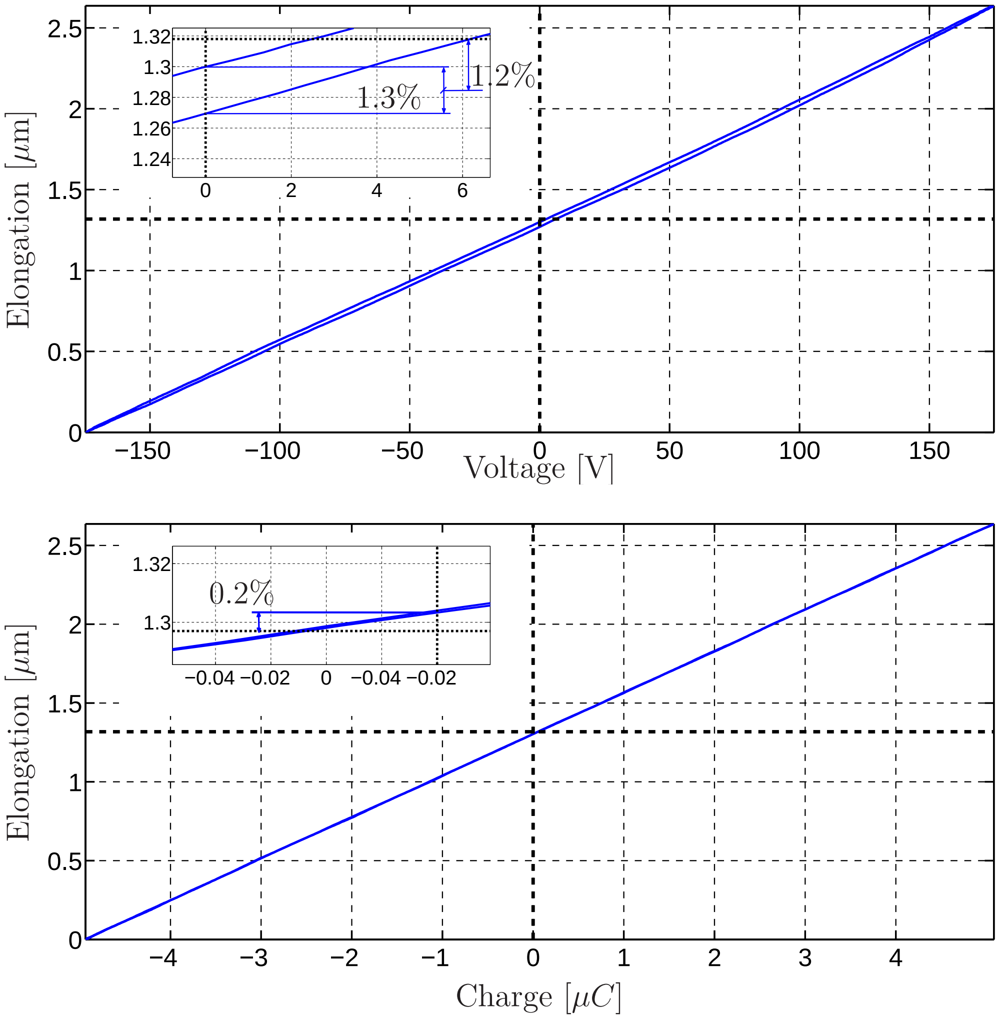

Figure 6.7: The hysteresis between voltage applied to the tube piezo and elongation in z-direction is shown. A hysteresis of 1.3% is measured. Next to hysteresis the E-scanner also shows an asymmetry of 1.2 %. The charge of the piezo is acquired by charge monitoring and depicted at the x-axis. Between elongation (on y-axis) and charge a hysteresis smaller than 0.3% can be recognized. In addition an asymmetry of 0.2 % is measured.

6.2.4 Strain measurement with strain gages

The error between the strain gage measurement (red) and the elongation measured by the capacitive sensor (blue) is shown in Figure 6.8. According to Chapter 4 the read-out system is designed to reach the required peak-to-peak gain at full range. Therefore, the error (green) is vanishing at full range. Due to the inherent nonlinearity of the strain gages, a maximum error of 0.4% arises at half range. As the error appears in the increasing and decreasing branch it shows twice the frequency of the driving signal. The aforementioned fourier decomposition is used to extract the systematic error from the random error introduced by the strain gages and capacitive sensor. With the reduced range (20%) the same nonlinearity results in a difference in magnitude between strain gage measurement and reference measurement. The resulting error in this range shows the same frequency as the driving signal.

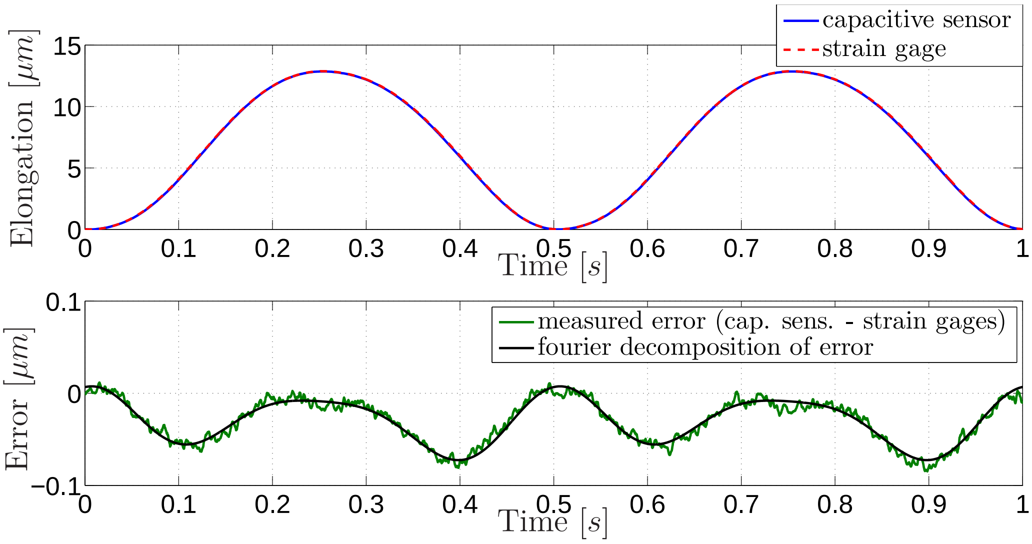

Figure 6.8: The error between strain gage measurement and reference measurement done with the capacitive sensor is shown. The piezo is driven over full-range (150 V) with 2 Hz. The inherent nonlinearity of the strain gage measurement (red dashed) results in an error of 0.4 % compared to the reference measurement done with a capacitive sensor (blue). The fourier decomposition of the error is depicted by the black line.

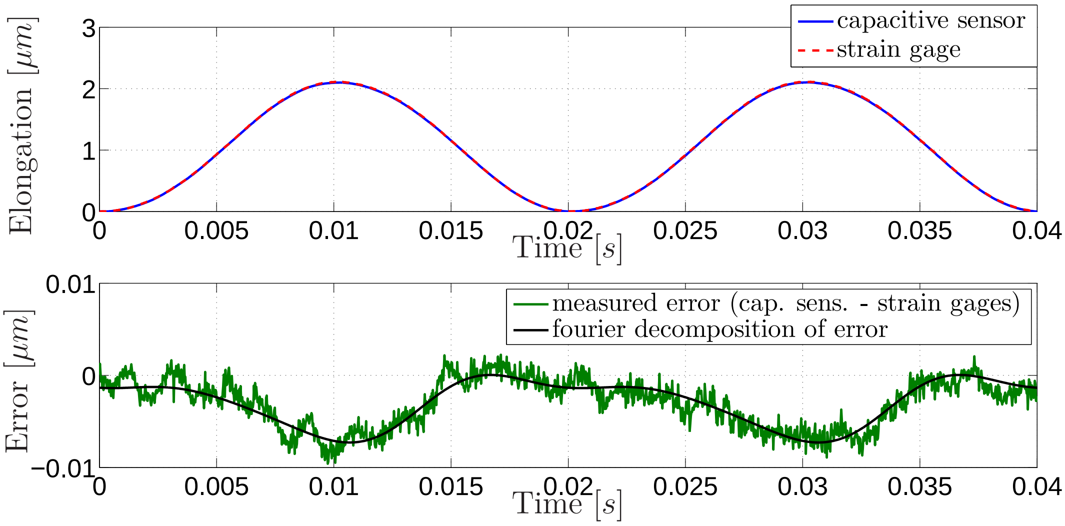

Figure 6.9: The error between the strain gage measurement and the reference measurement done with a capacitive sensor is depicted, while the piezo is driven over 20% of its range at 50 Hz. The nonlinearity of the strain gage measurement (red) results in an error (green) compared to the reference measurement done with a capacitive sensor (blue). The error is mainly dominated by a different magnitude between strain gage measurement and the reference elongation. The fourier decomposition of the error is depicted by the black line.

6.3 Analysis of uncertainty

In the previous Section residual hysteresis in charge monitoring are investigated over different range. In order to obtain a complementary filter with high accuracy, these information can not be left out. For optimizing the crossover frequency of a complementary filter, spectral information about the systematic error of charge monitoring as well as strain gage measurement is required. Common approaches to acquire such information are based on superposition and thereby restricted to linear systems. To allow an estimation of the spectral distribution of the systematic error a new method is required.

In difference to random errors, the systematic error depends on the applied signal. When using complementary filters the crossover frequency can be adjusted to the expected signal, in order to minimize the uncertainty, which is different for different signals. Therefore, the applied signal needs to be defined upfront. In Chapter 4 the expected spectra for scanning systems are introduced. For the scanning motion the envelope of a triangular signal with its fundamental frequency at the line scan rate of 10 Hz is expected. These spectrum shows constant amplitude up to the line scan rate followed by a decrease with a slope of -2. On the other hand, for the vertical actuator of an AFM, a constant amplitude up to the line scan rate followed by a decreasing amplitude with a slope of -1 is expected.

Depending on the expected signal applied to the piezo, the spectral composition of the systematic error needs to be estimated. Therefore, sinusoidal signals along the spectrum of interest are applied to the piezo successively after each other. The systematic error between investigated sensor system and reference sensor is acquired. This error is concentrated to the spectral component of the systematic error at the frequency of the applied signal.

As the amplitude spectral density is the square root of the PSD, the RMS value of the measured error are depicted over frequency in Figure 6.10 and Figure 6.11 for charge monitoring and strain gage measurement, respectively.

The difference between measurement and true value can be decomposed into two components, systematic and random error [98], [99]. Suppose a measurement x with a systematic error S as well as a random error σ. The measurement x can be treated as having two parts x_R with random error σ and x_S with systematic error S. With the definition of the expected value from Equation (4.1) the variance of x is derived by

$$\begin{aligned} V(x_1) &= \overline{x^2} - \overline{x}^2 \\ &= \overline{(x_R + x_S)^2} - \overline{x_R + x_S}^2 \\ &= \overline{x_R^2} + \overline{x_S^2} + 2\overline{x_R x_S} - \overline{x_R}^2 - \overline{x_S}^2 - 2\overline{x_R x_S} \quad = \sigma^2 + S^2 \end{aligned} \tag{6.1}$$

with the variance of the random error σ^2 as defined in Chapter 5 and the variance of the systematic error S^2. Therefore, the random and systematic error are summed in quadratic manner.

After summing the random error and systematic error in quadrature, the overall uncertainty of the sensor principles over frequency is derived. Based on the nonlinearity of charge monitoring the resulting systematic error depends on the DC value summed to any sinusoidal signal, which is applied to the piezo. As shown in Figure 6.6 the highest systematic error appears at the lower and upper boundary of the piezo's voltage range, as in this range the peak-to-peak gain shows the highest deviation from its nominal value. To take the worst-case systematic error into account each applied sinusoidal signal has its lowest value at 0 V.

6.3.1 Uncertainty of sensor principles

The aforementioned approach is used to derive an expectation of the systematic error over frequency, for each sensor principle. The systematic and random error are added in quadrature to derive the uncertainty. Which is used to determine the crossover frequency of the complementary filter, in order to reduce the uncertainty. As the systematic error depends on the applied spectrum, the calculation is done twice. Once for the spectrum of a triangular signal with full voltage range depicted in Figure 3.2 in blue and once for the expected spectrum of the Z-piezo shown in Figure 3.2 red.

Stacked piezo

With 20% of its voltage range applied to the piezo the hysteresis (0.4 %) and asymmetry (0.5 %) is already heavily reduced as shown in Figure 6.5. However, the deviation to the nominal peak-to-peak gain shown in Figure 6.6 dominates the error. The reduced

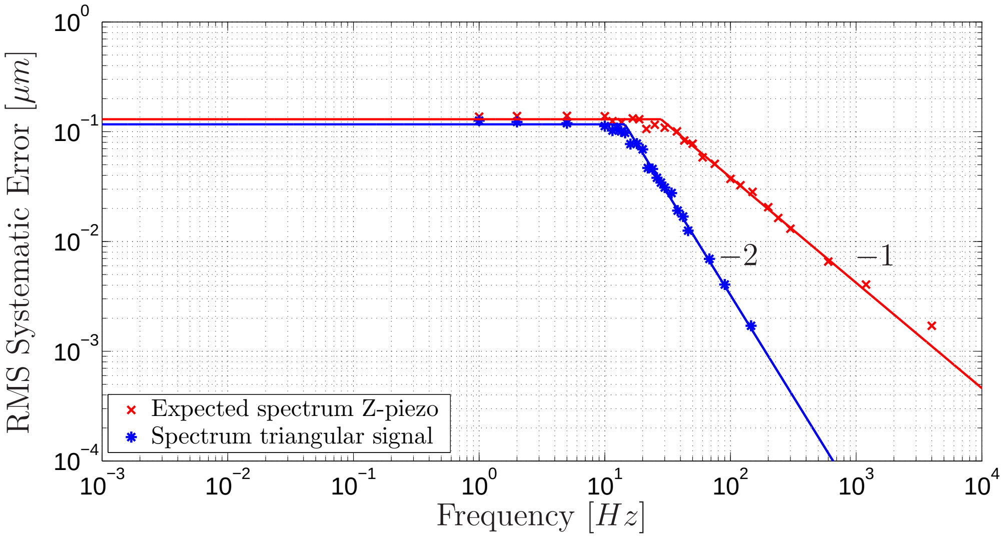

Figure 6.10: The systematic RMS error between charge monitoring applied to the stacked piezo and capacitive sensor is depicted over frequency. The blue measurement refers to the enveloping spectrum of a triangular signal (blue in Figure 3.2) applied to the piezo. Up to the frequency of 14 Hz the RMS error is approximated by a constant error of 0.12 μm. Above the error decreases with a slope of -2. In red the RMS error is shown, while the signal along the spectrum depicted in red in Figure 3.2 is applied to the piezo. The RMS error is approximated by a constant error of 0.13 μm up to a frequency of 28 Hz. Above the RMS error decreases approximately with a slope of -1.

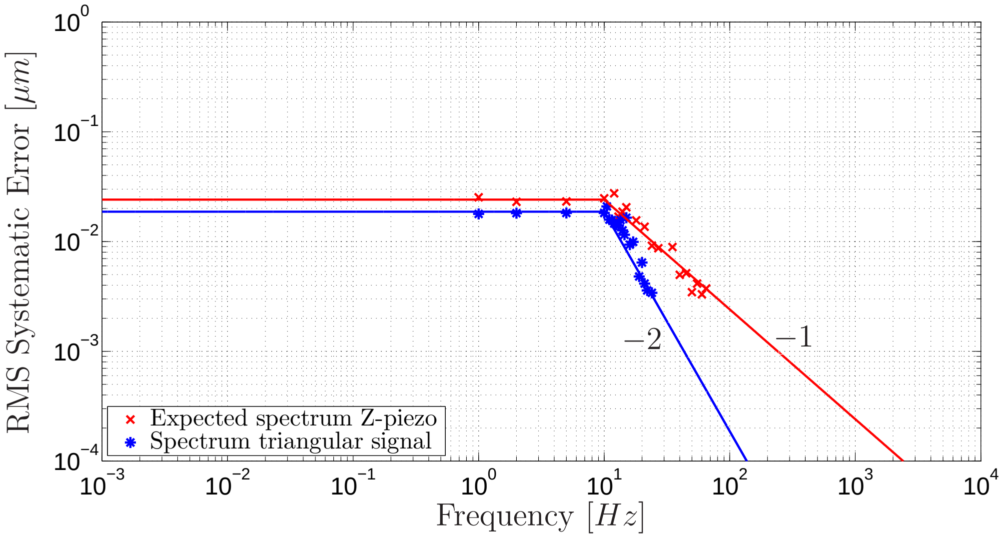

Figure 6.11: The RMS value of the systematic error between the strain gages measurement and the reference measurement. The measurement in red and blue regards to signals applied along the red and blue spectra in Figure 3.2. The measurement according to the expected spectrum at the Z-piezo shows a constant error of 0.024 μm and the measurement according to the triangular signals an error of 0.019 μm. Above the line scan rate the error decreases proportionally with the applied signal, with a slope of -1 and -2 respectively.

peak-to-peak gain at lower voltage makes an appearance as downscaled measurement compared to the true elongation, resulting in a systematic error, which is proportional to the applied signal. Thereby, the systematic error in Figure 6.10 decreases with the same slope as the applied spectra depicted in Figure 3.2. A similar result is derived for the systematic error of strain gages, as it is also dominated by error due to different sensitivities at low voltages.

In Figure 6.12 the systematic error of strain gages (dashed green) is compared with its random error (green solid). The systematic error is measured along the spectrum, which is expected for the Z-piezo in AFM (shown in red in Figure 3.2). Above the line scan rate of 10 Hz the systematic error of the strain gage measurement decreases with a slope of -1. The systematic error of the strain gage measurement is higher than its random error over the whole measurement.

The systematic error of charge monitoring is measured along the spectrum, depicted in Figure 3.2 in red. The resulting systematic error is shown by the blue dashed line in Figure 6.13 and compared to the random error depicted by the solid line. Although the systematic error decreases above 28 Hz with a slope of -1, there is no crossing point between systematic error and random error. With the required spectrum charge monitoring shows more systematic error than random error over the whole measurement range.

In order to approximate the overall uncertainty, the random error and the system-

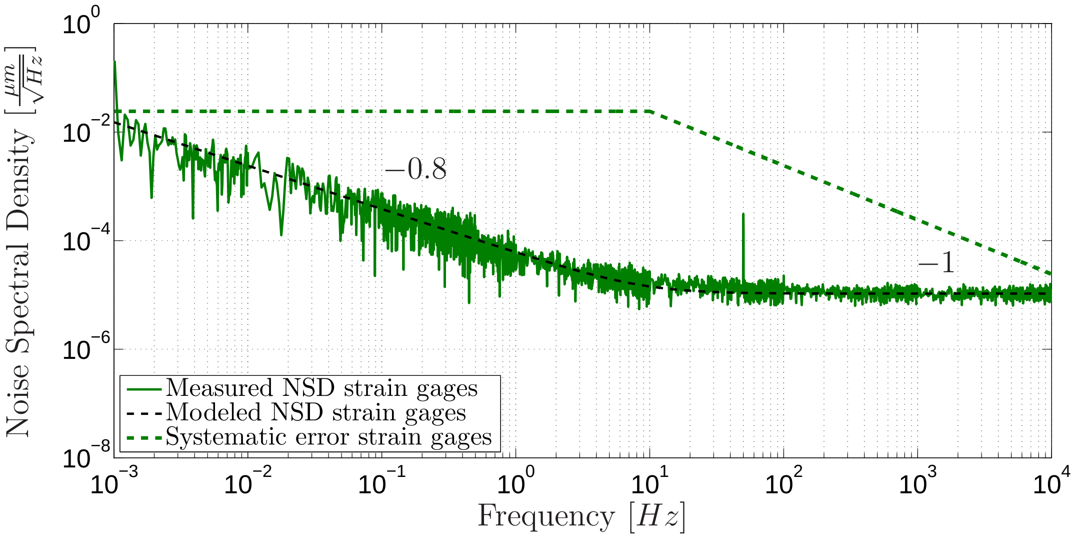

Figure 6.12: The systematic error of the strain gage measurement is shown by the dashed green line. The systematic error refers to the spectrum depicted in Figure 3.2 in red. Above the line scan rate of 10 Hz the systematic error decreases with a slope of -1. The solid line shows the NSD of the strain gage measurement. The systematic error is of higher extent than the random error over the whole measurement range.

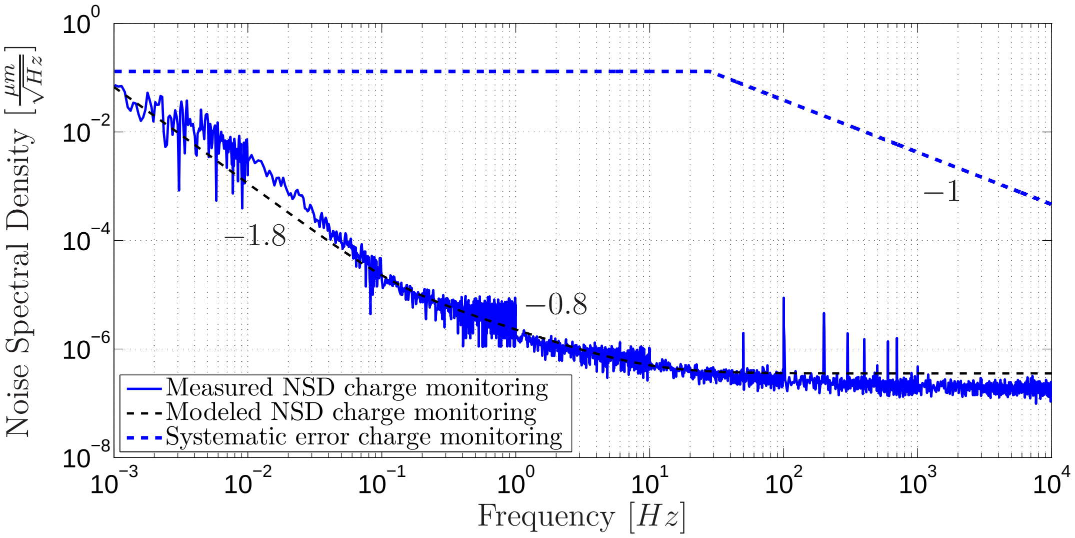

Figure 6.13: The dashed line represents the systematic error of charge monitoring along the spectrum shown in Figure 3.2 in red. Beyond 28 Hz the systematic error decreases proportionally with increasing frequency. The noise spectral density of the random signal (solid line) is below the systematic error over the whole range.

atic error are summed up quadratically. The resulting overall uncertainty of the strain gages is shown in Figure 6.14 in green and compared with the uncertainty of charge monitoring shown in blue. The uncertainty of charge monitoring is higher than the uncertainty of the strain gage measurement over the whole frequency range. In respect to the overall uncertainty, strain gages are preferable whenever the spectrum depicted in Figure 3.2 in red is applied to the input. Therefore, sensor fusion of charge monitoring and strain gages combined involve no benefit compared to using strain gages on their own.

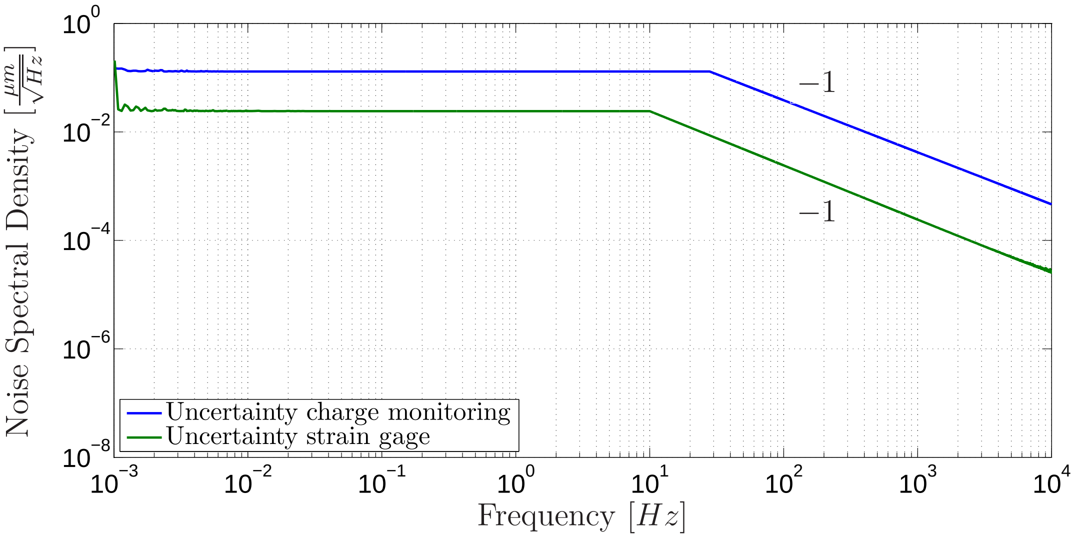

Figure 6.14: The random and systematic error from Figure 6.13 and 6.12 are summed up in a quadratic manner in reference to equation (6.1). The resulting uncertainty of the strain gage measurement and charge monitoring are shown in green and blue. The uncertainty of charge monitoring is above the uncertainty of the strain gage measurement over the whole range.

The same approach as before is now used to determine the uncertainty of strain gages and charge monitoring along the spectrum of the triangular signal depicted in Figure 3.2 in blue. Although the systematic error of charge monitoring (dashed blue) in Figure 6.15 decreases quadratically above 14 Hz, it is higher than the random error of charge monitoring (solid blue) over the whole measurement range. Above the line scan rate of 10 Hz the systematic error (dashed green) of the strain gages decreases with a slope of -2. Above 400 Hz the systematic error of the strain gages falls below the random error of the strain gages (green solid).

The uncertainty of charge monitoring represented by the blue line in Figure 6.16 is dominated by the systematic error over the whole frequency range. A crossing point consists between the uncertainty of the strain gage measurement (green) and the uncertainty of charge monitoring (blue). Nevertheless, this crossing point is found at 2300 Hz, which is above the used sensor bandwidth of 2000 Hz. The performance of strain gage measurement (depicted by the green line) and charge monitoring (depicted

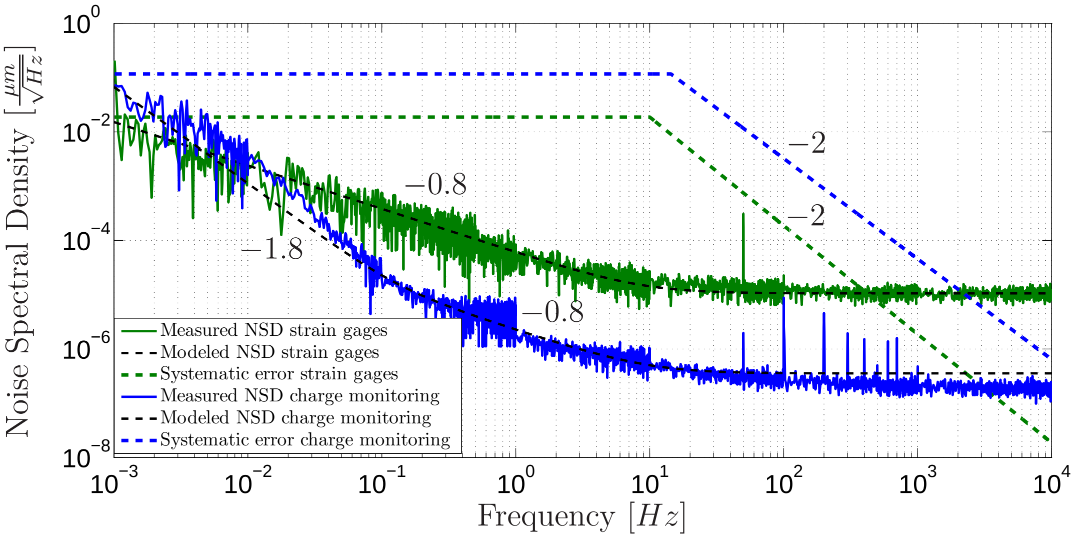

Figure 6.15: The systematic error of strain gages (dashed green) and charge monitoring (dashed blue) are related to the spectrum applied to the piezo depicted in Figure 3.2 in blue. The systematic error of charge monitoring decreases with a slope of -2 above 14 Hz. Nevertheless, there is no crossing point with the random error of charge monitoring shown by the blue solid line. The systematic error of the strain gage measurement decreases with a slope of -2 above the line scan rate of 10 Hz. Thereby, the systematic error of the strain gages falls below its random error (green, dashed) above 400 Hz.

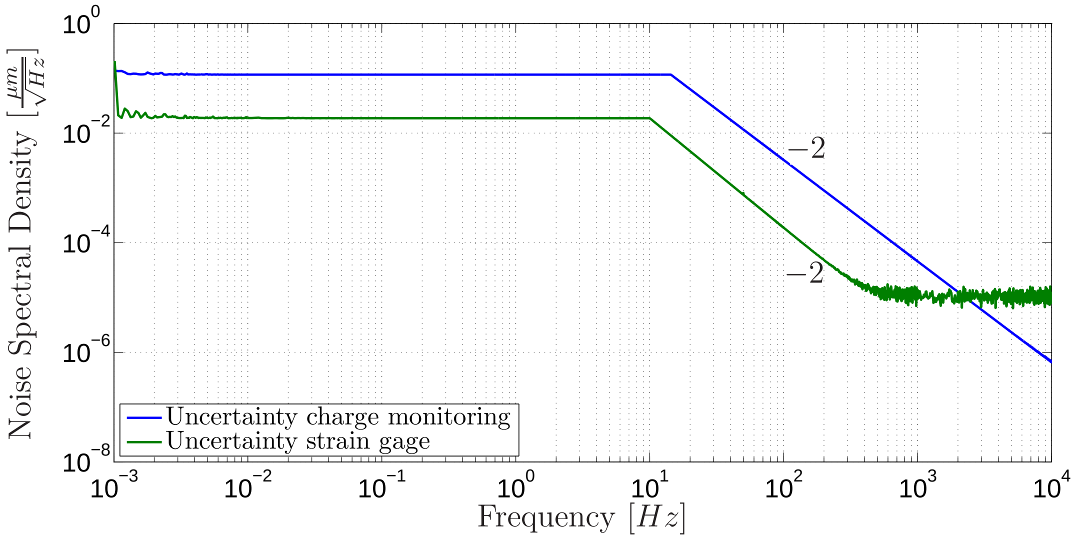

Figure 6.16: The random and systematic errors from Figure 6.15 are summed up in a quadratic manner, respectively. The resulting uncertainty of the strain gage measurement (green) and charge monitoring (blue) are shown above. A crossing point between the uncertainty of charge monitoring and strain gage measurement exists at 2300 Hz.

by the blue line) are compared, while a triangular signal with a maximum value of 150 V and 10 Hz is applied to the piezo in Figure 6.17. Although the hysteresis is reduced by 90% charge monitoring shows a maximum relative error of 2.4 %. In comparison the maximum relative error of the strain gage measurement is only 0.4%.

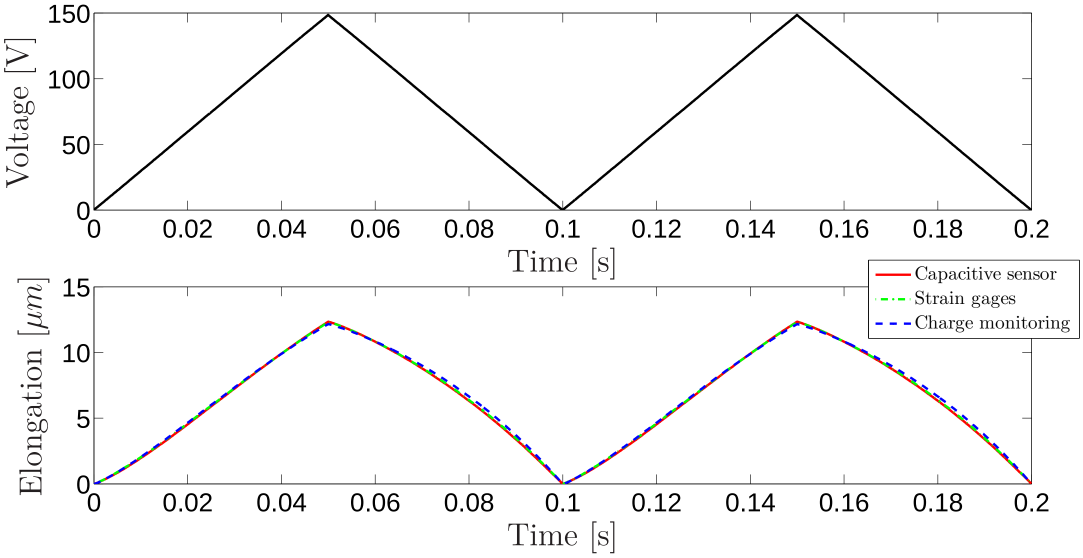

Figure 6.17: Charge monitoring and strain gage measurement are compared with a triangular signal applied to the piezo. The above Figure shows the triangular signal with a maximum of 150 V and 10 Hz applied to the piezo. The resulting elongation is measured with a capacitive sensor (depicted by the red line), charge monitoring (depicted by the blue line) and strain gage measurement (depicted by the green line).

Tube piezo

The same sensor fusion process with taking the systematic error into account is conducted with the tube piezo as it is applied to the stacked piezo. The systematic error of the stacked piezo and E-scanner are both composed by residual hysteresis and asymmetry. Although, the nonlinearities are inherently lower in the tube piezo. Therefore, it is assumed that in both piezos the same decrease in systematic error appears along the required spectra shown in Figure 3.2.

The RMS value of error between charge monitoring and the capacitive sensor is 2.5 nm at full range (350 V_{pp}) of the used piezo amplifier Falco Systems WMA-02 (Falco Systems, Amsterdam, The Netherlands). This error represents the systematic error up to 28 Hz in Figure 6.18. As the error in the tube piezo is similar composed by hysteresis and asymmetry, it is expected that the systematic error of the tube piezo shows the same behavior over frequency as the stacked piezo. In accordance to Figure 6.13 the systematic error decreases with a slope of -1 above 28 Hz, with signals along the spectrum depicted in Figure 3.2 in red applied to the actuator. The E-scanner

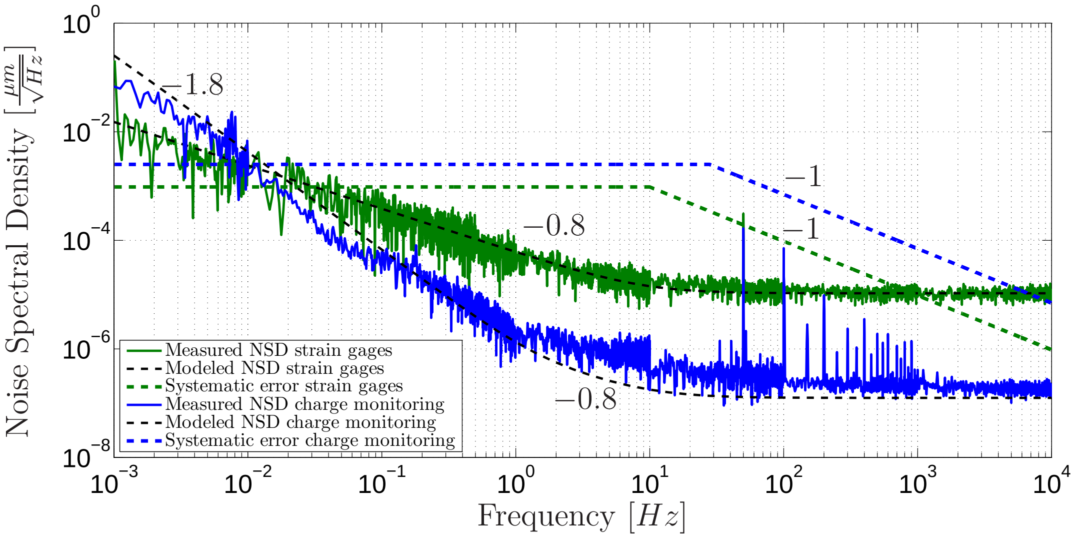

Figure 6.18: The systematic and random error of charge monitoring and strain gages are compared, with the spectrum depicted in Figure 3.2 in red applied to the piezo. The systematic error of charge monitoring (blue dashed) decreases with a slope of -1 above 28 Hz. The random error of charge monitoring (blue solid) exceeds the systematic error (blue dashed) below 10 mHz. Beyond the line scan rate of 10 Hz the systematic error of the strain gage measurement (green dashed) decreases with a slope of -1. Below 26 mHz and above 100 Hz the random error of the strain gages exceeds the systematic error.

performs an elongation of 2.6 μm when maximum voltage of 350 V_{pp} is applied. The expected systematic error of the strain gages at 2.6 μm is 0.96 nm. Compared to Figure 6.11 this error is reduced, as the error appearing due to the peak-to-peak gain is not taken into account. This assumption is valide as the strain gage measurement sensitivity would be adapted to the maximum value at an elongation of 2.6 μm. Above the line scan rate this error decreases quadratically. In accordance to Chapter 6 the random and systematic error are summed up to the uncertainty shown in Figure 6.19.

The uncertainty of charge monitoring depicted in blue is higher than the uncertainty of the strain gage measurement in green up to 7 kHz. The bandwidth of the combined sensor is 2 kHz. Therefore, the strain gage measurement is beneficial concerning uncertainty over the whole bandwidth.

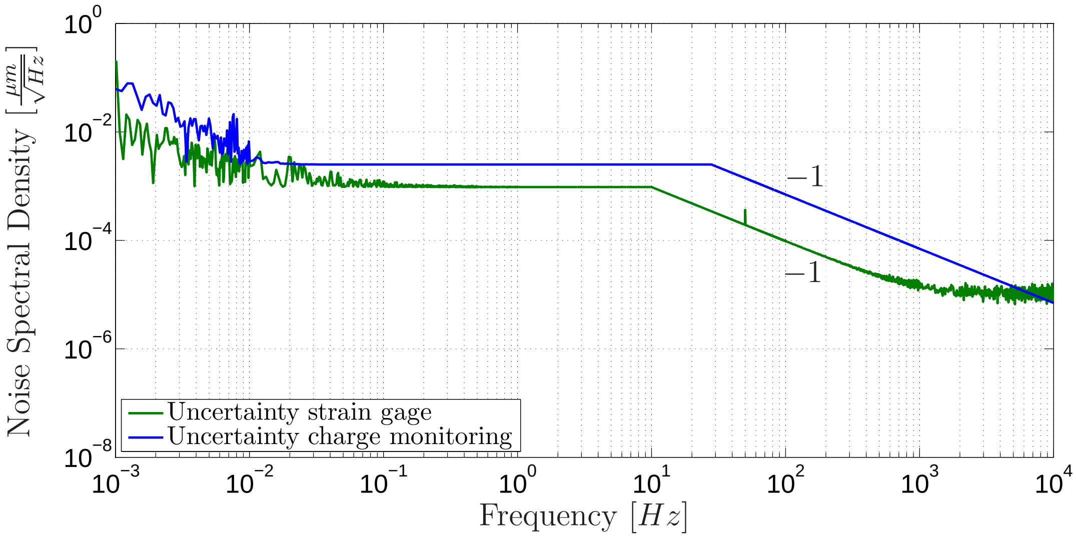

Figure 6.19: The random and systematic error from Figure 6.18 are summed up quadratically. The resulting uncertainty of charge monitoring and strain gage measurement are depicted in blue and green respectively. The uncertainty of charge monitoring is higher than the uncertainty of the strain gage measurement below 6.7 kHz. The crossing point between both uncertainties is already above the sensor bandwidth of 2 kHz.

In Figure 6.20 the systematic error is related to the spectrum depicted in Figure 3.2 in blue. The systematic error of the strain gages decreases with a slope of -2 above 14 Hz. Due to the integrated 1/f-current noise the random error of charge monitoring exceeds the systematic error below 10 mHz.

The resulting uncertainty are shown in Figure 6.21. The crossing point of the uncertainty of charge monitoring (blue) with the uncertainty of the strain gages (green) at 170 Hz indicates the possibility of complementary filtering. With the approach introduced in Section 5.1 the crossover frequency is derived at 454 Hz. The slope of the uncertainty of charge monitoring (-2) is higher than the slope of the first order

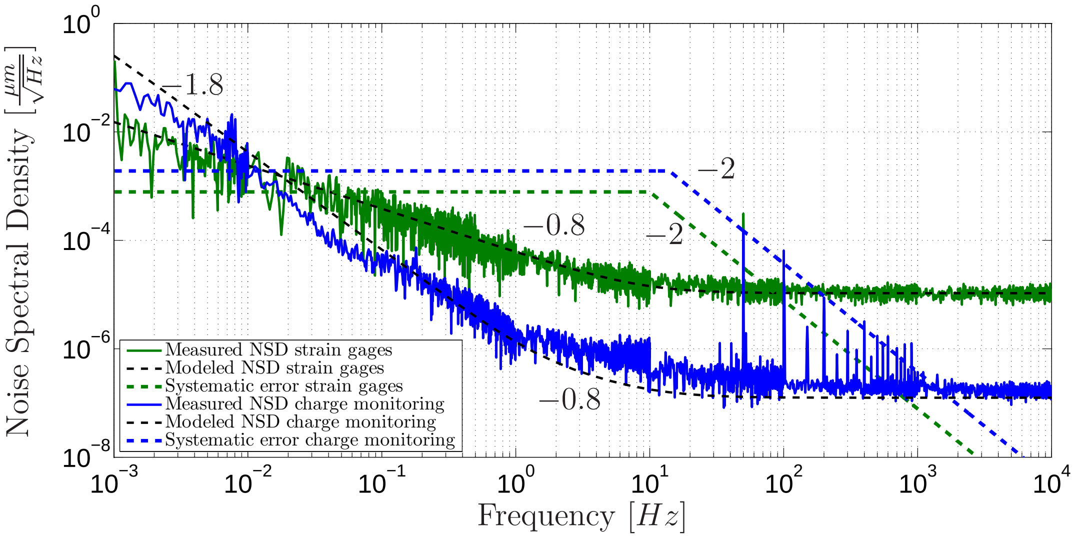

Figure 6.20: The systematic and random error of charge monitoring and strain gages are compared, with the spectrum depicted in Figure 3.2 in blue applied to the piezo. The systematic error decreases with a slope of -2 above 14 Hz. Between 10 mHz and 1862 Hz the systematic error of charge monitoring (dashed blue) is higher than its random error (solid blue). The systematic error of the strain gage measurement (dashed green) decreases with a slope of -2 above the line scan rate of 10 Hz. The random error is shown by the green solid line.

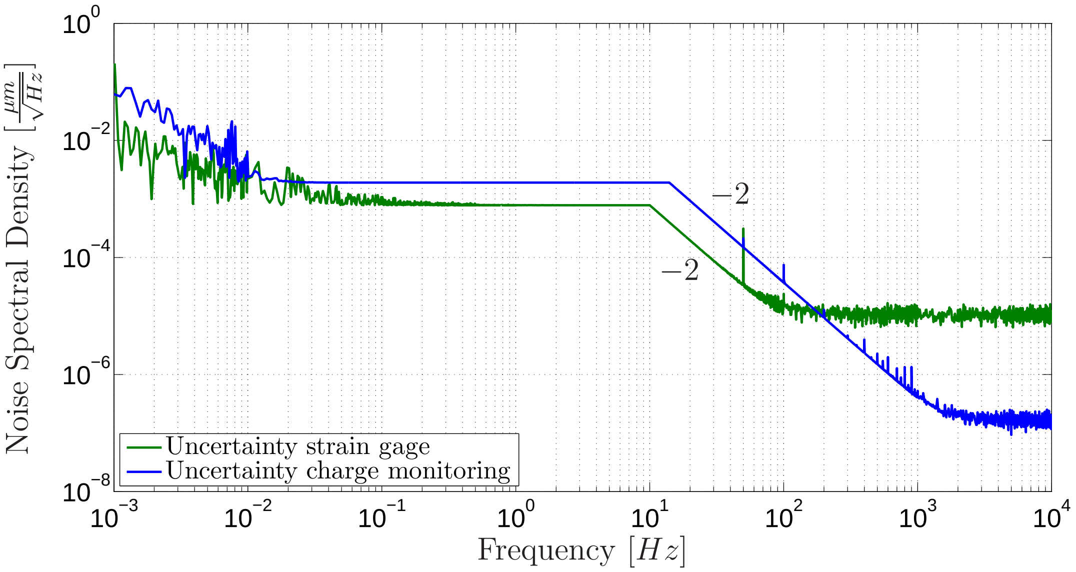

Figure 6.21: The random and systematic errors from Figure 6.20 are summed up quadratically. The resulting uncertainty of the strain gage measurement is shown in green and in blue the uncertainty of charge monitoring is shown. At low frequencies the uncertainty of charge monitoring dominates. Above 170 Hz the uncertainty of charge monitoring falls below the uncertainty of the strain gages.

complementary filter discussed in section 5.1. Therefore, the crossover frequency is higher than the crossing point of the uncertainty.

The residual hysteresis could be reduced to less than 0.3 % with charge monitoring applied to the E-scanner. Nevertheless, in a large part the strain gages still perform better concerning uncertainty than charge monitoring. For the expected spectrum of the Z-piezo in closed-loop (depicted in Figure 3.2 in red) the strain gages show less uncertainty over the whole required bandwidth of 2 kHz.

6.4 Summary of sensor fusion including systematic error

The investigated nonlinearities make an appearance as hysteresis, asymmetry and difference in peak-to-peak gain. The stacked piezo as well as the tube piezo nonlinearities are composed by the same nonlinearities although different in extent. Theses nonlinearities arises in charge monitoring as well although highly reduced. When accuracy is of importance, these information can not be left out, when designing a complementary filter. For designing the crossover frequency of a complementary filter, spectral information about the systematic error is needed. Common approaches, such as superposition, to acquire such information are restricted to linear systems. To allow an estimation of the spectral distribution of the systematic error, single sinusoidal signals along the spectrum of interest, are applied to the piezo. The acquired systematic error between investigated and reference sensor is used to represent the spectral component of the systematic error at the frequency of the applied signal.

With the assumed spectra applied to the stacked piezo, strain gages on their own offer a sensor signal with less uncertainty than can be reached by combining charge monitoring and strain gages.

Sensor fusion of strain gages and charge monitoring applied to the E-scanner results in a crossover frequency of the complementary filter of 454 Hz, in case of the enveloping spectra of the triangular signal applied to the piezo. For the expected spectrum of Z-piezo strain gages are preferred to the combined signal.

Nevertheless, the signals applied to the piezo are often lower than the expected worst-case spectra. In that case the systematic error of charge monitoring is reduced. Charge monitoring still suffers from the integrated current noise in the low frequency range. AFM images are typically acquired with a line scan rate of 0.1 Hz to 10 Hz. The main part of the noise in charge monitoring is therefore encountered below the line scan rate. After applying a line fit, these noise components are no longer relevant.

CHAPTER 7

Sensor fusion applied to AFM

In this Section the benefit of charge monitoring is demonstrated at the AFM Mulimode8 (Bruker Nano Inc., Santa Barbara, USA). For this purpose Z-piezo of the E-scanner is equipped with charge monitoring as already discussed in Chapter 4. Further a Nanoscope 5 controller (Bruker Nano Inc., Santa Barbara, USA) and a Signal Access Module III (Bruker Nano Inc., Santa Barbara, USA) is used.

The benefit on charge monitoring is shown by the example of measuring the topography of a calibration standard HS-100MG (Budget Sensors, Bulgaria, Sofia). This calibration standard shows a step height of 113 nm with 5 μm pitch. The measurement is acquired with a scanasyst-air cantilever, with a nominal spring constant of 0.4 $\frac{N}{m}$ and a measured spring constant of 0.37 $\frac{N}{m}$, determined by thermal tune [100]. The deflection sensitivity of the laser alignment is 31.23 $\frac{nm}{V}$. Figure 7.1 shows the measured topography with a scan size of 14.6 μm (maximum scan size of the used scanner). The line scan rate is 3.05 Hz with 1024 samples per line and 1024 lines. The slow scan axis is disabled at the position marked by the red line in Figure 7.1. The line profile depicted in Figure 7.2 is acquired by averaging over all the 1024 lines. No line or plane fit is applied to the measured topography. The upper profile line shows the measured topography with the elongation derived from the voltage applied to the piezo. This method is used by the Multimode AFM. To derive the height signal the voltage applied to the piezo is converted into elongation by the actuator sensitivity 7.79 $\frac{nm}{V}$ given in the calibration file. In comparison, the centered Figure depicts the elongation derived from charge monitoring. The lower Figure shows the difference of trace and retrace for charge monitoring (brown solid) and height (green dashed). The difference between trace and retrace provides a figure of merit for the quality of the measurement, as the real topography is expected to be found in between the height measured during trace and retrace. Starting from point A towards C the height signal increases, when measured from left to right (trace, blue) and decreases in case that it is measured from the right to the left (retrace, blue). Due to the closed loop the piezo

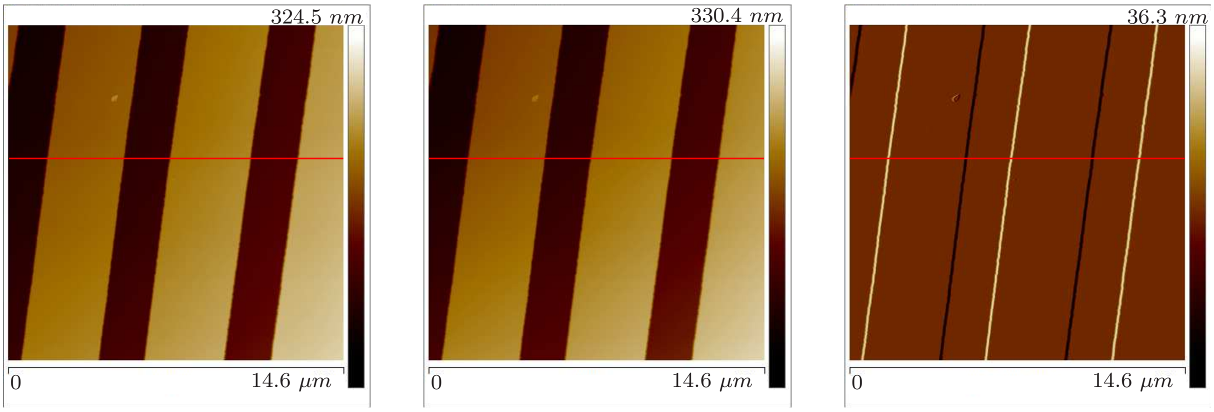

Figure 7.1: The Figure shows the acquired topography of the test grating. The left Figure shows the topography acquired from the voltage applied to the Z-piezo. Simultaneously the charge of the Z-piezo is measured and the derived topography is shown in the centered Figure. On the right Figure the deflection error is shown. No line or plane fit is applied to the measured topography.

tracks the topography. In case of increasing height (trace), due to the hysteresis more voltage is required to reach the same elongation between the point A and C, compared to the decreasing height (retrace). Therefore, a positive difference is measured in this range (green dashed). When using charge instead of voltage, the hysteresis is reduced and thereby also the difference between trace and retrace (brown solid). The peaks in the difference between trace and retrace originate from finite controller bandwidth [47], geometry of the tip [101] and lateral bending [102]. Therefore, the regions between the dashed black vertical lines are omitted when calculating the RMS value of the difference between trace and retrace. When using voltage to derive the height signal, the RMS value of the difference between trace and retrace is 2.5 *nm*. With taking advantage of charge monitoring this error could be reduced by nearly one half to 1.3 *nm*.

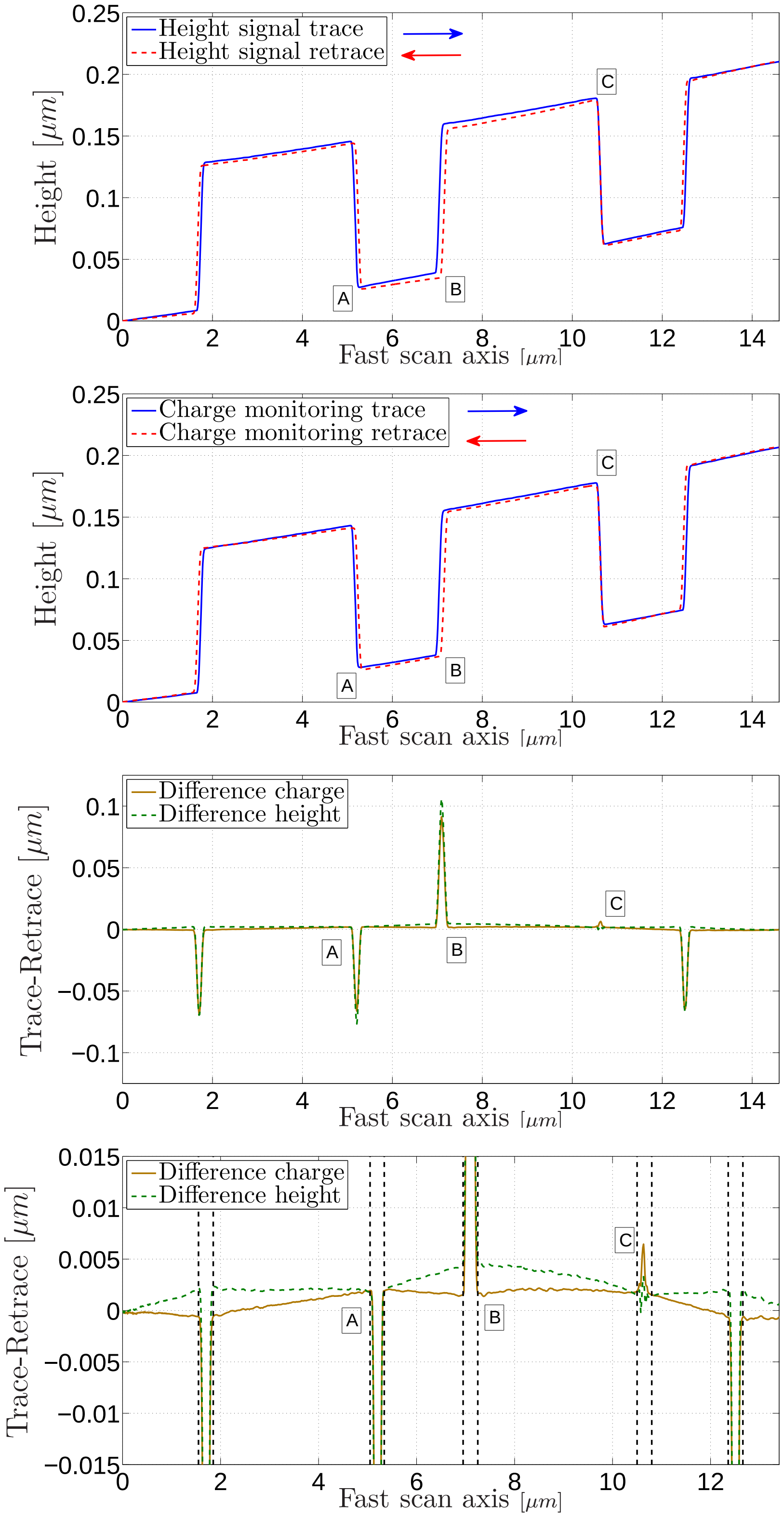

Figure 7.2: The measured topography of a calibration standard is shown. The upper figure shows the height signal acquired from the voltage applied to the piezo. The figure in the center shows the height signal, acquired by using charge monitoring. In the bottom figure the difference between trace and retrace of both measurements is shown. A significant reduction of the difference when using charge monitoring is recognized, due to the reduced hysteresis.

CHAPTER 8

Conclusion

Although piezos have significant nonlinearities they are often used without compensation. In this project charge monitoring is used to measure the elongation of a piezo. Thereby the lower frequency limit is determined as the inherent limit of the piezo's time constant as shown in Chapter 3. To overcome this limit charge monitoring is combined with strain gages.

Two different approaches for measuring the charge of the piezo are investigated and compared in respect to random errors in Chapter 4. Charge monitoring via capacitor insertion as well as charge monitoring via current integration suffer from increased noise spectral density at low frequency however arising from different origins.

Charge monitoring via current integration requires an integrator to transform the current through a shunt resistor to charge. Thereby its noise spectral density is shaped by the integrator.

The increased noise spectral density at low frequency in charge monitoring via capacitor insertion arises from current noise at the high impedance. Charge monitoring via capacitor insertion has proved to be advantageous concerning random errors (standard deviation of 2.2 nm between 1 mHz and 2 kHz) compared to charge monitoring via current integration (standard deviation of 23.4 nm between 1 mHz and 2 kHz).

To reduce the impact of low-frequency noise charge monitoring is combined with resistive strain gages in Chapter 5. In accordance to literature the high gain in the read out electronics amplifies noise arising from the used electronics and thermal noise of the strain gages. Therefore, strain gages result in low resolution (standard deviation of 2.5 nm between 1 mHz and 2 kHz) when used over high bandwidth. Nevertheless, strain gages provide a perfect counterpart to charge monitoring. After combining both sensor principles a low-cost and easy-to-integrate sensor is built. With lower noise (standard deviation of 0.56 nm between 1 mHz and 2 kHz) than each individual sensor as well as a commercial capacitive sensor.

Although, in literature often not considered - charge monitoring shows residual hysteresis which is investigated in Chapter 6. This residual hysteresis is investigated for a stacked piezo with high nonlinearities and for a tube piezo with less nonlinearities.

In order to implement a complementary filter which reduces the overall uncertainty spectral information about the systematic error is needed. Common approaches to acquire such information are restricted to linear systems. A novel approach is introduced used to estimate the extent of systematic error upfront. To allow an estimation of the spectral distribution of the systematic error, single sinusoidal signals along the spectrum of interest are applied to the piezo. The acquired systematic error between investigated and reference sensor is used to represent the spectral component of the systematic error at the frequency of the applied signal. For the system investigated in this thesis strain gages are preferred to charge monitoring whenever high accuracy is of main concern although hysteresis is reduced by 90%. When taking both systematic as well random errors into account the resulting crossover frequency is highly increased. At the example of the tube piezo from 11 mHz to 454 Hz and at the example of the stacked piezo strain gages on their own are preferred.

Nevertheless, practically encountered spectra are often below the assumed spectra which results in an decreased systematic error. When doing charge monitoring the majority of noise is encountered in the frequency range below the line scan rate of an Atomic Force Microscope. After applying a line or plane fit these noise components are no more visible in the acquired image. This motivates to apply charge monitoring without strain gages to the vertical piezo of the Atomic Force Microscope shown in Chapter 7. When using charge instead of voltage to derive the height signal the RMS value of the difference between trace and retrace is nearly reduced to one half from 2.5 nm to 1.3 nm. The reduced difference between trace and retrace indicates an improved accuracy of the measurement.

The combination of charge monitoring and strain gages offers an easy-to-integrate method to measure the elongation of a piezo. In applications where the low frequency concerns of charge monitoring are of negligible impact, charge monitoring on its own is applicable.

CHAPTER 9

Outlook

Concerning random errors the proposed approach is already competitive with common nanopositioning sensors. Nevertheless, in case of charge monitoring a significant influence of the power line is recognized. Therefore, it is recommendable to implement charge monitoring for future work on printed circuit boards. From the derived noise models the main contributors to the random error of the sensor principles are detected. Although, already taken into account in the circuit design approach of this project, with even higher quality components the resulting random error could be further reduced. Strain gages are used only in a small frequency range, nevertheless they contribute significantly to the random error of the deduced combined sensor principle. By exciting the strain gages with an AC signal, and later demodulate the bridge voltage (carrier frequency technique) the low frequency noise could be remarkable reduced.

The basic principle of charge monitoring is to build a capacitive voltage divider. Similar to bridge circuits the residual nonlinearity could be reduced by a sensing capacitor with similar nonlinearity as the residual hysteresis.

The main contributor to the systematic error in the residual nonlinearity is the changing peak-to-peak gain over range. It is assumed that this error originates from a change in piezoelectric constant d_{33} over voltage. Similar to the consideration done in Chapter 6 any change in steepness with the same extent in the dielectric domain (voltage-charge relation) and the piezoelectric domain (voltage-elongation relation) would not result in an error at charge monitoring (charge-elongation relation). Therefore, it is worth to investigate the change of d_{33} in both domains. If there is a hysteresis-free relation between these two, a compensation of the nonlinear sensitivity error of charge monitoring could be done. Thereby, a sensor with excellent resolution and good accuracy could be built.

In literature either the application of charge monitoring or hysteresis models is discussed. Nevertheless, it is a promising approach to reduce hysteresis in a first step by charge monitoring. Later, the residual hysteresis could be further reduced by a hysteresis model. Further, the hysteresis model could be used as sensor signal above the upper boundary of charge monitoring. The expected signal in this range are anyhow small and therefore it is expected that a hysteresis model would reduce hysteresis sufficiently.

Although, the residual hysteresis originates from the piezo itself, to my knowledge, there is no literature available, which kind of piezo fits best for doing charge monitoring. Analysing different geometries and materials could result to further reduction of the residual hysteresis.

Bibliography

[1] Lucy Y. Pao, Jeffrey A. Butterworth, and Daniel Y. Abramovitch. Combined feedforward/feedback control of atomic force microscopes. In *American Control Conference, 2007. ACC'07*, pages 3509–3515. IEEE, 2007.

[2] Georg Schitter. Advanced mechanical design and control methods for atomic force microscopy in real-time. In *American Control Conference, 2007. ACC'07*, pages 3503–3508. IEEE, 2007.

[3] Peter Eaton and Paul West. *Atomic Force Microscopy.* Oxford University Press, Great Clarendon Street, Oxford 0x2 6DP, 2010.

[4] V. Buscaglia, M.T. Buscaglia, M. Viviani, T. Ostapchuk, I. Gregora, J. Petzelt, L. Mitoseriu, P. Nanni, A. Testino, R. Calderone, et al. Raman and afm piezoresponse study of dense batio 3 nanocrystalline ceramics. *Journal of the European Ceramic Society*, 25(12):3059–3062, 2005.

[5] Yu G. Kuznetsov, J.G. Victoria, W.E. Robinson, and A. McPherson. Atomic force microscopy investigation of human immunodeficiency virus (hiv) and hiv-infected lymphocytes. *Journal of virology*, 77(22):11896–11909, 2003.

[6] Zhiguo Liu, Zhuang Li, Hualan Zhou, Gang Wei, Yonghai Song, and Li Wang. Imaging dna molecules on mica surface by atomic force microscopy in air and in liquid. *Microscopy research and technique*, 66(4):179–185, 2005.

[7] Claretta J. Sullivan, J.L. Morrell, David .P Allison, and Mitchel John Doktycz. Mounting of escherichia coli spheroplasts for afm imaging. *Ultramicroscopy*, 105(1):96–102, 2005.

[8] M.J. Doktycz, C.J. Sullivan, P.R. Hoyt, D.A. Pelletier, S. Wu, and D.P. Allison. Afm imaging of bacteria in liquid media immobilized on gelatin coated mica surfaces. *Ultramicroscopy*, 97(1):209–216, 2003.

[9] Th. Schimmel, Th. Koch, J. Küppers, and M. Lux-Steiner. True atomic resolution under ambient conditions obtained by atomic force microscopy in the contact mode. *Applied Physics A*, 68(4):399–402, 1999.

[10] Yoshiaki Sugimoto, Pablo Pou, Masayuki Abe, Pavel Jelinek, Rubén Pérez, Seizo Morita, and Oscar Custance. Chemical identification of individual surface atoms by atomic force microscopy. *Nature*, 446(7131):64–67, 2007.

[11] Christophe Tromas, Peter Eaton, Jean Mimault, Javier Rojo, and Soledad Penadés. Structural characterization of self-assembled monolayers of neoglycoconjugates using atomic force microscopy. *Langmuir*, 21(14):6142–6144, 2005.

[12] G. Schitter, R.W. Stark, and A. Stemmer. Fast contact-mode atomic force microscopy on biological specimen by model-based control. *Ultramicroscopy*, 100(3):253–257, 2004.

[13] Daniel Y. Abramovitch, Sean B. Andersson, Lucy Y. Pao, and Georg Schitter. A tutorial on the mechanisms, dynamics, and control of atomic force microscopes. *Proceedings of the 2007 American Control Conference*, pages 3488–3502, 2007.

[14] Ricardo Garcia and Alvaro San Paulo. Attractive and repulsive tip-sample interaction regimes in tapping-mode atomic force microscopy. *Physical Review B*, 60(7):4961, 1999.

[15] Shuiqing Hu and Arvind Raman. Chaos in atomic force microscopy. *Physical Review Letters*, 96(3):036107, 2006.

[16] Georg Schitter, Karl J. Åström, Barry E. DeMartini, Philipp J. Thurner, Kimberly L. Turner, and Paul K. Hansma. Design and modeling of a high-speed afm-scanner. *Control Systems Technology, IEEE Transactions on*, 15(5):906–915, 2007.

[17] G. Binnig and D.P.E. Smith. Single-tube three-dimensional scanner for scanning tunneling microscopy. *Review of Scientific Instruments*, 57(8):1688–1689, 1986.

[18] Georg Schitter, Wouter F. Rijkée, and Nghi Phan. Dual actuation for high-bandwidth nanopositioning. In *Decision and Control, 2008. CDC 2008. 47th IEEE Conference on*, pages 5176–5181. IEEE, 2008.

[19] Robert Munning Schmidt, Georg Schitter, and Jan van Eijk. *The Design of High Performance Mechatronics*. IOS Press BV, Nieuwe Hemweg 6b, 1013 BG Amsterdam, 2011.

[20] Brett Watson, James Friend, and Leslie Yeo. Piezoelectric ultrasonic micro/milli-scale actuators. *Sensors and Actuators A: Physical*, 152(2):219–233, 2009.

[21] Stefan Kuiper and Georg Schitter. Active damping of a piezoelectric tube scanner using self-sensing piezo actuation. *Mechatronics*, 20(6):656–665, 2010.

[22] Zhi Yu, Chen Ang, Ruyan Guo, and AS Bhalla. Piezoelectric and strain properties of ba (ti1-xzrx) o3 ceramics. *Journal of applied physics*, 92:1489–1493, 2002.

[23] Alexei Bykhovski, Boris Gelmont, and Michael Shur. The influence of the strain-induced electric field on the charge distribution in gan-aln-gan structure. *Journal of applied physics*, 74(11):6734–6739, 1993.

[24] Shan-Tao Zhang, Alain Brice Kounga, Emil Aulbach, Helmut Ehrenberg, and Jürgen Rödel. Giant strain in lead-free piezoceramics system. *Applied Physics Letters*, 91(11):112906, 2007.

[25] Ralph C. Smith, Murti Salapaka, and Luke Cherveny. Preisach model for quantifying hysteresis in an atomic force microscope. In *SPIE's 9th Annual International Symposium on Smart Structures and Materials*, pages 498–504. International Society for Optics and Photonics, 2002.

[26] Donald Croft, G. Shed, and Santosh Devasia. Creep, hysteresis, and vibration compensation for piezoactuators: atomic force microscopy application. *Journal of Dynamic Systems, Measurement, and Control*, 123(1):35–43, 2001.

[27] Kam K. Leang and Santosh Devasia. Feedback-linearized inverse feedforward for creep, hysteresis, and vibration compensation in afm piezoactuators. *Control Systems Technology, IEEE Transactions on*, 15(5):927–935, 2007.

[28] G. Song, Jinqiang Zhao, Xiaoqin Zhou, De Abreu-García, and J. Alexis. Tracking control of a piezoceramic actuator with hysteresis compensation using inverse preisach model. *Mechatronics, IEEE/ASME Transactions on*, 10(2):198–209, 2005.

[29] Andrew J. Fleming. Quantitative scanning probe microscope topographies by charge linearization of the vertical actuator. *Review of Scientific Instruments*, 81(10):103701, 2010.

[30] A.J. Fleming and K.K. Leang. Charge drives for scanning probe microscope positioning stages. *Ultramicroscopy*, 108(12):1551–1557, 2008.

[31] Han J.M.T.A. Adriaens, Willem L. De Koning, and Reinder Banning. Modeling piezoelectric actuators. *Mechatronics, IEEE/ASME Transactions on*, 5(4):331–341, 2000.

[32] R.H. Comstock. Charge control of piezoelectric actuators to reduce hysteresis effects, 1981. US Patent 4,263,527.

[33] C.V. Newcomb and I. Flinn. Improving the linearity of piezoelectric ceramic actuators. *Electronics Letters*, 18(11):442–444, 1982.

[34] Jayesh Minase, T-F Lu, B. Cazzolato, and S. Grainger. A review, supported by experimental results, of voltage, charge and capacitor insertion method for driving piezoelectric actuators. *Precision Engineering*, 34(4):692–700, 2010.

[35] G. Bertotti and I. Mayergoyz. *The Science of Hysteresis - Hysteresis in Materials*, volume 3. Elsevier, Amsterdam, 2006.

[36] Dragan Damjanovic. Contributions to the piezoelectric effect in ferroelectric single crystals and ceramics. *Journal of the American Ceramic society*, 88(10):2663–2676, 2005.

[37] Giovanni Biancuzzi, Daniel Haller, Thomas Lemke, Martin Wischke, Frank Goldschmidtboeing, and Peter Woias. A dynamic linearization concept for piezoelectric actuators. *Ultrasonics, Ferroelectrics, and Frequency Control, IEEE Transactions on*, 58(4):689–697, 2011.

[38] K. Kuhnen, H. Janocha, D. Thull, and A. Kugi. A new drive concept for high-speed positioning of piezoelectric actuators. In *Proceedings of the 10th International Conference on New Actuators*, pages 82–85, 2006.

[39] S. Salapaka, Abu Sebastian, Jason P. Cleveland, and Murti V. Salapaka. High bandwidth nano-positioner: A robust control approach. *Review of scientific instruments*, 73(9):3232–3241, 2002.

[40] Georg E. Fantner, Georg Schitter, Johannes H. Kindt, Tzvetan Ivanov, Katarina Ivanova, Rohan Patel, Niels Holten-Andersen, Jonathan Adams, Philipp J. Thurner, Ivo W. Rangelow, et al. Components for high speed atomic force microscopy. *Ultramicroscopy*, 106(8):881–887, 2006.

[41] Liang Huang, Yu Ting Ma, Zhi Hua Feng, and Fan Rang Kong. Switched capacitor charge pump reduces hysteresis of piezoelectric actuators over a large frequency range. *Review of Scientific Instruments*, 81(9):094701, 2010.

[42] Juan Du, Ying Feng, Chun-Yi Su, and Yue-Ming Hu. On the robust control of systems preceded by coleman-hodgdon hysteresis. In *Control and Automation, 2009. ICCA 2009. IEEE International Conference on*, pages 685–689. IEEE, 2009.

[43] Isaak D. Mayergoyz and G. Friedman. Generalized preisach model of hysteresis. *Magnetics, IEEE Transactions on*, 24(1):212–217, 1988.

[44] Ming-Jyi Jang, Chieh-Li Chen, and Jie-Ren Lee. Modeling and control of a piezoelectric actuator driven system with asymmetric hysteresis. *Journal of the Franklin Institute*, 346(1):17–32, 2009.

[45] Li Chuntao and Tan Yonghong. A neural networks model for hysteresis nonlinearity. *Sensors and Actuators A: Physical*, 112(1):49–54, 2004.

[46] I.A. Mahmood and S.O. Reza Moheimani. Making a commercial atomic force microscope more accurate and faster using positive position feedback control. *Review of Scientific Instruments*, 80(6):063705, 2009.

[47] Georg Schitter, Paul Menold, H.F. Knapp, F. Allgöwer, and Andreas Stemmer. High performance feedback for fast scanning atomic force microscopes. *Review of Scientific Instruments*, 72(8):3320–3327, 2001.

[48] G. Schitter, F. Allgöwer, and A. Stemmer. A new control strategy for high-speed atomic force microscopy. *Nanotechnology*, 15(1):108, 2004.

[49] G. Schitter, A. Stemmer, and F. Allgöwer. Robust two-degree-of-freedom control of an atomic force microscope. *Asian Journal of Control*, 6(2):156–163, 2004.

[50] Andrew J. Fleming. A review of nanometer resolution position sensors: Operation and performance. *Sensors and Actuators A: Physical*, pages 106–126, 2013.

[51] S. Fericean and R. Droxler. New noncontacting inductive analog proximity and inductive linear displacement sensors for industrial automation. *Sensors Journal, IEEE*, 7(11):1538–1545, Nov 2007.

[52] B. Dörband, H. Gross, and H. Müller. *Optical Systems, Metrology of Optical Components and Systems*. Gross/Optical Systems V1-V6 special prices until 6V ST published. Wiley, 2012.

[53] David K. MacKinnon, Victor Aitken, and Francois Blais. A comparison of precision and accuracy in triangulation laser range scanners. In *Electrical and Computer Engineering, 2006. CCECE'06. Canadian Conference on*, pages 832–837. IEEE, 2006.

[54] Suat Topcu, Luc Chassagne, Darine Haddad, Yasser Alayli, and Patrick Juncar. Heterodyne interferometric technique for displacement control at the nanometric scale. *Review of Scientific Instruments*, 74(11):4876–4880, 2003.

[55] G. Schitter, R.W. Stark, and A. Stemmer. Sensors for closed-loop piezo control: strain gauges versus optical sensors. *Measurement Science and Technology*, 13(4):N47, 2002.

[56] Paul P.L. Regtien. *Sensors for Mechatronics*, volume 1. Elsevier, Amsterdam, 2012.

[57] Woo-Tae Park, Joseph R. Mallon Jr, Ali J. Rastegar, Beth L. Pruitt, et al. Review: Semiconductor piezoresistance for microsystems. *Proceedings of the IEEE*, 97(3):513–552, 2009.

[58] John Nordling, Rachel L. Millen, Heather A. Bullen, Marc D. Porter, Mark Tondra, and Michael C. Granger. Giant magnetoresistance sensors. 1. internally calibrated readout of scanned magnetic arrays. *Analytical chemistry*, 80(21):7930–7939, 2008.

[59] Chiun-Peng Lee, Mei-Feng Lai, Hao-Ting Huang, Chi-Wen Lin, and Zung-Hang Wei. Wheatstone bridge giant-magnetoresistance based cell counter. *Biosensors and Bioelectronics*, 57:48–53, 2014.

[60] Jayant Sirohi and Inderjit Chopra. Fundamental understanding of piezoelectric strain sensors. *Journal of Intelligent Material Systems and Structures*, 11(4):246–257, 2000.

[61] Oliver Mack. The non-linearity of piezoelectric force transducers and their analytical modelling. In *Proceedings of the 17th World Conference–Metrology in the 3rd Millenium*, pages 22–27, 2003.

[62] King A. Yi and Robert J. Veillette. A charge controller for linear operation of a piezoelectric stack actuator. *IEEE Transactions on Control System Technology*, 13(4):517–526, 2005.

[63] Andrew J. Fleming and S.O. Reza Moheimani. Hybrid dc accurate charge amplifier for linear piezoelectric positioning. In *Proc. 3rd IFAC Symp. Mechatron. Syst*, pages 283–288, 2004.

[64] Ioan Alexandru Ivan, Micky Rakotondrabe, Philippe Lutz, and Nicolas Chaillet. Quasistatic displacement self-sensing method for cantilevered piezoelectric actuators. *Review of Scientific Instruments*, (80), 2009.

[65] Mohsen Bazghaleh, Steven Grainger, Ben Cazzolato, Tien-Fu Lu, and Reza Oskouei. Implementation and analysis of an innovative digital charge amplifier for hysteresis reduction in piezoelectric stack actuators. *Review of Scientific Instruments*, 85(4):91–98, 2014.

[66] Mohsen Bazghaleh, Steven Grainger, Morteza Mohammadzaheri, Ben Cazzolato, and Tien-Fu Lu. A novel digital charge-based displacement estimator for sensorless control of a grounded-load piezoelectric tube actuator. *Sensors and Actuators A: Physical*, 198(80):91–98, 2013.

[67] S. Kuiper and G. Schitter. Self-sensing actuation and damping of a piezoelectric tube scanner for atomic force microscopy. In *Control Conference (ECC), 2009 European*, pages 3887–3892, Aug 2009.

[68] S.O. RezaMoheimani and Andrew J. Fleming. *Piezoelectric Transducers for Vibration Control and Damping.* Springer-Verlag London, London, 2006.

[69] Stefan Kuiper. *Mechatronics and Control Solutions for Increasing the Imaging Speed in Atomic Force Microscopy.* PhD thesis, Delft Center for Systems and Control, Delft University of Technology, 2011.

[70] Standards Committee of the IEEE Ultrasonics, Ferroelectrics, and Frequency Control Society. Ieee standard on piezoelectricity. 1988.

[71] Pat Barney, Jim Redmond, and David Smith. Characteristics of self-sensing actuation for active control. Technical report, Sandia National Labs., Albuquerque, NM (United States), 1996.

[72] Jeffrey J. Dosch, Daniel J. Inman, and Ephrahim Garcia. A self-sensing piezoelectric actuator for collocated control. *Journal of Intelligent Material Systems and Structures*, 3(1):166–185, 1992.

[73] Robert Grover Brown and Patrick Y. C. Hwang. *Introduction to Random Signals and Applied Kalman Filtering.* John Wiley and Sons, New York, 1997.

[74] JR. Walter T. Higgens. A comparison of complementary and kalman filtering. *IEEE Transactions on Aerospace and Electronic Systems*, AES-11(3):321–325, 1975.

[75] Hyung-Jik Lee and Seul Jung. Gyro sensor drift compensation by kalman filter to control a mobile inverted pendulum robot system. In *Industrial Technology, 2009. ICIT 2009. IEEE International Conference on*, pages 1–6. IEEE, 2009.

[76] Hyungjik Lee and Seul Jung. Balancing and navigation control of a mobile inverted pendulum robot using sensor fusion of low cost sensors. *Mechatronics*, 22(1):95–105, 2012.

[77] Andrew J. Fleming, Adrian G. Wills, and S. O. Reza Moheimani. Sensor fusion for improved control of piezoelectric tube scanners. *IEEE Transaction on Control Systems Technology*, 16(6):1265–1276, November 2008.

[78] Andrew J. Fleming and Kam K. Leang. Integrated strain and force feedback for high-performance control of piezoelectric actuators. *Sensors and Actuators A: Physical*, 161(1):256–265, 2010.

[79] Stefan Kuiper, A.J. Fleming, and Georg Schitter. Dual actuation for high speed atomic force microscopy. In *Proc. IFAC Mechatronics Conf*, pages 441–446. Citeseer, 2010.

[80] Dominik Kohl, Thomas Riel, Rudolf Saathof, Juergen Steininger, and Georg Schitter. Auto-tuning pi controller for surface tracking in atomic force microscopy - a practical approach. *The 2016 American Control Conference, Boston, USA, in press (2016)*, 2016.

[81] I.P. Lipscomb, P.M. Weaver, J. Swingler, and J.W. McBride. The effect of relative humidity, temperature and electrical field on leakage currents in piezo-ceramic actuators under dc bias. *Sensors and Actuators A: Physical*, 151(2):179–186, 2009.

[82] Cyril M. Harris and Allan G. Piersol. *Shock and Vibration Handbook*. McGraw-Hill, New York, Fifth Edition edition, 2002.

[83] Rudolf Müller. *Rauschen*. Springer Verlag, Heidelberg, 1990.

[84] Gabriel Vasilescu. *Electronic Noise and Interfering Signals*. Springer Verlag, Heidelberg, 2004.

[85] J.A. Goetz and Frank Jay. *IEEE Standard Dictionary of Electrical and Electronics Terms*. Wiley Interscience, New York, 1984.

[86] Paul C. Dow. An analysis of certain errors in electronic differential analyzers ii-capacitor dielectric absorption. *IRE Transactions on Electronic Computers*, pages 17–22, 1958.

[87] Art Kay. *Operational Amplifier Noise: Techniques and Tips for Analyzing and Reducing Noise*. Newnes, Newton, MA, USA, 1st edition, 2012.

[88] F.J. Lidgey and K. Hayatleh. Current-feedback operational amplifiers and applications. *Electronics & communication engineering journal*, 9(4):176–182, 1997.

[89] Manel Gasulla, Xiujun Li, and Gerard Meijer. The noise performance of a high-speed capacitive-sensor interface based on a relaxation oscillator and a fast counter. *Instrumentation and Measurement, IEEE Transactions on*, 54(5):1934–1940, 2005.

[90] Emily J. McDowell, Xiquan Cui, Zahid Yaqoob, and Changhuei Yang. A generalized noise variance analysis model and its application to the characterization of 1/f noise. *Optics express*, 15(7):3833–3848, 2007.

[91] WY Ho, Charles Surya, KY Tong, Wook Kim, Andrei E Botcharev, and Hadis Morkoç. Characterization of flicker noise in gan-based modfet's at low drain bias. *Electron Devices, IEEE Transactions on*, 46(6):1099–1104, 1999.

[92] Y. Fu, H. Wong, and Juin J. Liou. Characterization and modeling of flicker noise in junction field-effect transistor with source and drain trench isolation. *Microelectronics Reliability*, 47(1):46–50, 2007.

[93] Zenji Yatabe, Toru Muramatsu, Joel T. Asubar, and Seiya Kasai. Calculating relaxation time distribution function from power spectrum based on inverse integral transformation method. *Physics Letters A*, 379(7):738–742, 2015.

[94] Daniel Roetenberg, Henk J. Luinge, Chris Baten, and Peter H. Veltink. Compensation of magnetic disturbances improves inertial and magnetic sensing of human body segment orientation. *Neural Systems and Rehabilitation Engineering, IEEE Transactions on*, 13(3):395–405, 2005.

[95] Manel Martinez-Ramon, J Arenas-Garcia, A Navia-Vázquez, et al. An adaptive combination of adaptive filters for plant identification. In *Digital Signal Processing, 2002. DSP 2002. 2002 14th International Conference on*, volume 2, pages 1195–1198. IEEE, 2002.

[96] Jian-shu Liu, Ren-hou Li, and Hong Chang. Multi-sensor data fusion based on correlation function and least square. *Control and Decision*, 21(6):714, 2006.

[97] Seung-Jean Kim, Kwangmoo Koh, Michael Lustig, Stephen Boyd, and Dimitry Gorinevsky. An interior-point method for large-scale l 1-regularized least squares. *Selected Topics in Signal Processing, IEEE Journal of*, 1(4):606–617, 2007.

[98] Stuart Geman, Elie Bienenstock, and René Doursat. Neural networks and the bias/variance dilemma. *Neural computation*, 4(1):1–58, 1992.

[99] Roger Barlow. *Statistics: A Guide to the Use of Statistical Methods in the Physical Sciences.* John Wiley and Sons Ltd., Chichester, 1999.

[100] Benjamin Ohler. Cantilever spring constant calibration using laser doppler vibrometry. *Review of Scientific Instruments*, 78(6):063701, 2007.

[101] Peter Markiewicz and M. Cynthia Goh. Simulation of atomic force microscope tip–sample/sample–tip reconstruction. *Journal of Vacuum Science & Technology B*, 13(3):1115–1118, 1995.

[102] Mark C Strus, Arvind Raman, Chang-Soo Han, and C.V. Nguyen. Imaging artefacts in atomic force microscopy with carbon nanotube tips. *Nanotechnology*, 16(11):2482, 2005.